

**COSMIC NEUTRINO EVENTS
IN HIRES I DETECTOR**

by

Kiyoung Kim

A dissertation submitted to the faculty of
The University of Utah
in partial fulfillment of the requirements for the degree of

Doctor of Philosophy

Department of Physics

The University of Utah

August 2002

Copyright © Kiyoung Kim 2002

All Rights Reserved

THE UNIVERSITY OF UTAH GRADUATE SCHOOL

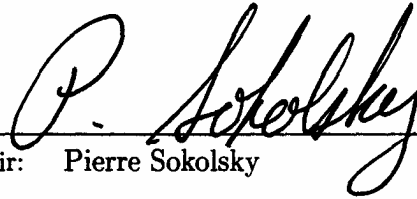
SUPERVISORY COMMITTEE APPROVAL

of a dissertation submitted by

Kiyoung Kim

This dissertation has been read by each member of the following supervisory committee and by majority vote has been found to be satisfactory.

June 20, 2002



Chair: Pierre Sokolsky

Eugene Loh

June 20, 2002



Craig Taylor

Yong-Shi Wu

June 20, 2002



Allan A. Ekdale


THE UNIVERSITY OF UTAH GRADUATE SCHOOL

FINAL READING APPROVAL

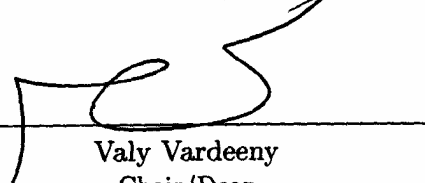
To the Graduate Council of the University of Utah:

I have read the dissertation of Kiyoung Kim in its final form and have found that (1) its format, citations, and bibliographic style are consistent and acceptable; (2) its illustrative materials including figures, tables, and charts are in place; and (3) the final manuscript is satisfactory to the Supervisory Committee and is ready for submission to The Graduate School.

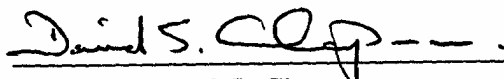
June 20 2002
Date


Pierre Sokolsky
Chair, Supervisory Committee

Approved for the Major Department


Valy Vardeeny
Chair/Dean

Approved for the Graduate Council


David S. Chapman
Dean of The Graduate School

ABSTRACT

High energy cosmic neutrino events ($\geq 10^{15}$ eV) – deeply penetrating events in the atmosphere and upward-going events from the Earth surface – are searched for with the HiRes I detector located at Dugway Proving Grounds in Utah. The detector acceptance for the neutrino events is calculated using a Monte Carlo simulation for neutrino events in the atmosphere or below the surface of the Earth and a parton model for the neutrino cross section. The events rates in the HiRes I detector for various cosmic neutrino spectrum models, such as AGN-M95, AGN-SS91, AGN-P96, and GRB-WB, are estimated and compared with HiRes I data.

To My Parents
Wife, Yunsil, and Daughter, Jacqueline

CONTENTS

ABSTRACT	iv
LIST OF FIGURES	viii
LIST OF TABLES	xi
ACKNOWLEDGEMENTS	xii
CHAPTERS	
1. INTRODUCTION	1
2. COSMIC RAYS	4
2.1 Astrophysical Information	4
2.1.1 Spectrum	4
2.1.2 Chemical Composition, Isotropy, and Homogeneity	5
2.2 Extensive Air Showers (EAS) for EHE	
Cosmic Rays	6
2.2.1 Electromagnetic Shower Development	7
2.2.2 Hadronic Shower Development	10
3. LIGHT PRODUCTION AND PROPAGATION	13
3.1 Cherenkov Light	13
3.2 Atmospheric Fluorescence Light	14
3.3 Propagation in the Atmosphere	14
3.3.1 Rayleigh Scattering	14
3.3.2 Aerosol Scattering (Mie Scattering)	15
4. HIRES I DETECTOR	16
4.1 Detector Geometry and Mirror Optics	16
4.1.1 Spot Size and Shape	17
4.2 Photomultiplier Tube(PMT) Response	19
4.2.1 Background Noise and PMT Threshold	19
4.3 Events in the Detector	20
4.4 Event Selection and Data Flow	23
5. COSMIC NEUTRINOS	25
5.1 The Spectrum Models	25
5.2 Neutrino - Nucleon Interactions	27
5.2.1 Neutrino Cross Section	27
5.2.2 The 6.3 PeV $\bar{\nu}_e$ Resonance and Electron Interaction	30
5.2.3 The Landau-Pomeranchuk-Migdal (LPM) Effect	33

6. DETECTOR MONTE CARLO	40
6.1 Event Geometry	41
6.2 Neutrino Events	43
6.3 Extensive Air Shower (EAS)	44
6.4 Detector Acceptance	46
6.4.1 Detector Aperture(\mathcal{A})	46
6.4.2 Neutrino Event Rate	50
7. NEUTRINO EVENT SEARCH	54
7.1 Search Mechanism	54
7.1.1 Criterion for Neutrino Events	55
7.2 Geometrical Reconstruction	58
7.2.1 Plane Fit	59
7.2.2 Timing Fit	62
7.3 Other Possible Deeply Penetrating Events	64
7.4 Neutrino Events Search	64
7.4.1 Xenon Flashers and YAG Laser Events Filtering	64
7.4.2 Neutrino Events Search with MC Data	66
7.4.3 HiRes I Data and Data Processing	67
8. CONCLUSION AND DISCUSSION	72
8.1 Conclusion	72
8.2 Discussion	73
8.3 Summary of MC	74
REFERENCES	76

I
I
I

LIST OF FIGURES

2.1 The differential cosmic ray flux[14]	5
2.2 EM shower developments(10^{15} to 10^{19} eV)	10
2.3 EM and Hadronic showers and their mixture	12
4.1 Cluster plane (meter scale); each tube size has ~ 4 cm diameter	17
4.2 Spot size and the shadow effect: 0, 4, and 7 degrees off the mirror axis(F1) and the corresponding X-axis projections in (F3); 2, 5, and 8 degrees off the mirror axis(F2) and their Y-axis projections (F4). the spot for 8 degrees off the mirror axis is shown at left below in (F2).	18
4.3 Mirror threshold distributions; the vertical lines indicate average thresholds(mV) for the period of (09/04/1999 - 11/07/2000)	21
4.4 Mirror threshold(mV) variations on julian dates from 09/04/1999 to 11/07/2000	22
5.1 Differential flux of muon neutrinos($\nu_\mu + \bar{\nu}_\mu$)	26
5.2 $\bar{\nu}_e e \rightarrow \bar{\nu}_e e$, $\bar{\nu}_e e \rightarrow \bar{\nu}_e \tau$, $\bar{\nu}_e e \rightarrow hadrons$, $\bar{\nu}_e N$ interaction	31
5.3 Secondary lepton energy and the angular distributions	32
5.4 Earth mass density vs. radius	33
5.5 Differential bremsstrahlung intensities and differential pair-production probabilities per radiation length	34
5.6 LPM effect on 10^{+15} , 10^{+16} , and 10^{+17} eV photon initiated cascades in the earth : small solid squares represent the GH profile initiated by a 10^3 TeV photon; solid circles, LPM effect for 10^3 TeV photon; solid triangles, LPM effect for 10^4 TeV photon; empty squares, LPM effect for 10^5 TeV photon.	36
5.7 $1.0E+7$ TeV electron initiated cascades in the earth, and the equivalent GH profile in the air for every 200 radiation length(X_o)	37
5.8 Shower profiles in the air initiated by preshowers by a $1.0E+7$ TeV electron inside the earth ; for instance, the 201 profile represents a $1.0E+7$ TeV electron initiating an EM showers at 201 X_o below the earth surface, and finally emerging to the air	38
5.9 EM showers with LPM effect initiated by $1.0E+9$ TeV electron at altitudes, 25, 20, 15, 10, 5, 0 km (from left)	39
6.1 Cosmic-ray impact points projection on the earth's surface	41
6.2 Neutrino event geometries and the cases	42

6.3	Detector trigger rates versus R_p in MC for neutrino events: The dashed lines indicate that the $1/R_p^2$ functional fit is not successful using all data points for neutrino energy between 10^{16} eV and 10^{18} eV. The solid lines indicates that the fitting is successful if some small R_p data points are removed.	43
6.4	Neutrino interaction probability versus zenith angle within the depth of $1.0 \times 10^{+5}$ g/cm ² (980 m) from the impact point on the earth surface in the neutrino trajectory. Empty circles are for an incident neutrino energy of $1.0 \times 10^{+15}$ eV; solid squares, $1.0 \times 10^{+16}$ eV; upward-going triangles, $1.0 \times 10^{+17}$ eV; downward-going triangles, $1.0 \times 10^{+18}$ eV; solid circles, $1.0 \times 10^{+19}$ eV.	45
6.5	HiRes I detector acceptance for upward-going and downward-going neutrino events	47
6.6	HiRes I detector acceptance for the atmospheric neutrino events and for the earth originated neutrino events.	48
6.7	Aperture for pseudo-horizontal($\theta > 70^\circ$.) and upward-going events.	49
6.8	Aperture dependence on zenith angle for E_ν : $10^{15} - 10^{16}$ (eV), $10^{17} - 10^{18}$ (eV), and $10^{19} - 10^{20}$ (eV) ; the outermost thick boundary indicates the total sum for E_ν of $10^{15} - 10^{20}$ (eV).	50
6.9	Neutrino events expectation in HiRes I detector for 1 year(detector on time)	51
6.10	Pseudo-horizontal or upward-going events expectation ($\theta > 70^\circ$)	52
7.1	HiRes I detector acceptance : solid circles indicate total detector acceptance; downward-going triangles, for horizontal events; empty squares, for atmospheric events; empty circles, for earth-originated events.	55
7.2	HiRes I detector Aperture for Hadronic events with a 6-degree track cut : Solid circles represent the aperture for all zenith angles; empty boxes, for zenith angles, $\theta > 70^\circ$; empty circles, for zenith angles, $\theta > 80^\circ$; downward triangles, for zenith angles, $\theta > 82^\circ$; upward triangles, for zenith angles, $\theta > 84^\circ$	56
7.3	Plane normal angle distributions for the HiRes I detector aperture for the primary cosmic rays, neutrino and proton, with a 6-degree track length cut: The out most thick lines indicate total sums; $1.0 \times 10^{15} - 1.0 \times 10^{20}$ eV for Neutrino and $1.0 \times 10^{16} - 1.0 \times 10^{19}$ eV for Proton	57
7.4	Differential cosmic ray spectrum(1.0×10^{16} eV $< E < 1.0 \times 10^{19}$ eV) : Ref. Fig. 2.1	58
7.5	Hadronic event rates in the HiRes I detector depending on the SD plane normal angle cut: solid circles represent all angles; solid boxes, for a 20-degree cut; upward triangles, for a 15-degree cut; downward triangles, for a 12-degree cut; and empty circle, for a 10-degree cut. The uncertainties are from the statistics in the MC and the spectrum.	59
7.6	Event rates vs. neutrino energy with 12-degree plane normal angle cut: solid circles indicate AGN-M95; solid boxes, AGN-SS91; upward-going triangles, AGN-P96; downward-going triangles, GRB-WB.	61
7.7	Pseudo-horizontal neutrino events for $5.5 \times 10^{17} < E < 1.0 \times 10^{18}$ eV: resolution of SD plane fit; co-relations to to χ^2 and the number of PMTs . .	62

7.8 Shower axis and the direction of propagation in the SD plane; $L_i(i = 1, 2, \dots)$ is the distance from the Detector to the shower axis for each bin(bin size : 1 degree)	63
7.9 Detector acceptances with plane normal angle cuts	65
7.10 The event on the cluster box plane	69
7.11 Shower size vs. slant depth	70
7.12 EM longitudinal Gaisser-Hillas profile with energy 1.6×10^{10} GeV; slant depth is shifted $+8530 \text{ g/cm}^2$	71
8.1 $\nu_\mu + \bar{\nu}_\mu$ neutrino flux limit for $\gamma = 1, 2, 3$	73

LIST OF TABLES

2.1 π , K meson decay modes and fractions	8
4.1 Average mirror thresholds(mV) in HiRes I detector(09/04/1999 - 11/07/2000)	23
5.1 Neutrino-electron interactions at 6.3 PeV	30
6.1 Number of events expected per year (detector on time).	53
6.2 Number of events expected per year ($\theta > 70^\circ$).	53
7.1 Hadronic events rates for 1 year(detector on time) in HiRes I detector(6-degree track length cut)	60
7.2 Neutrino events with the 10-degree SD plane normal angle cut for 1 year (detector on time)	60
7.3 Neutrino events with the 12-degree SD plane normal angle cut for 1 year (detector on time)	60
7.4 Neutrino events with the 15-degree SD plane normal angle cut for 1 year(detector on time)	61
7.5 Neutrino events search efficiency with the 12-degree cut.	67
7.6 Neutrino events expectation in the HiRes I detector for 1 year(detector on time) with the 12-degree SD plane normal angle cut and the events search efficiency.	68

ACKNOWLEDGEMENTS

I deeply appreciate my parents for their endless encouragement and unlimited patience in waiting for my achievement while I have studied physics for a long time. I also thank to my family and friends for their understanding and expectation on my work in physics.

Without my wife and daughter, especially my wife's cordially concern and assistance, I would not have completed this work. I dedicate this small achievement to my parents, wife, and daughter.

While I have worked at the HIRES Cosmic Ray Group in University of Utah, I have received a lot of assistance from group members. I appreciate all of them. Especially, I wish to thank my adviser Prof. Pierre Sokolsky for his kindness, generosity, and lots of advice in physics for the last 5 years. Finally I appreciate Prof. Eugene Loh, Prof. Craig Taylor, Prof. Yong-Shi Wu, and Prof. Tony Ekdale for their advice on my thesis.

CHAPTER 1

INTRODUCTION

In the night sky we can see innumerable bright objects – stars, planets, the Milky Way, nebulae – with the naked eye. Without using any equipment we can see only the visible range of light coming from the stars; however, they radiate IR (infrared) and UV (ultraviolet) light too, and some of them are sources of highly energetic elementary particles and/or nuclei. Cosmic rays are particles coming from outer space, such as protons, α particles, γ -rays, heavier nuclei, etc. Some of them have an extremely high energy (EHE) ($\sim 1.0 \times 10^{18}$ eV or above[1]) or ultra high energy (UHE) ($\geq 1.0 \times 10^{19}$ eV). Measurements of UHE cosmic rays beyond the Greisen-Zatsepin-Kuz'min (GZK) cutoff energy ($\sim 5.0 \times 10^{19}$ eV) have been reported by the Fly's Eye group in Utah and by others.[2] The discovery of cosmic rays beyond the GZK cutoff energy contradicts the theory of universal distribution of cosmic ray sources because of the GZK cutoff mechanism[3] in which UHE cosmic rays beyond the cutoff energy can interact effectively with the 2.7K microwave background radiation (MBR) via

$$\gamma_{2.7} + p \rightarrow \Delta^{*+} \rightarrow p + \pi^0 \text{ or } n + \pi^+ \quad (1.1)$$

implies that they cannot survive more than ~ 50 Mpc in intergalactic space.

The pertinent questions include the following: what are these UHE particles, where are they coming from, how can they have such extremely high energies, and how do they propagate and survive through interstellar and intergalactic space? These have been the prime concerns in cosmic ray physics since the emergence of *cosmic ray astrophysics* in the early 1950s. Unfortunately, the answers for those questions are still not clear. Moreover, if the GZK mechanism exists, we have not, up to now, found a reasonable and acceptable explanation for the events which have been reported beyond the cutoff energy.[4] Is there any unknown mechanism in cosmic ray creation and propagation which bypasses the GZK cutoff?

To answer those fundamental questions and explain the observation of UHE events beyond the GZK cutoff energy, many cosmic-ray spectrum models and scenarios have been proposed. One of the models[5] which has been suggested to avoid the GZK cutoff mechanism has to do with interactions of possible UHE neutrinos with relic neutrinos within 50 Mpc from the earth. UHE cosmic rays are produced from these interactions and the puzzle of post-GZK- cutoff events can be solved naturally. However, the model is speculative and still has no experimental basis. What about searching for the existence of the cosmic ray neutrino flux directly?

Due to the extremely small cross section of a neutrino in comparison with other elementary particles, it is difficult for us to get meaningful statistics in a short time period compared to cosmic rays, such as protons, iron, γ -rays, etc. However, the same property leads to several distinctive characteristics of neutrino events. For instance, since every cosmic-ray spectrum model simultaneously implies a neutrino spectrum as a by-product, it is relatively straightforward to estimate the neutrino spectrum from the origin of acceleration (the small cross section makes it almost interaction free from the source to the detection point). Then, the observed cosmic-ray neutrino spectrum can be compared with the estimation. Furthermore, if there is a local source (for instance, SN1987A, the quasar 3C279[6]), it is easy to locate the possible neutrino source since neutrinos are not affected by the interstellar medium and magnetic fields ($B \sim 10^{-8} - 10^{-10}$ T).

Although relatively low-energy neutrino events (\sim MeV, mainly from the Sun, up to \sim TeV, originating from the interactions of high energy cosmic rays with the earth's atmospheric nucleus) have been detected in Super Kamiokande, SNO, AMANDA, Baikal, etc.[7], EHE and/or UHE cosmic neutrino events have not been detected yet. In 1984, 1985, and 1992 neutrino (and deeply penetrating particle in general) events searches in the Fly's Eye detector[8, 9] had been performed. In 1991 the neutrino event expectation for HiRes (the High Resolution Fly's Eye) detector (which uses atmospheric nitrogen fluorescence to detect EAS[Extensive Air Showers] initiated by a high-energy cosmic ray) was estimated for a high-energy ν flux from Active Galactic Nuclei(AGN)[10]. Unfortunately, no neutrino events have been found in the Fly's Eye and HiRes Prototype detectors in Utah.

Since then, many cosmic neutrino¹ spectrum models have been updated and/or have emerged [11], and the parton model for the neutrino cross section has been updated. [13]

¹At 1.0×10^{15} eV and above all sources(models) dominate the background of atmospheric neutrinos.

The main issue of this work is to search for neutrino and/or deeply penetrating events with the HiRes I Detector, which has run since May 1997 with much improved detector resolution compared to the Fly's Eye Detector. Hopefully, if we can detect enough events to get statistical significance, we can compare the cosmic neutrino spectrum models with the event rate in the HiRes I Detector and also independently from the spectrum models we can confirm whether the cosmic neutrino cross section, which has been estimated from the parton model, represents reality by comparing the event ratio between upward going to downward going events. If we do not find any neutrino events or deeply penetrating event candidates, we can still estimate the minimum cosmic neutrino flux required for the HiRes I Detector to detect at least one neutrino event.

In Chapter 2, the cosmic ray spectrum and the chemical composition for hadronic interactive cosmic rays, such as protons, irons, γ -rays are discussed. Scintillation light production and propagation will be discussed briefly in Chapter 3, and the HiRes I Detector operation, electronics, and event selection and data flow are described in Chapter 4. The cosmic neutrino cross section, the spectrum models, the characteristic differences of neutrino events from hadronic events in event geometry and shower development all are discussed in Chapter 5. In the next chapter, the detector Monte Carlo(MC) for the cosmic neutrino events is discussed in detail. In Chapter 7, the event search mechanism for cosmic neutrinos or other deeply penetrating cosmic rays is explained, and the HiRes I data analysis and the result are shown. Conclusion and discussion are in Chapter 8.

CHAPTER 2

COSMIC RAYS

Every second, cosmic ray particles hit the earth's atmosphere at the rate of about 1000 per square meter. In cosmic ray physics we can consider the universe itself to be a part of the experimental setup for the study of cosmic ray sources even though we cannot control the time and the place of an event. We can get unique astrophysical information including origin, spectrum, composition, anisotropy, and we can also apply and/or test results from high-energy particle physics. From time to time we can expect extremely high-energy(EHE) cosmic rays – well beyond the available energies from contemporary accelerators.

2.1 Astrophysical Information

2.1.1 Spectrum

The flux of cosmic rays has been known to follow a power law of energy as

$$\frac{dN(E)}{dE} \propto E^{-\gamma},$$

where γ is the spectral index, which is approximately 2.5 to 3.1 depending on the energy range as shown in Figure 2.1. There are two sudden changes of the slope indicating that there should be, at least, a couple of distinctive mechanisms in cosmic-ray creation and propagation depending on the cosmic-ray energy and the composition.[15] The first break is at around a PeV – called the *knee* – and the second, at around 3×10^{18} eV – called the *ankle*. For the all particle spectrum, the spectrum index below 10^{15} eV is about 2.5 - 2.7 and above the knee is about 3.1. At around the ankle the spectrum index changes from 3.01 at 0.1 EeV to 3.27 at 0.3 EeV, and changes again to 2.71 above 3 EeV. The sudden changes of the slope is well indicated in Figure 7.4.

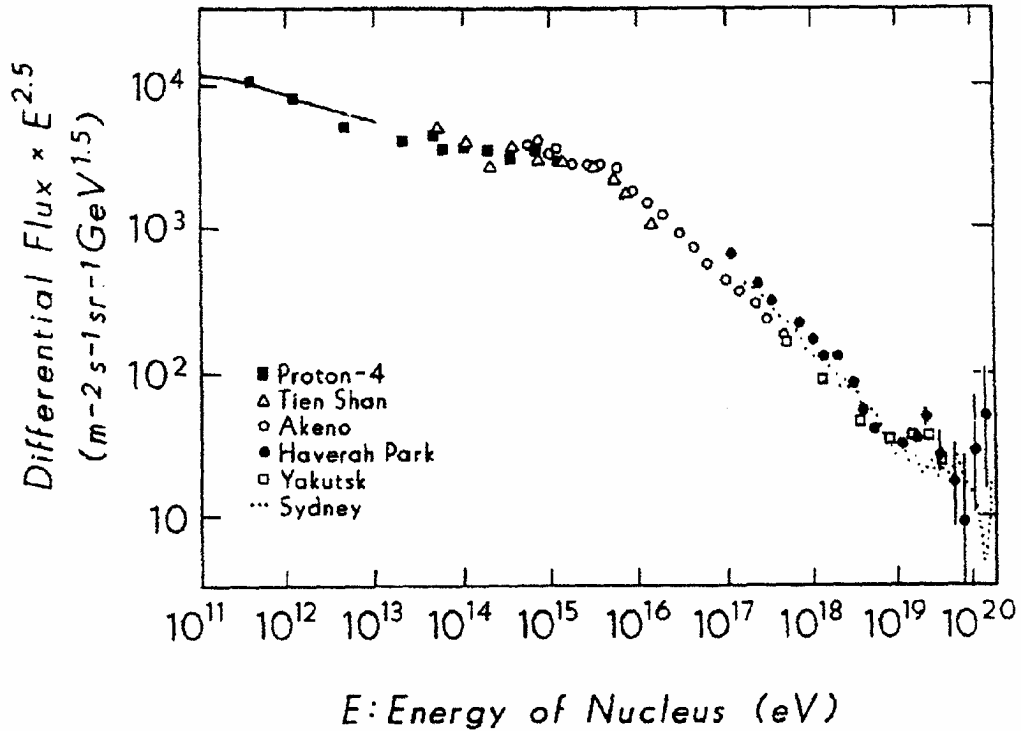


Figure 2.1. The differential cosmic ray flux[14]

2.1.2 Chemical Composition, Isotropy, and Homogeneity

From the TeV to the PeV energy region the chemical composition of cosmic rays is known to be $\sim 50\%$ proton, $\sim 25\%$ α -particles, $\sim 13\%$ CNO, $\sim 13\%$ Fe, $\leq 10^{-2}\%$ electron, and $\leq 10^{-3}\%$ γ -rays.[16] For the EHE region, in which experiments are indirect, the chemical composition study can be done, for instance, by investigating X_o (the first interaction depth in the atmosphere), X_{max} (depth at shower maximum), and the width of the EAS (Extensive Air Showers) profile. In a simple picture, if a nucleus with A nucleons and energy E_o breaks into A nucleons each with energy E_o/A , and if these A nucleons contribute to the EAS development independently, the shower develops faster than one resulting from one nucleon carrying all the energy E_o . Of course, the detailed estimation depends on the hadronic interaction model[17] for the inelastic cross section σ^{inel} and the inelasticity $K = \frac{E_o - E'}{E_o - M_n}$, where E_o is the initial energy, E' is the energy after collision, and M_n is the target mass.

Hence, lighter nuclei tend to have longer interaction lengths than do heavier nuclei, and the EAS profiles of lighter nuclei develop deeper and fluctuate more than do heavier

nuclei.

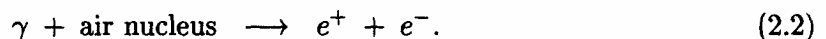
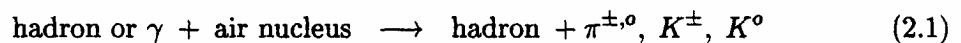
Although some point sources have been identified with Cygnus X-3, Hercules X-1, the Crab pulsar etc. (transient sources), isotropy and homogeneity in cosmic rays have been a general assumption in cosmology.

2.2 Extensive Air Showers (EAS) for EHE Cosmic Rays

The cosmic ray flux below the knee ($< 10^{15}$ eV) is high enough for direct measurements using calorimeters, emulsion stacks, etc; moreover, phenomenological theories for the cosmic ray interactions inside experimental devices – cross section (σ_{inel}) and secondary particle multiplicity – can be tested directly using accelerators. On the other hand, the flux of EHE cosmic rays as shown in Figure 2.1 is so low that experiments must be indirect, for instance, by detecting atmospheric EAS produced by the primary cosmic ray particle; and the phenomenological particle interaction theories for this energy region cannot be tested directly because of the high energy.

When an EHE cosmic ray particle enters the earth atmosphere, it interacts with an atmospheric nucleus (nitrogen or oxygen) near the top of the atmosphere. In the interaction the primary cosmic ray particle loses some part of the initial energy to the creation of new particles (secondaries). Now, the primary, if it has not been broken up, and the secondaries interact with air nuclei as did the primary before, and other secondary particles are produced and added to the EAS profile. The parents, if they have not been broken up yet, and the secondaries, keep interacting with air nuclei and feeding the EAS. The majority of the EAS particles become electrons (e^-) and positrons (e^+), and the average energy of EAS particles keeps getting lower and lower as the shower develops while the size of EAS gets bigger and bigger. This cascade process keeps going on until the average energy of EAS particles reaches the critical energy E_c for *bremsstrahlung* interaction. At that point the EAS profile reaches a maximum at a depth called X_{max} . At depths beyond X_{max} the energy loss of the shower particles is mainly from ionization loss (collisional process), which dominates over *bremsstrahlung* and *pair production*. The size of the EAS gets smaller and smaller, and finally the shower disappears.

In the first interaction, the majority of secondaries are pions (π^+, π^-, π^0) and kaons (K^\pm, K^0) for hadronic showers and e^\pm for electromagnetic showers



When an EHE photon interacts with an air nucleus, the relative probability of photo-production to pair production (e^+e^-), $R = \sigma_{\gamma \rightarrow \text{hadrons}} / \sigma_{\gamma \rightarrow e^+e^-} \approx 2.8 \times 10^{-3}$ [18], and the possible production of $\mu^+\mu^-$ in pair production is highly suppressed by a factor of order $(m_e/m_\mu)^2 \sim 2 \times 10^{-5}$.

Because of the short life times(τ) of the mesons, π^\pm ($\tau \sim 2.6 \times 10^{-8}$ sec), π^0 ($\tau \sim 8.4 \times 10^{-17}$ sec), K^\pm ($\tau \sim 1.2 \times 10^{-8}$ sec), K_S^0 ($\tau \sim 0.9 \times 10^{-10}$ sec), and K_L^0 ($\tau \sim 5.2 \times 10^{-8}$ sec) the secondary mesons such as pions and kaons in the hadronic interaction often decay before they interact with air nuclei. The decay modes are

$$\begin{aligned}\pi^\pm &\longrightarrow \mu^\pm + \nu_\mu(\bar{\nu}_\mu) \\ \pi^0 &\longrightarrow 2\gamma.\end{aligned}\tag{2.3}$$

Table 2.1 shows the π and K meson decay modes and the branching ratios.[19] The muons(μ^\pm) in Equation (2.3) also decay as

$$\mu^\pm \longrightarrow e^\pm + \nu_e(\bar{\nu}_e) + \bar{\nu}_\mu(\nu_\mu),\tag{2.4}$$

but their mean life time ($\tau \sim 2.2 \times 10^{-6}$ sec) is much longer than the life time of pion or kaon. Because the *bremsstrahlung* interaction is inversely proportional to the square of the rest mass of the radiating particle, the radiation length for muons is $\sim (m_\mu/m_e)^2$ times larger than that for electrons, which means that the *bremsstrahlung* interaction is crucial for high-energy electrons and positrons but not for high-energy muons. Hence, high-energy muons (μ) created in the atmosphere can survive in the atmosphere and reach the earth's surface without interacting with air nuclei. For instance, the decay length of muon (μ) with energy $E_\mu \sim 2.5$ GeV is ~ 15 km. On the other hand, a π^\pm with the same energy can barely go ~ 140 m before it decays to a μ and ν_μ , and the decay length of kaons (K^\pm, K^0) is about five times smaller than that of π^\pm due to the mass difference of kaons and π^\pm .

2.2.1 Electromagnetic Shower Development

In the EAS initiated by an EHE photon, the radiation process (*bremsstrahlung*) and ionization loss – for charged particles (e^+e^-) – and *pair production*, Compton scattering, and photoelectric effect – for γ rays – should be considered all together. Moreover, hadronic interactions as in Equation (2.1) are also possible, but they are suppressed by the factor of R . Until the energy of the charged particle (e^\pm) reaches to the critical energy E_c given as[20]

Table 2.1. π , K meson decay modes and fractions

	decay mode	fraction
π^\pm	$\mu^\pm \nu_\mu (\bar{\nu}_\mu)$	$\sim 99.99\%$
π^0	2γ	$\sim 98.8\%$
K^\pm	π^+, π^- π^\pm, π^0	$\sim 69\%$ $\sim 21\%$
K_s^0	π^+, π^- π^0, π^0	$\sim 69\%$ $\sim 31\%$
K_l^0	$3 \pi^0$ π^+, π^-, π^0 π^\pm, μ^\mp, ν π^\pm, e^\mp, ν_e	$\sim 21\%$ $\sim 13\%$ $\sim 27\%$ $\sim 38\%$

$$E_c \sim 710 \text{ MeV} / (Z + 0.92) \text{ for gases,}$$

at which the energy loss rates by the radiation and by ionization become equal, the radiational process is dominant. *Pair production* plays an exclusively important role for high-energy photons above the critical energy E_c ($\sim 80 - 90$ MeV in air). Hence, in the first approximation, called Approximation A, only these two processes, *bremsstrahlung* and *pair production*, are considered.[21] For example, for high-energy γ -rays and leptons (e^+e^-), the radiation length (ϵ_0)¹ for pair production from γ -rays is approximately equal to that for the bremsstrahlung of the leptons; hence, if D is the length at which the probability for pair production or for the bremsstrahlung is 1/2, then D should be $\epsilon_0 / \ln 2$ from the equation, $0.5 = \exp(-D/\epsilon_0)$. Now, if an EHE photon initiates an EAS, then after the first D length a pair of e^+ and e^- is created (*on average*) by pair production;

¹Defined as a length in units of g/cm^2 : after a particle (e^+ or e^-) passes through this length the survival probability of a particle in a medium is reduced by a factor of $1/e$.

after $2D$ lengths, two high energy photons are generated, and the energy of each particle is $E_o/4$ (*on average*); and so on. Therefore, the total number of particles after nD lengths is 2^n with an average energy of $E_o/2^n$. This cascade process continues until the average energy of leptons drops below the critical energy E_c . The number of D lengths to the shower maximum, N_{max} , can be evaluated as $\ln(E_o/E_c)/\ln 2$. Here, the shower maximum N_{max} is linearly dependent on the primary energy E_o as $N_{max} = E_o/E_c$.

A simple explanation such as the one above for a pure electromagnetic cascade process is good enough to understand the general cascade properties, but a real EAS profile may have considerable fluctuations and be quite different from the average expectations because the *average* is not meaningful enough for the small number of particles in the first few steps of the EAS.

The longitudinal development of a purely electromagnetic shower is described using an age parameter s which starts from 0 (at the first interaction), goes through 1.0 (at shower maximum), and reaches to 2.0 at the depth for which the shower vanishes. For example, the longitudinal development of an electromagnetic shower is written by Hillas[22] as follows:

$$N_e = \frac{0.31}{\sqrt{y}} \exp[t(1.0 - 1.5 \ln(s))], \quad (2.5)$$

where N_e is the number of electrons in the shower, t is the depth of the shower in radiation lengths(x_o);

$$y = \ln(E_o/E_c),$$

where E_o is the incident energy and E_c is the critical energy; and

$$s = \frac{3}{[1 + 2y/t]}$$

is the shower age. Figure 2.2 shows the Hillas profiles for the longitudinal development of pure electromagnetic showers. The straight line indicates constant shower age, $s = 1$, and each crossing point with the line represents the number of radiation lengths at the shower maximum for the initial energies 10^{15} , 10^{16} , 10^{17} , 10^{18} , and 10^{19} eV, respectively.

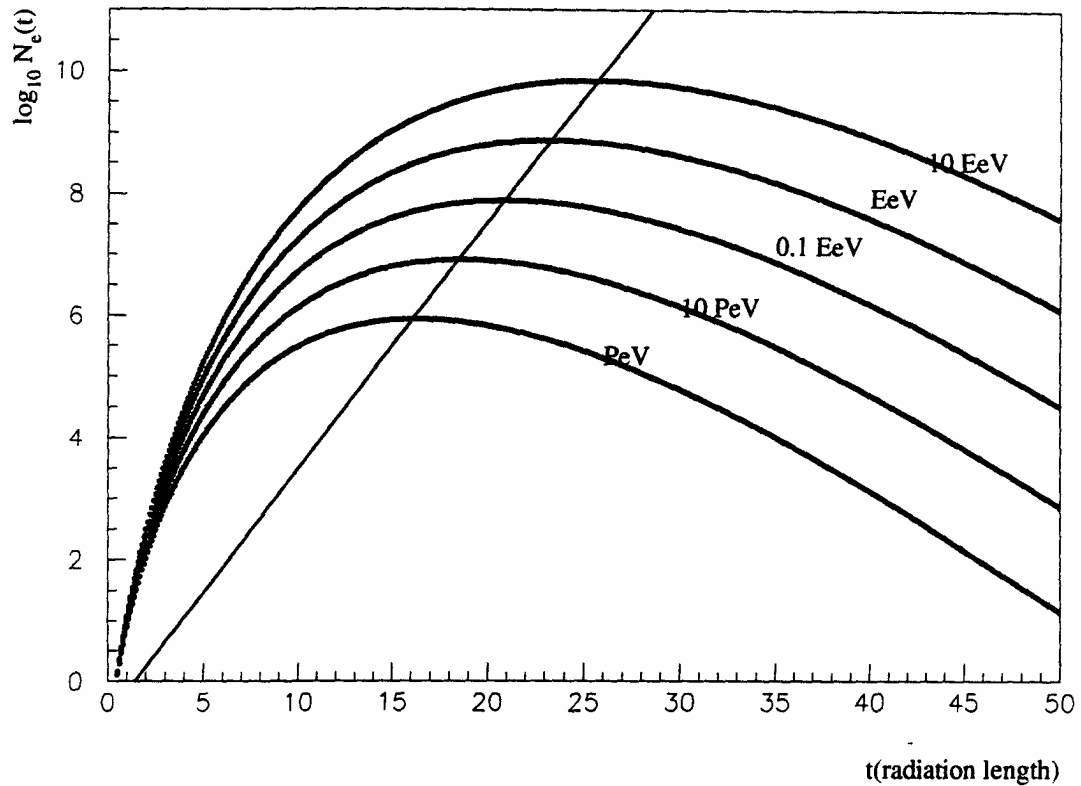


Figure 2.2. EM shower developments(10^{15} to 10^{19} eV)

2.2.2 Hadronic Shower Development

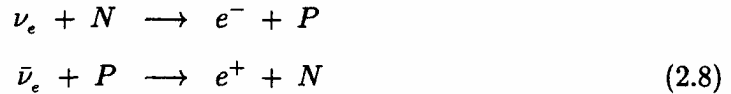
Hadronic showers consist of hadrons, mesons ($K^{\pm 0}$, $\pi^{\pm 0}$, etc.) and leptons (μ^{\pm} , e^{\pm}). The shower development depends on σ_{p-air}^{inel} (~ 530 mb at $10^{18} - 10^{19}$ eV) which determines the primary hadron's interaction length (~ 45 g/cm²) and $\sigma_{\pi-air}$ which determines the secondary pions interaction length. Relatively heavier particles such as hadrons and kaons stay close to the trajectory of the primary - hadronic core, but leptons or relatively lighter particles produce a conical-shaped shower profile - lateral distribution. From the decays of mesons given in Table 2.1 and especially from π^0 's ($\tau \sim 10^{-17}$ sec), individual electromagnetic showers keep being created and added to the shower profile; thus, as the cascade process develops the hadronic core gets smaller, and the electromagnetic shower part gets bigger and more dominant. As in the case of a pure electromagnetic shower, the number of particles N_{max} at shower maximum is still proportional to the primary energy E_o as[23]

$$N_{max} = (1.1 \text{ to } 1.6) E_o \text{ (GeV)}, \quad (2.6)$$

where the proportional constant depends on details of the hadronic model and incident particle composition. After the shower passes the shower maximum point the number of particles in the shower decreases exponentially due to *ionization loss*. For the longitudinal development of a proton initiated shower, an analytic expression is given by Gaisser and Hillas[24] as

$$N(X) = N_{max} \left(\frac{X - X_o}{X_{max} - X_o} \right)^{\frac{(X_{max} - X_o)}{\lambda}} \exp \left[-\frac{(X_{max} - X_o)}{\lambda} \right], \quad (2.7)$$

where X_o is the first interaction depth in air ($\sim 70 \text{ g/cm}^2$ for $\sim 10^{+15} \text{ eV}$ and $\sim 80 \text{ g/cm}^2$ for $\sim 10^{+18} \text{ eV}$) and $\lambda \sim 70 \text{ g/cm}^2$. Figure 2.3 shows the electromagnetic [Eq. (2.5)] and the hadronic shower profile initiated by EeV energy γ -ray and proton, respectively. In Equation (2.7), the first interaction depth X_o is assumed to be 80 g/cm^2 ; N_{max} , $1.1 \times 10^{+9}$ from Equation (2.6); and X_{max} , $\sim 780 \text{ g/cm}^2$ given by the Monte-Carlo (MC) prediction for protons.[25] For an electromagnetic shower, a radiation length (x_o) of 37.1 g/cm^2 and a critical energy (E_c) of 81 MeV are used. If an EeV energy electron neutrino ($\nu_e, \bar{\nu}_e$) interacts with a nucleon in the air, for instance,



the lepton (e^+, e^-) acquires $\sim 75\%$; and the outgoing nucleon, $\sim 25\%$ of the 1 EeV initial neutrino energy. Therefore, the EAS initiated by a neutrino interaction like Equation (2.8) is a superposition of electromagnetic and hadronic showers. In Figure 2.3 the profile represented by solid circles shows the mixture of 75% electromagnetic and 25% hadronic shower. Neutrino interactions are discussed in detail in Chapter 4 and Chapter 5.

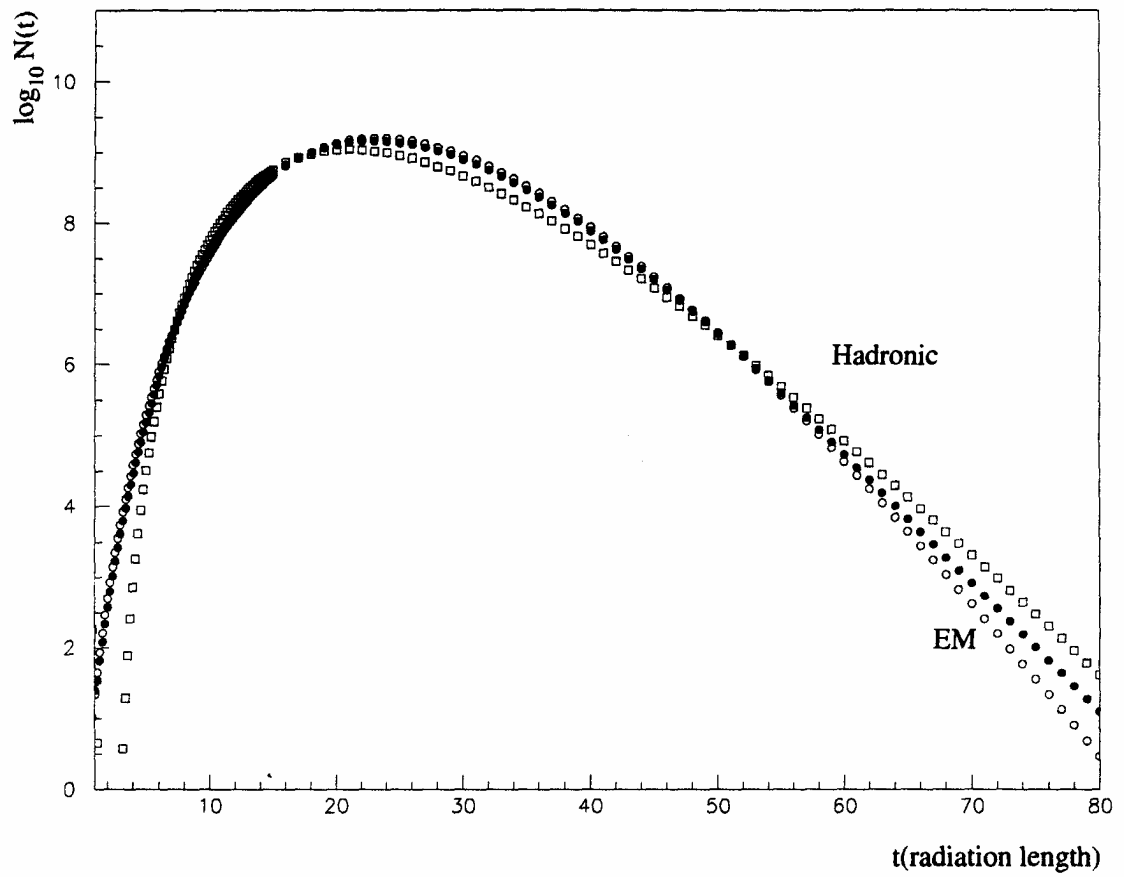


Figure 2.3. EM and Hadronic showers and their mixture

CHAPTER 3

LIGHT PRODUCTION AND PROPAGATION

Because of their small cross-section neutrinos can pass through the atmosphere¹ without interacting with atmospheric nuclei or electrons, and they can penetrate the earth all the way from the other side if their energy is less than a TeV. Even though the interaction probability is extremely small,² the interaction can happen in the atmosphere, and the resulting EAS is initiated by a single lepton (mainly e^\pm) and/or the hadron – the secondary particle in the neutrino-nucleon (ν, N) or neutrino-electron (ν, e) interaction – and develops through the cascade process as explained in Chapter 2. The EAS consists mainly of charged particles such as $K^\pm, \pi^\pm, \mu^\pm, e^\pm$, etc., and the charged particles are highly energetic. For example, before the EAS reaches the shower maximum X_{max} , the average energy of the particles $E \geq E_{th} \sim 81$ MeV; after X_{max} , the average energy begins to decrease to below E_{th} . Below E_{th} the energy loss of the shower particles is mainly by collisions with the atmospheric atoms and molecules – ionization and excitation.

3.1 Cherenkov Light

The velocity of a highly energetic shower particle exceeds the light velocity in the air, and excited atoms in the vicinity of the particles become polarized and coherently emit radiation at a characteristic angle θ , which is given as

$$\cos \theta = \frac{1}{\beta n}.$$

Here, β is v/c and n is the index of refraction. For standard temperature and pressure (STP) $n = 1.000293$, and θ_{max} is close to 1.3 degrees. The number of photons generated by a shower particle of energy E is given as[27]

¹Maximum horizontal depth : $\sim 7.3 \times 10^4$ g/cm².

²At $E \sim$ EeV; $\sigma(\nu, N) \sim 1.5 \times 10^{-32}$ cm², and $\sigma(p, p) \sim 1.3 \times 10^{-22}$ cm². [26]

$$\frac{dN_p}{dl} = 4\pi\alpha \left[1 - \left(\frac{E_{min}}{E} \right)^2 \right] \int \frac{\delta}{\lambda^2} d\lambda \text{ (photons/meter)}, \quad (3.1)$$

where α is the fine structure constant and $\delta = 1 - n$, E_{min} is Cherenkov threshold energy. If the shower particle is an electron and δ is small enough, $E_{min} \sim 0.511/\sqrt{2\delta}$ (MeV). For an isothermal atmosphere approximation $\delta = \delta_o e^{-h/H_o}$, where δ_o is the value of δ at the local surface ($\delta_o = 2.4 \times 10^{-4}$ at Fly's Eye altitude [860 gm/cm²]), and H_o is atmospheric scale height ($H_o \sim 7.3$ km).[27]

Cherenkov light contains a lot of ultraviolet photons due to the $\frac{1}{\lambda}$ dependence in Equation (3.1), and it is highly collimated along the shower axis. The Cherenkov light builds up along the shower front as the shower front propagates. Along the shower front, the size of the Cherenkov component depends on the history of the shower development, such as the energy of the cosmic ray particle, the first interaction depth(x_o), and the event geometry since the Cherenkov threshold energy depends on altitude. For scintillation detectors(the HiRes I detector) which measure fluorescence light to estimate the shower size along the shower track, the Cherenkov light is a nuisance since a correction must be made to estimate the exact shower size at each local position along the the shower track. Although it depends on the history of the shower development, as a general rule the Cherenkov component increases with the shower age.

3.2 Atmospheric Fluorescence Light

Atmospheric molecules can be excited or ionized by the charged particles in the EAS. The excited molecules either participate in collisional processes (nonradiative) or emit visible or ultraviolet photons (fluorescence) isotropically. Most of the fluorescence light (300 nm - 400 nm) comes from excited N_2 molecules and N_2^+ molecular ions.[28] Although there is a slight dependence on altitude and temperature, the fluorescence efficiency is $4 \sim 5$ photons/meter/electron.[29]

3.3 Propagation in the Atmosphere

Fluorescence light and Cherenkov light are attenuated by Rayleigh Scattering and Aerosol Scattering in the atmosphere until they finally reach the HiRes I detector.

3.3.1 Rayleigh Scattering

Rayleigh Scattering[27] is a relatively well-known process in the air.

$$\frac{dN_\gamma}{dl} = -\frac{\rho N_\gamma}{X_R} \left(\frac{400 \text{ nm}}{\lambda} \right)^4,$$

where X_R is the mean free path at $\lambda = 400 \text{ nm}$, and ρ is the air density given as

$$\rho = \rho_o \exp(-h/H_o)$$

for an isothermal atmosphere, in which $\rho_o = 0.00107 \text{ g/cm}^3$ at 0° C at Fly's Eye altitude, h is vertical height, and H_o is the scale height. The scattering probability into a given solid angle is given by

$$\frac{d^2 N_\gamma}{dl d\Omega} = \frac{3}{16\pi} \left| \frac{dN_\gamma}{dl} \right| (1 + \cos^2 \theta).$$

3.3.2 Aerosol Scattering (Mie Scattering)

Scattering of light by small particulate particles(aerosols) is not simple, and it depends on the aerosol size and shape. The aerosol size varies from $\sim 10^{-1} \mu\text{m}$ to $\sim 10^{+1} \mu\text{m}$, the size distribution is different from place by place, and the number density depends on weather condition, such as humidity and wind velocity. Most aerosols are concentrated near the surface of the Earth (the boundary layer).[30] The amount of scattered light from a beam of N_γ is approximately

$$\frac{dN_\gamma}{dl} \simeq \frac{N_\gamma \exp^{-h/h_M}}{l_M},$$

where h_M is the scale height, l_M is the mean free path which is function of wavelength. The angular distribution is also a function of wavelength and highly forward peaked as

$$\frac{d^2 N_\gamma}{dl d\Omega} \simeq a \exp^{-\theta/\theta_M} \left| \frac{dN_\gamma}{dl} \right|,$$

where typical values are $a = 0.80$ and $\theta_M = 26.7^\circ$. The mean free path (l_M) and the scale height (h_M) have been updated to be $l_M \sim 25 \text{ km}$ and $h_M \sim 1.0 \text{ km}$ [31] appropriate for the HiRes experiment at Dugway, Utah. This new result is used in the MC simulation.

CHAPTER 4

HIRES I DETECTOR

The HiRes I detector is located on top of Little Granite mountain at the U.S. Army Dugway proving ground in Utah, approximately 160 km southwest of Salt Lake City, Utah. Like the former Fly's Eye detector[27], but with much improved detector resolution and aperture size, HiRes I detector was designed to detect the passage of EAS in the atmosphere using the fluorescence light measurement.[32]

4.1 Detector Geometry and Mirror Optics

The HiRes I detector consists of 21 mirrors with which the detector covers the full azimuthal range of angles except for a half mirror azimuthal gap, and it looks up at the sky from ~ 3 to ~ 17 degrees in elevation. Each spherical mirror is formed by four of mirror segments like a four-leaf clover. The mirror has an effective area of 3.72 m^2 (area: 4.18 m^2), and the surface of the mirror is coated with silver. The reflectivity of fluorescence light (300 nm - 400 nm) on the silver coated surface is estimated to be ~ 0.8 . Each mirror looks at the moonless night sky. There is a PMT (photomultiplier tube) cluster box 4.5 m in front of the mirror surface. The PMT cluster box consists of 256 hexagonal PMTs and electronics for the PMTs. The surface of the cluster box pointing towards the mirror surface is called the cluster plane, and the cluster plane vector starting at the center of the cluster plane is on the mirror axis. The 256 PMTs are assembled in a honeycomb structure on the cluster plane. Figure 4.1 shows the honeycomb structure on the cluster plane. The solid angle coverage, $\Delta\Omega$, for each PMT is approximately $2.39 \times 10^{-4} \text{ str}$ which corresponds to $\sim 1^\circ \times 1^\circ$.¹ With 256 PMTs for each mirror and 21.5 mirrors the HiRes I detector covers $\sim 21\%$ of the night sky.

Light, composed of fluorescence light, Cherenkov light, and background noise, is reflected from the mirror, and some of it reaches the cluster plane. After passing through the UV bandpass filter (300 nm - 400 nm) only fluorescence light, some fraction of Cherenkov

¹ $\Delta\Omega = 2 \pi \int_{0.0^\circ}^{0.5^\circ} \sin(\theta) d\theta.$

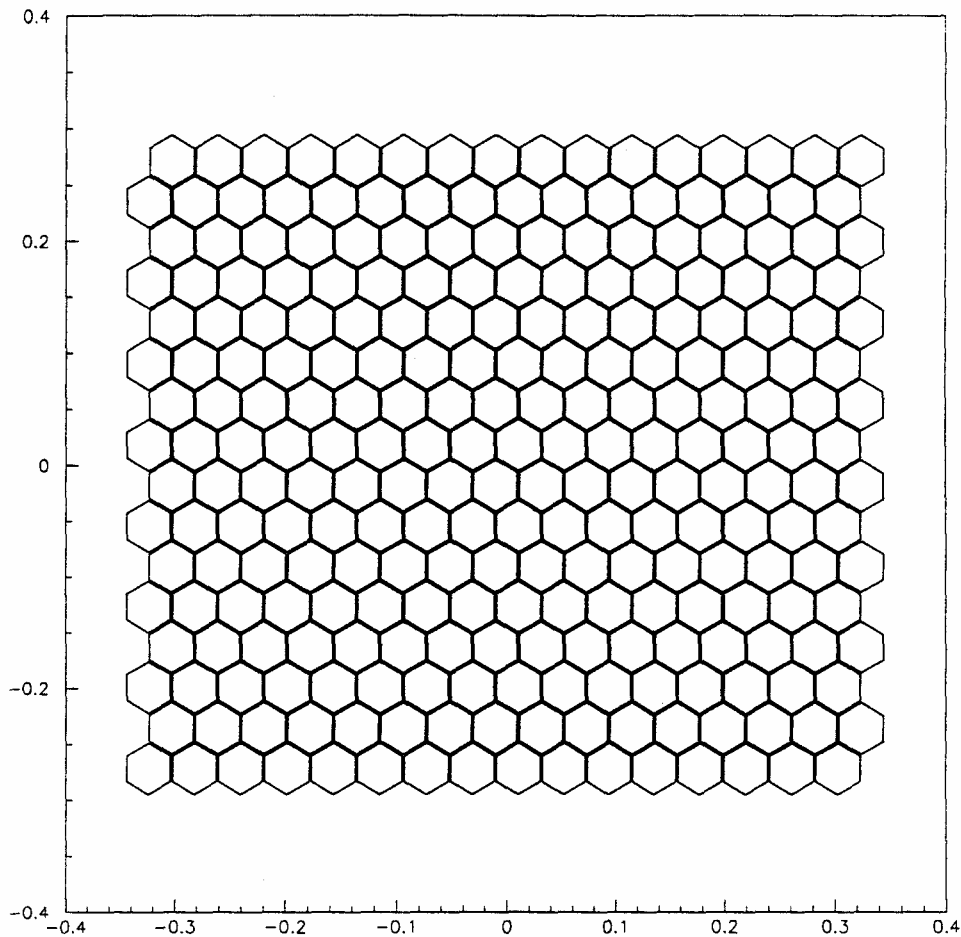


Figure 4.1. Cluster plane (meter scale); each tube size has ~ 4 cm diameter

light, and some UV noise impinge on the PMTs. If the light signal came from a remote distance the light is focused by the spherical mirror, and an image spot is produced on the cluster plane. Depending on the incident direction of light, the spot size and the shape changes due to spherical aberration. The cluster plane is located at a distance so as to minimize these changes.

4.1.1 Spot Size and Shape

The spot size of the image on the PMT cluster plane depends on the incident direction of light. Using the ray-tracing method, the position, size, and shape of the image can be simulated. Figure 4.2 shows the size and shape of the spot depending on the incident

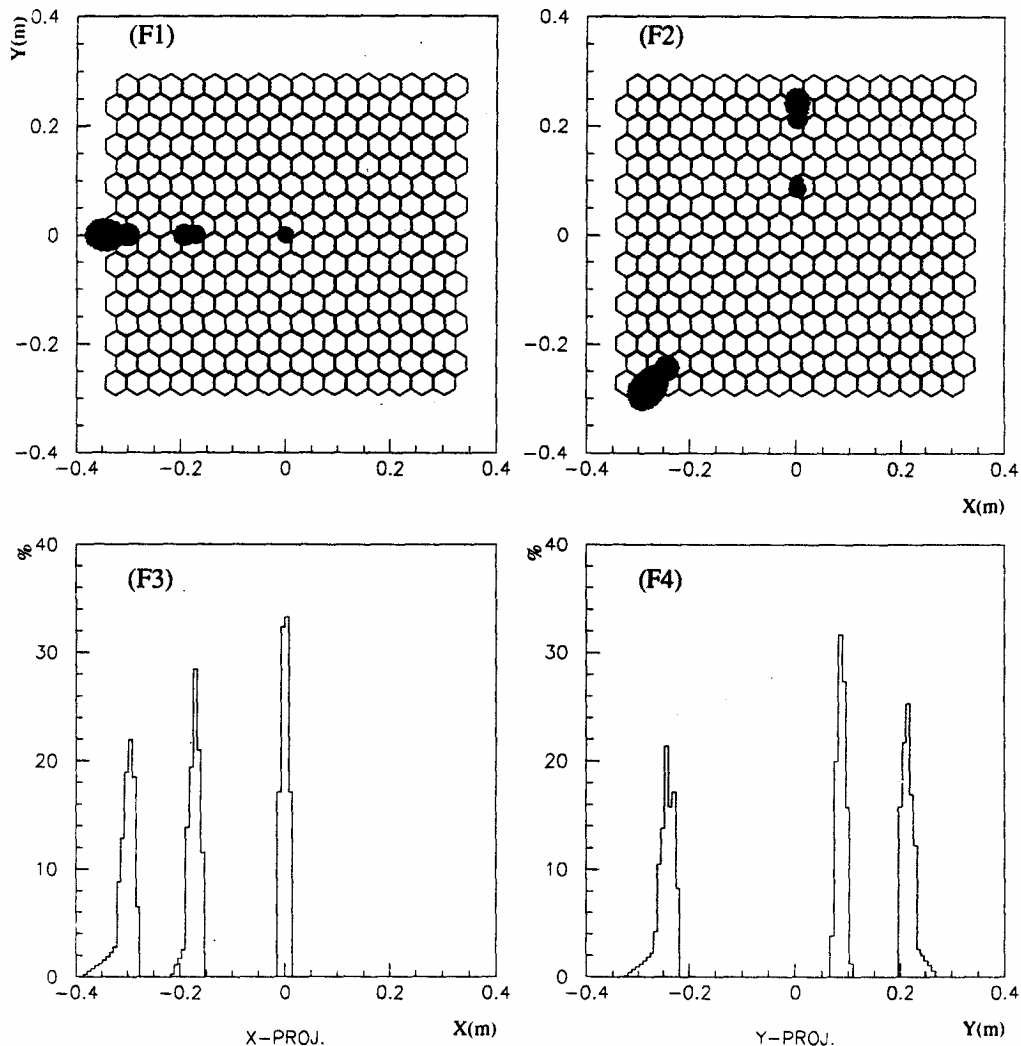


Figure 4.2. Spot size and the shadow effect: 0, 4, and 7 degrees off the mirror axis(F1) and the corresponding X-axis projections in (F3); 2, 5, and 8 degrees off the mirror axis(F2) and their Y-axis projections (F4). the spot for 8 degrees off the mirror axis is shown at left below in (F2).

angle on the mirror. The effective area of the spot varies from ~ 3 cm (tube size ~ 4 cm) to ~ 4 cm in diameter over most of the mirror and reaches to ~ 8 cm in overall length at the edges. In Figure 4.2 (F3), the first plot shows the largest diameter, corresponding to an incident direction 7 degrees off from the mirror axis, and the smeared part (less than $\sim 2\%$) which reaches to ~ 8 cm.

The shape of the spot changes depending on the incident direction of light. Like a

shadow effect the further the distance from the center of the cluster plane, the more distortion of the spot image can be expected.

4.2 Photomultiplier Tube(PMT) Response

A photomultiplier tube is a well-known device used to convert a light pulse (scintillation light) into a corresponding electric signal.[33] Once incident light hits the photocathode, a few photoelectrons come out of the photo-cathode material(*photoelectric effect*), these electrons go through the dynode chain where the number of electrons are multiplied(*cascade process*). Finally those electron cascade reaches the anode and the preamplifier reads the electric signal. When light hits the photocathode, the quantum efficiency (QE) is given as

$$\text{QE} = \frac{\text{number of photoelectrons}}{\text{number of incident photons}}$$

The quantum efficiency depends on the wavelength of the light and the material of photocathode, and ranges from 20% to 30%. For HiRes I detector there are two types of PMTs² being used, and the overall quantum efficiency for those PMTs is $\sim 20\%$. However, the quantum efficiency is not uniform over the photocathode surface.

The electric signal passes through the preamplifier and shaping amplifier with a Gain(G) given as

$$G = e^{\alpha} V^{\beta},$$

where V is high voltage and the constants (α, β) are determined through a tube calibration procedure done at the University of Utah. For the HiRes I detector, $\alpha = -31.70 \pm 0.77$ and $\beta = 5.89 \pm 0.14$ (1σ error in Gaussian distribution) and the Gain is $\sim 10^5$ [34].

4.2.1 Background Noise and PMT Threshold

Even on moonless night there is background noise due to scattered star light, diffuse radiation from the galaxy, sun light scattered by interplanetary matter, photochemical atmospheric light, and man-made light pollution. The night sky background noise for HiRes I is ~ 40 photons/ $(\mu\text{s m}^2)$ for the 300-400 nm bandpass and 1° field of view. The noise signal for each PMT is then ~ 24 pe/ μs (QE : 0.2, mirror reflectivity: 0.8, mirror

²Manufacturer: EMI, Philips.

area: 3.72 m^2). To suppress noise triggering and optimize the detector for cosmic ray events HiRes I has a variable trigger threshold for each mirror, which is adjusted every ~ 4 sec so that the tube trigger rates are kept at 200 Hz.

To discriminate against noise triggers, HiRes I has two channels in trigger analog shaping for each PMT – a 100 ns single pole RC filter (Channel A) and a 375 ns 3-pole LC Bessel filter (Channel B). Channel A is optimized for an EAS near the detector; and channel B, for remote EAS. However, HiRes I presently uses only channel B to optimize for remote showers. On average, 8.93 pe is expected for the noise signal in the 375 ns time window. This corresponds to a 7.5×10^{-5} tube trigger probability in each time window. If the noise signal follows Poisson statistics, the threshold for the cosmic ray events corresponds 22.5 pe / 375 ns. Hence, the threshold is set to more than 4.5σ above the average noise signal ($\sigma = 2.99$ pe). Similarly, if channel A is used with the 100 ns RC filter, on average 2.4 pe is expected for the noise signal in the 100 ns time window (100 ns RC filter), and this corresponds to a threshold set at 5.9σ ($\sigma = 1.55$) for a trigger rate of 200 Hz.

The night sky noise changes with the environmental situation as mentioned above, and a seasonal variation is also expected. That means that the mirror threshold also changes with the environmental situation since HiRes I has fixed mirror trigger rates. Figure 4.3 and Figure 4.4 show the mirror thresholds and the seasonal variations (09/04/1999 - 11/07/2000) in the HiRes I detector[35], and the average threshold is summarized in Table 4.1. In the MC study for the neutrino events, the average threshold values in Table 4.1 are used since the fluctuations can be ignored compared with other uncertainties in the MC.

4.3 Events in the Detector

HiRes I uses one of the following preprogrammed patterns to distinguish cosmic ray events from noise triggers: For subcluster³ triggers, three tubes with two being adjacent are required; for mirror triggers, at least two subclusters must trigger within a predefined time window. HiRes I has two channels, channel A has $1.2 \mu\text{s}$ and channel B has $5.6 \mu\text{s}$ integration gate widths, respectively. To optimize the detector for remote EHE cosmic ray events, the $5.6 \mu\text{s}$ gate widths has been used with $1.6 \mu\text{s}$ delay. Using the detector calibration data these integrated charges can be converted to the corresponding number

³Each cluster has 16 subclusters(4×4).

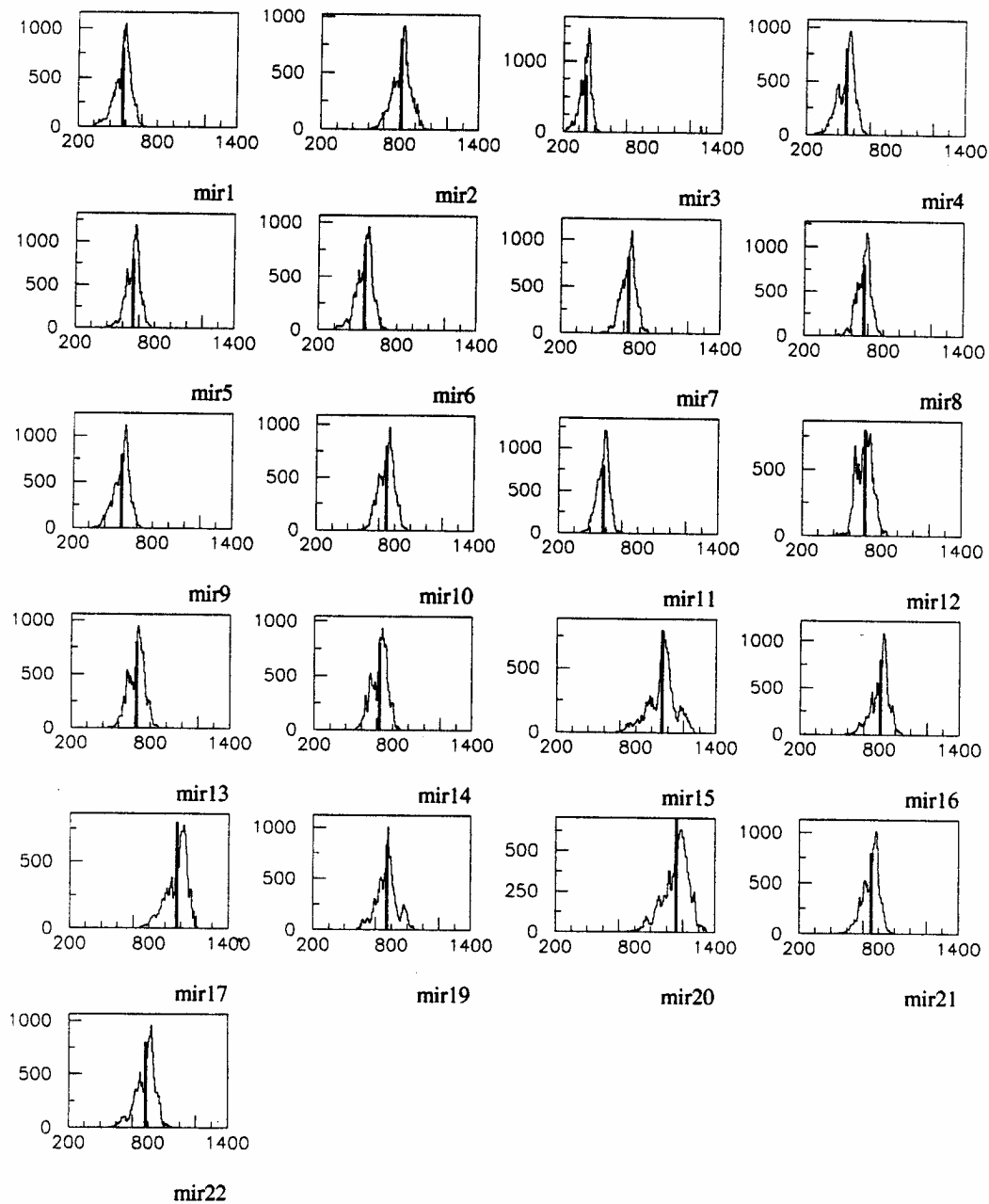


Figure 4.3. Mirror threshold distributions; the vertical lines indicate average thresholds(mV) for the period of (09/04/1999 - 11/07/2000)

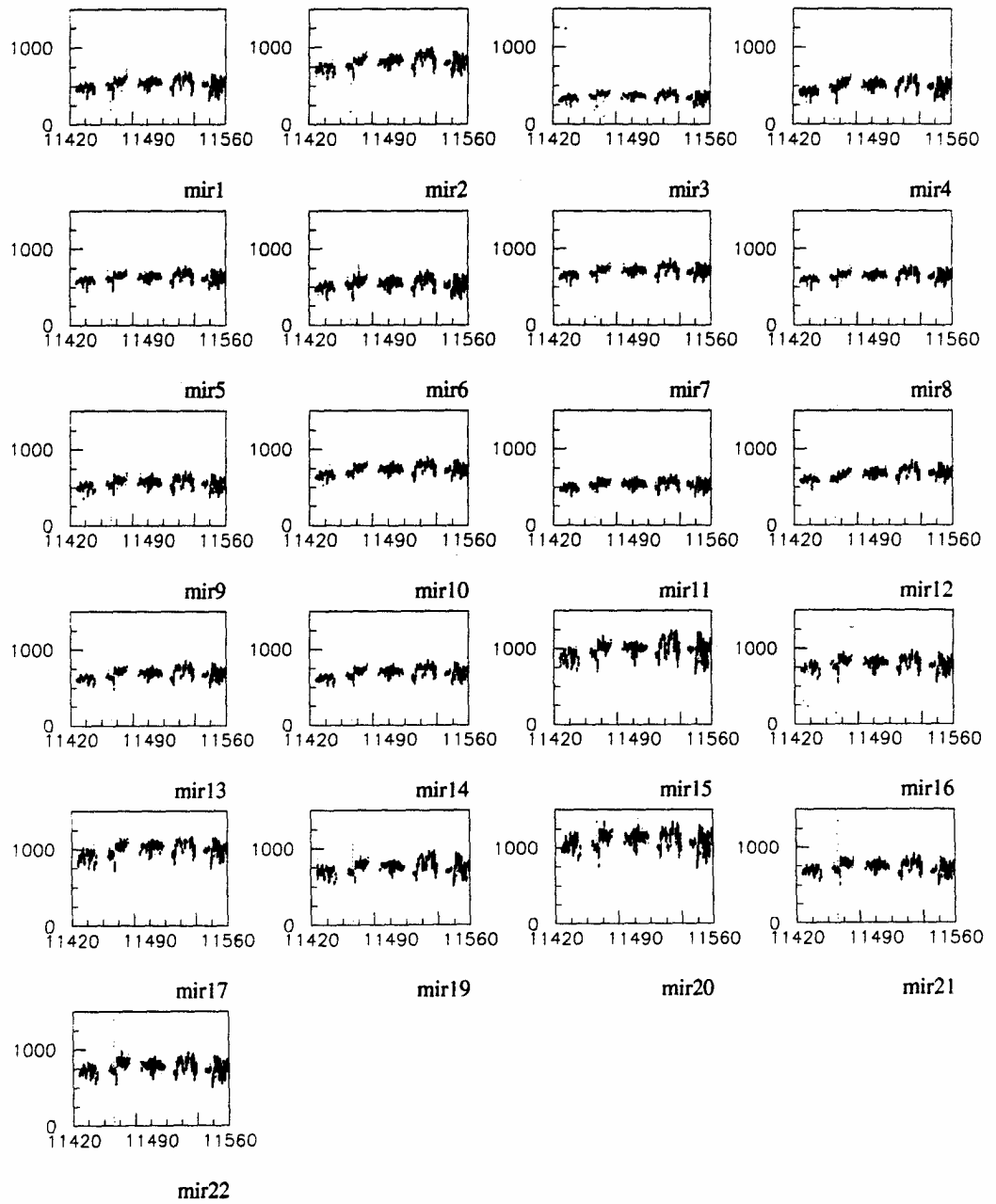


Figure 4.4. Mirror threshold(mV) variations on julian dates from 09/04/1999 to 11/07/2000

Table 4.1. Average mirror thresholds(mV) in HiRes I detector(09/04/1999 - 11/07/2000)

mir1	mir2	mir3	mir4	mir5	mir6	mir7	mir8	mir9	mir10
541.4	812.7	372.5	500.7	636.8	552.9	713.7	651.9	567.6	736.3
mir11	mir12	mir13	mir14	mir15	mir16	mir17	mir18	mir19	mir20
538.1	676.3	694.3	696.6	999.3	806.5	1011.0	-	759.2	1118.0
mir21	mir22								
742.7	783.5								

of photo-electrons at the PMT cathode and to the corresponding number of photons arriving in the field of view (~ 1 degree) of the PMT along the shower track.

If a subcluster tube is triggered, constant current time charging begins for the tube, and the tube's individual trigger flag is set for at least $25 \mu\text{s}$. When a mirror trigger is formed, the hold-off time for all triggered tubes is extended an additional $10 \mu\text{s}$. Each triggered PMT time information can be determined from the constant current time charging data.

For each event, the PMT time information and the integrated charges are converted to QDC (charge-to-digital converter) and TDC (time-to-digital converter) values, respectively. For each triggered PMT, the QDC and TDC are recorded as raw data. Details in mirror electronics and the detector calibration can be found in reference [36].

4.4 Event Selection and Data Flow

The raw data file is not in time sequence but depends on the traffic condition over the network. Hence, the first stage of processing(PASS0) is time matching and grouping the packet to form events. The second stage(PASS1) is event calibration: Raw TDC values are converted to a PMT-triggered time (in microseconds) measured from the time of the mirror trigger (delayed by $50 \mu\text{s}$). The raw QDC values are converted to the number of photo-electrons using *gain* and *offset* values from the detector calibration. Since there are lots of noise-triggered events, a filtering process is necessary; hence, the next stage(PASS2) is event selection (*Rayleigh Filter*) which uses statistics to distinguish noise triggers (random in tube time sequence) and cosmic ray events (not random in tube time sequence)[36]. In PASS2, noise triggers are filtered out and cosmic ray events are kept with 99.9% efficiency. Out of ~ 52 million triggered events from May 1997 to June 1999 only ~ 2.3 million events passed through PASS2[36] and were categorized to three

separate files: downward-going, horizontal, and upward-going.

Human made artificial events, such as Xenon flashers and YAG laser events for atmospheric monitoring, are still included in the data sets of horizontal and upward-going events at this point.

CHAPTER 5

COSMIC NEUTRINOS

Cosmic neutrinos originate from outer space in contrast to neutrinos produced in cosmic-ray interactions with atmospheric nuclei. According to neutrino production models based on AGNs (Active galactic nuclei) and GRBs (Gamma Ray burst) and the program ATM[12] for the generation of atmospheric neutrinos, the cosmic neutrino flux should dominate the atmospheric neutrinos flux for neutrino energies above 1.0×10^{15} eV. In fact, there is no clear cut way to distinguish cosmic neutrinos from atmospheric neutrinos on an event-by-event basis, but we assume that neutrinos with energy above 1.0×10^{15} eV are of cosmic origin because the atmospheric neutrino flux is predicted to be extremely low above this energy.

5.1 The Spectrum Models

Several muon neutrino spectra – summarized by Raj Gandhi, *et al.* in 1998[39] – from AGN and GRB models (AGN-M95, AGN-SS91, AGN-P96, GRB-WB) are used for the reference spectrums in the Monte Carlo (MC) simulation for the HiRes I detector in Utah. Figure 5.1 shows these $(\nu_\mu + \bar{\nu}_\mu)$ spectrums from the models evaluated at the earth's surface. There have been many cosmic neutrino spectrum models and neutrino events expectation calculations.[38, 39] AGNs are the most powerful radiation sources in the universe. They act as cosmic-ray accelerators and get powered by the gravitational energy of matter falling in upon a supermassive black hole. However, Eli Waxman and John Bahcall recently suggested an upper bound on the high-energy cosmic neutrino flux, which is based on cosmic rays observation.[40] Their upper limit is two orders of magnitude below the intensity predicted in the AGN jet model[41] and is consistent with the GRB model.[42] Nonetheless, it is not yet clear which model is close to reality. In these models the cosmic neutrinos are created mainly from *pion photo-production*

$$p + \gamma \longrightarrow \pi^0 \text{ or } \pi^\pm + \text{anything}, \quad (5.1)$$

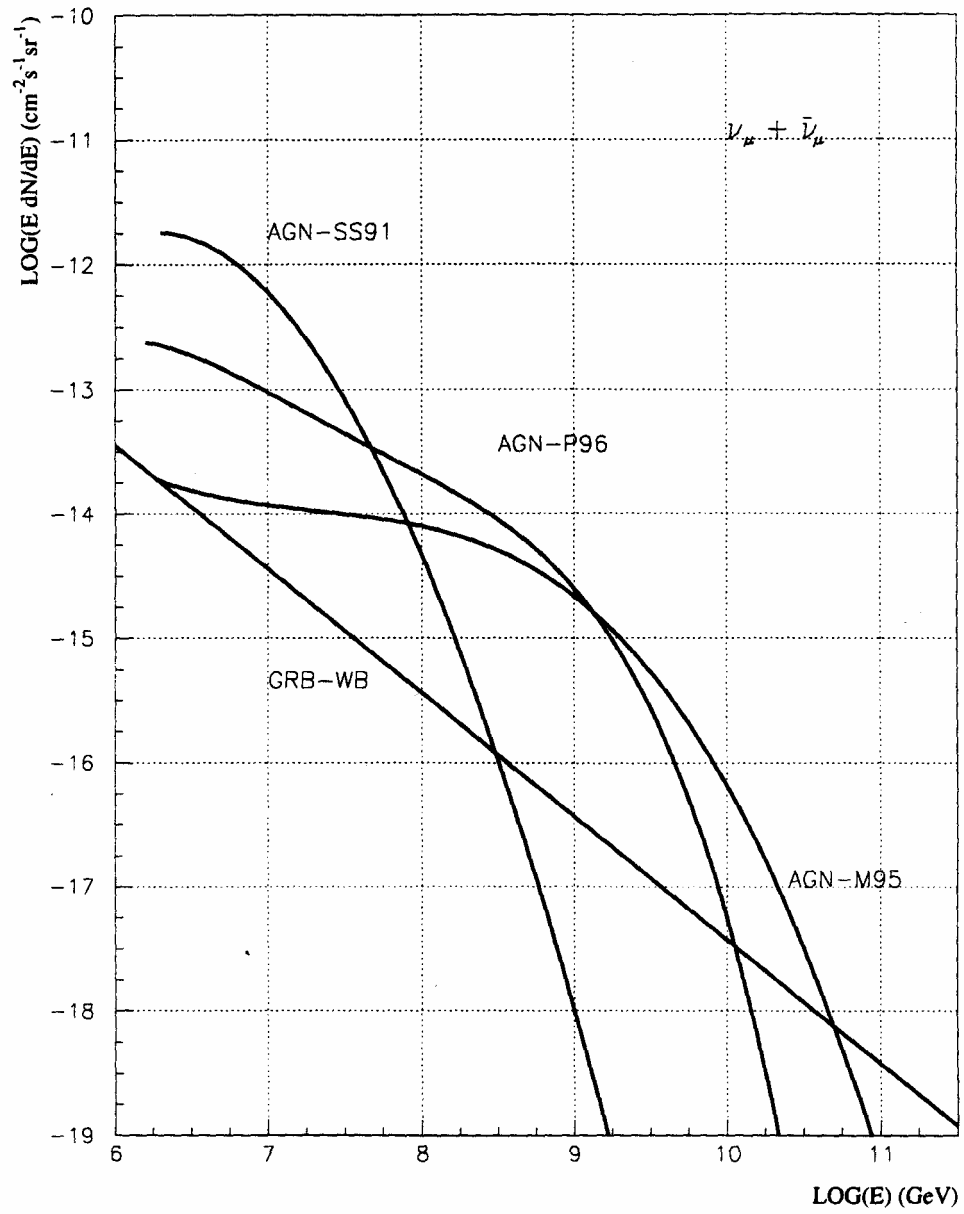


Figure 5.1. Differential flux of muon neutrinos ($\nu_\mu + \bar{\nu}_\mu$)

where UHE protons interact with UV photons near UHE cosmic ray source like an AGN. The pions decay via

$$\pi^0 \longrightarrow \gamma + \gamma \quad (5.2)$$

$$\pi^\pm \longrightarrow \mu + \nu_\mu, \quad (5.3)$$

and

$$\mu \longrightarrow e + \nu_e + \bar{\nu}_\mu. \quad (5.4)$$

Hence, the number of electron neutrinos ($\nu_e + \bar{\nu}_e$) created from pion photo-production [Eq. (5.1)] should be 50% of the number of muon neutrinos ($\nu_\mu + \bar{\nu}_\mu$). If the pions (π^0, π^+, π^-) are produced in equal numbers, UHE γ -rays are also produced in equal number to electron neutrinos ($\nu_e + \bar{\nu}_e$)

$$2\gamma : 2\nu_\mu : 2\bar{\nu}_\mu : 1\nu_e : 1\bar{\nu}_e.$$

In general, it is assumed that the flux intensity of $\nu_e + \bar{\nu}_e$ should be $\sim 50\%$ of the muon neutrino flux intensity of $\nu_\mu + \bar{\nu}_\mu$ in Figure 5.1.[39]

5.2 Neutrino - Nucleon Interactions

Cosmic neutrinos can interact with nucleons or electrons in the atmosphere and inside the earth. The interaction, (νN) or (νe^-) is the weak interaction (WI) mediated by the W^\pm or Z^0 boson; hence, it is categorized as a Charged Current (CC) or a Neutral Current (NC) interaction if mediated by W^\pm and Z^0 bosons, respectively.

5.2.1 Neutrino Cross Section

The cross section of an UHE neutrino with a nucleon is not yet precisely known because the cross section cannot be measured in any contemporary accelerator on the earth (the maximum beam energy is \sim a few TeV in the TEVATRON), but it has been evaluated using the **parton** model[39, 43, 44, 45, 46]. For instance, in UHE electron-proton ($e p$) interactions (*deep inelastic interaction*) we can resolve the individual quarks inside the proton if we can keep increasing the center of mass energy of the system. Now, as an extreme case, let us consider an infinite-momentum frame of reference, in which the

constituents of the proton become pseudo-free (incoherent)¹ due to the *time dilation* in Special Relativity. The ($e p$) interaction is *instantaneous* if the velocity of the intermediate boson, which is a photon (γ) in this case, is close to the velocity of light in free space. The individual constituents of a proton(or a nucleon in general) are called *partons* in the infinite-momentum frame of reference, and only one parton² is supposed to participate in the interaction because the parton is an almost free particle.³ Therefore, the form factor of the *deep inelastic interaction* has a simple form, that is a δ -function for the structureless point particle, and depend **only** on the *momentum fraction*, $x = Q^2/2M\nu$ ⁴. The Bjorken scaling variables, $x = Q^2/2M\nu$ and $y = \nu/E_\nu$, are thus naturally introduced.

It is assumed that the above reasoning for ($e p$) interaction is *approximately* valid for the weak interactions as well. The Bjorken scaling variables are now $x = Q^2/2M\nu$ and $y = \nu/E_\nu$, in which $-Q^2$ is the invariant momentum transfer between incident neutrino and outgoing lepton and $\nu = E_\nu - E_{lep}$ is the energy loss in the lab frame(target). The inclusive differential cross section for the CC reaction, $(\nu N) \rightarrow \text{lepton}(e, \mu, \text{etc}) + \text{anything}$, where $N \equiv \frac{n+p}{2}$ is an isoscalar nucleon, is given as[39]

$$\frac{d^2\sigma}{dx dy} = \frac{2G_F^2 M E_\nu}{\pi} \left(\frac{M_W^2}{Q^2 + M_W^2} \right)^2 \left[xq(x, Q^2) + x\bar{q}(x, Q^2)(1-y)^2 \right], \quad (5.5)$$

and the NC reaction, $(\nu N) \rightarrow \nu + \text{anything}$, is given as[39]

$$\frac{d^2\sigma}{dx dy} = \frac{G_F^2 M E_\nu}{2\pi} \left(\frac{M_Z^2}{Q^2 + M_Z^2} \right)^2 \left[xq^o(x, Q^2) + x\bar{q}^o(x, Q^2)(1-y)^2 \right], \quad (5.6)$$

where M is the the nucleon mass; M_W and M_Z are the intermediate-boson masses; $G_F = 1.16632 \times 10^{-5} \text{GeV}^{-2}$, Fermi constant; and $q(x, Q^2)$, $\bar{q}(x, Q^2)$, $q^o(x, Q^2)$, and $\bar{q}^o(x, Q^2)$ are the quark and antiquark distributions from model CTEQ4-DIS[39]. For $10^{16} \text{ eV} \leq E_\nu \leq 10^{21} \text{ eV}$, the CC (charged current), NC (neutral current), and the total cross section for νN (neutrino Nucleon) interaction are given within 10% by

¹It is essentially a free particle, not interacting with its friends in the proton.

²Structureless, i.e., a point particle.

³We assume that $P_\tau \sim 0$ in the interaction.

⁴ $-Q^2$ is the invariant momentum transfer between the incident and outgoing electron and $\nu = \Delta E$, the energy loss in the proton rest frame.

$$\begin{aligned}
\sigma_{CC}(\nu N) &= 5.53 \times 10^{-36} \text{cm}^2 \left(\frac{E_\nu}{1 \text{ GeV}} \right)^{0.363} \\
\sigma_{NC}(\nu N) &= 2.31 \times 10^{-36} \text{cm}^2 \left(\frac{E_\nu}{1 \text{ GeV}} \right)^{0.363} \\
\sigma_{tot}(\nu N) &= 7.84 \times 10^{-36} \text{cm}^2 \left(\frac{E_\nu}{1 \text{ GeV}} \right)^{0.363} .
\end{aligned} \tag{5.7}$$

Similarly, the cross sections for $\bar{\nu}N$ (antineutrino Nucleon) are

$$\begin{aligned}
\sigma_{CC}(\bar{\nu}N) &= 5.52 \times 10^{-36} \text{cm}^2 \left(\frac{E_\nu}{1 \text{ GeV}} \right)^{0.363} \\
\sigma_{NC}(\bar{\nu}N) &= 2.29 \times 10^{-36} \text{cm}^2 \left(\frac{E_\nu}{1 \text{ GeV}} \right)^{0.363} \\
\sigma_{tot}(\bar{\nu}N) &= 7.80 \times 10^{-36} \text{cm}^2 \left(\frac{E_\nu}{1 \text{ GeV}} \right)^{0.363} .
\end{aligned} \tag{5.8}$$

For high energies the cross section depends on the effective lower limit in x . To study the effective lower limit in x with neutrino energy, let $Q^2 \rightarrow M_W^2$ (W-propagator damping); hence, $x = M_W^2/2MyE_\nu$. If we use the average inelasticity, $\langle y \rangle$, which ranges from 0 to 1 and changes slowly with the neutrino energy, the effective lower limit, $x_c \sim M_W^2/2M\langle y \rangle E_\nu$. For instance, for a neutrino energy of 1.0×10^6 GeV x_c is $\sim 1.3 \times 10^{-5}$ ($\langle y \rangle \sim 0.27$), and for 1.0×10^{11} GeV x_c is $\sim 1.7 \times 10^{-7}$ ($\langle y \rangle \sim 0.2$), respectively. However, for large Q^2 the contribution of *sea* quarks increases at small x values when $x \rightarrow 0$. It is difficult to reach this small value of x_c in experiments (the limit is $x_c \sim 10^{-4}$) and an extrapolation method is used to get the information for the remaining part of small x . Naturally, the uncertainty of the (νN) cross section is bigger with increasing neutrino energy. For 10^{11} GeV neutrino the estimate of the uncertainty reaches a factor of ~ 2 .

Since the lepton (electron or positron) and the secondary nucleon from (ν_e, N) or $(\bar{\nu}_e, N)$ interaction (CC) can initiate EASs independently, the energies of the lepton and the nucleon should both be considered. These energies can be estimated using the inelasticity factor (y) distribution which can be evaluated from Eq. (5.5). The average of the inelasticity factor, $\langle y \rangle$, goes from ~ 0.25 (at $E_\nu \sim 10^{16}$ eV) to ~ 0.20 (at $E_\nu \sim 10^{20}$ eV), which corresponds to a nucleon energy of between $\sim 25\%$ and $\sim 20\%$ of the incident neutrino energy and a lepton energy of between $\sim 75\%$ and $\sim 80\%$, respectively. Moreover, the secondary nucleon from muon neutrino interactions (CC or NC), such as (ν_μ, N) and $(\bar{\nu}_\mu, N)$ interactions, and from NC interactions such as (ν_e, N) and $(\bar{\nu}_e, N)$ also can initiate an EAS. As in the CC interaction, the energy distribution of the nucleon

can be estimated from the inelasticity factor (y) using Eq. (5.6). The y distribution is quite similar to the CC interaction for neutrino energy above $1.0 \times 10^{+15}$ eV.

5.2.2 The 6.3 PeV $\bar{\nu}_e$ Resonance and Electron Interaction

In general the neutrino-electron interactions, (νe) or $(\bar{\nu} e)$, can be neglected compared to the neutrino-nucleon interactions (νN) due to the small mass of electron.[45] However, there is a resonance effect in $(\bar{\nu}_e e)$ interactions, in which the intermediate boson W^- is produced at around 6.3 PeV(neutrino energy in lab. system) and the resonance region is $\sim 5.7 \text{ PeV} \leq E_\nu \leq \sim 7.0 \text{ PeV}$. The cross section of $(\bar{\nu}_e e)$ at 6.3 PeV is larger than the neutrino-nucleon (νN) cross section for the same energy (by ~ 40 times), but also at any energy up to 10^{+21} eV. Considering that the cosmic neutrino spectra in Figure 5.1 are exponentially decreasing, the production of possible neutrino events at around 6.3 PeV energy cannot be ignored. In the resonance $(\bar{\nu}_e e)$ interaction, the W^- boson, right after its creation, decays to hadrons or leptons. According to the branching ratios of the W^- boson decay modes, the decay probability to the hadrons $(\bar{\nu}_e e \rightarrow \text{hadrons})$ is ~ 6 times bigger than to the leptons $(\bar{\nu}_e e \rightarrow \bar{\nu}_l l)^5$. Table 5.1 shows the cross sections of $(\nu_e e)$ and $(\bar{\nu}_e e)$ interactions for 6.3 PeV energy neutrino (antineutrino).

For the HiRes I detector, the muonic decay mode $(\bar{\nu}_\mu \mu)$ can be ignored, since the muon does not produce a shower effectively,⁶ and since it has a relatively long lifetime. The tau lepton in $(\bar{\nu}_\tau \tau)$ decay mode needs to be considered because of its short lifetime ($c\tau = 87.11 \mu\text{m}$). At these PeV energies the τ lepton cannot go further than ~ 50 m

Table 5.1. Neutrino-electron interactions at 6.3 PeV

Reaction	cross section $\sigma(\text{cm}^2)$
$\nu_e e \rightarrow \nu_e e$	3.10×10^{-35}
$\bar{\nu}_e e \rightarrow \bar{\nu}_e e$	5.38×10^{-32}
$\bar{\nu}_e e \rightarrow \bar{\nu}_\mu \mu$	5.38×10^{-32}
$\bar{\nu}_e e \rightarrow \bar{\nu}_\tau \tau$	5.38×10^{-32}
$\bar{\nu}_e e \rightarrow \text{hadrons}$	3.41×10^{-31}
$\bar{\nu}_e e \rightarrow \text{anything}$	5.02×10^{-31}

⁵Decay to one neutrino-lepton pair.

⁶Pair production is slightly more important and hadronic interaction is about a factor of three less important than bremsstrahlung.[48]

before it decays to $(\nu_\tau \text{ hadrons})$, or $(\nu_\tau \bar{\nu}_l l)$, etc., the secondary hadronic shower or electromagnetic shower should be considered for the HiRes I detector. However, the combined probability that the W^- boson decays to $(\tau \nu_\tau)$ ($\sim 10\%$, Table 5.1) and the τ decays to ν_τ with hadrons ($\sim 65\%$ [47]) or $(e \nu_e)$ ($\sim 18\%$ [47]) is small if compared to other cases, such as $(\bar{\nu}_e e \rightarrow W^- \rightarrow \text{hadrons})$ or $(\bar{\nu}_e e \rightarrow W^- \rightarrow \bar{\nu}_e e)$. It is about 1.5% for $(\bar{\nu}_e e \rightarrow W^- \rightarrow \bar{\nu}_\tau \tau, \text{ and } \tau \rightarrow \nu_\tau \bar{\nu}_e e)$ and about 6.5% for $(\bar{\nu}_e e \rightarrow W^- \rightarrow \bar{\nu}_\tau \tau, \text{ and } \tau \rightarrow \nu_\tau \text{ and hadrons})$. Through the decay of τ lepton the energy for the shower generation is small due to the τ neutrino energy at the final stage.

Figure 5.2 shows the resonance effect in the cross sections of $(\bar{\nu}_e e \rightarrow \bar{\nu}_e e)$, $(\bar{\nu}_e e \rightarrow \bar{\nu}_\tau \tau)$, and $(\bar{\nu}_e e \rightarrow \text{hadrons})$, and Figure 5.3 shows the secondary lepton energy fraction acquired from the incident neutrino energy and the angular distribution in the interaction of $(\bar{\nu}_e e \rightarrow \bar{\nu}_e e)$. On average, the secondary lepton acquires about 25% of the incident neutrino energy.

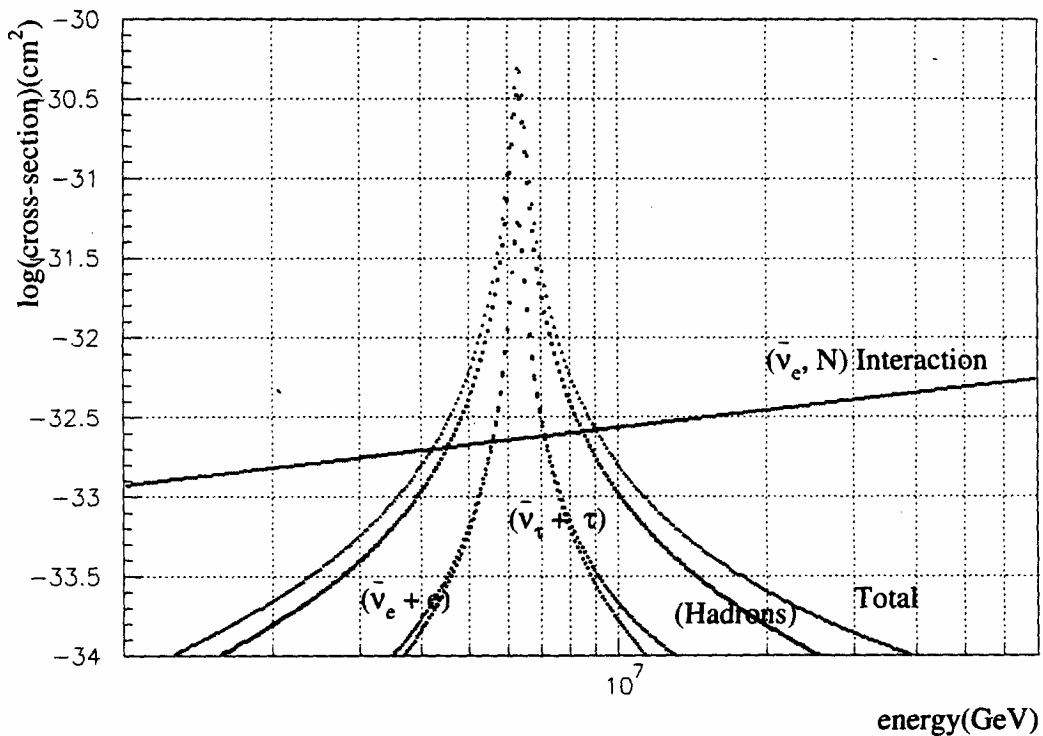


Figure 5.2. $\bar{\nu}_e e \rightarrow \bar{\nu}_e e$, $\bar{\nu}_e e \rightarrow \bar{\nu}_\tau \tau$, $\bar{\nu}_e e \rightarrow \text{hadrons}$, $\bar{\nu}_e N$ interaction

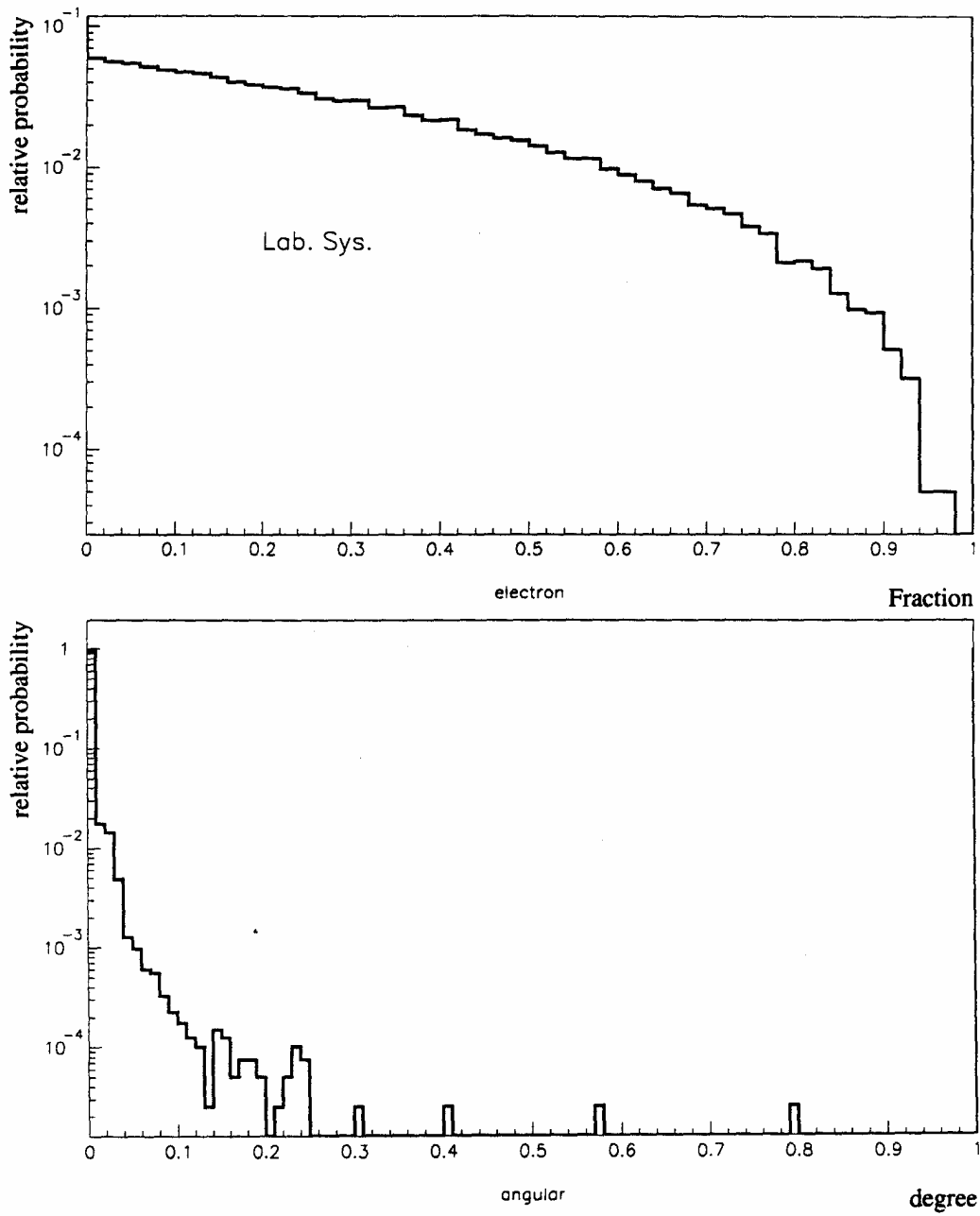


Figure 5.3. Secondary lepton energy and the angular distributions

5.2.3 The Landau-Pomeranchuk-Migdal (LPM) Effect

If the νN (neutrino-nucleon) interaction happens inside the earth, the LPM effect – the effect of multiple scattering on the *bremsstrahlung* and *pair production* cross sections or density effects of the medium in which the shower develops – should be considered for electromagnetic shower development[49, 50]. If the incident energy to initiate a shower, $E_o \gg E_{\text{lpm}} = 61.5L_{\text{cm}} \text{ TeV}$ [50]⁷, the LPM effect is significant. For instance, at up to 1.0 km below the surface of the earth the mass density is almost constant (Fig. 5.4), and it is $\sim 1.02 \text{ g/cm}^3$ with a radiation length, X_o , given as $\sim 26.8 \text{ g/cm}^2$. [52] Then, $E_{\text{lpm}} \sim 1.6 \times 10^3 \text{ TeV}$. Figure 5.5 shows the LPM effect on bremsstrahlung interaction and pair-production for different energy electrons and photons, respectively. In the figure, $F(x)$ is the probability per radiation length of radiating a photon with fractional energy between x and $x+dx$; and $G(x)$ is the probability per radiation length of pair-production with one electron with fractional energy between x and $x+dx$. Below the LPM threshold

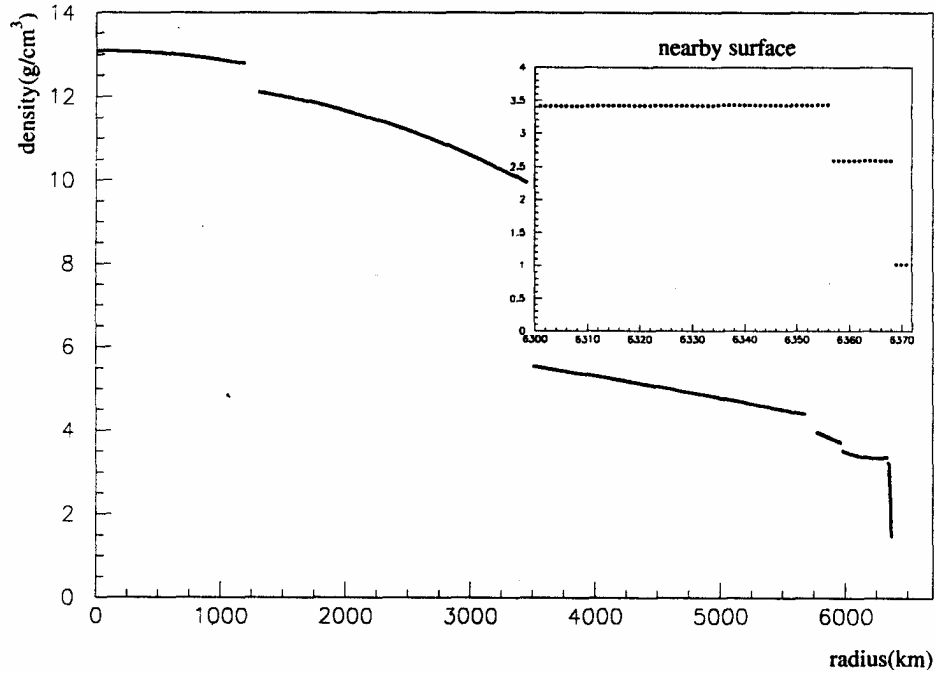


Figure 5.4. Earth mass density vs. radius

⁷ L_{cm} is the radiation length in centimeters

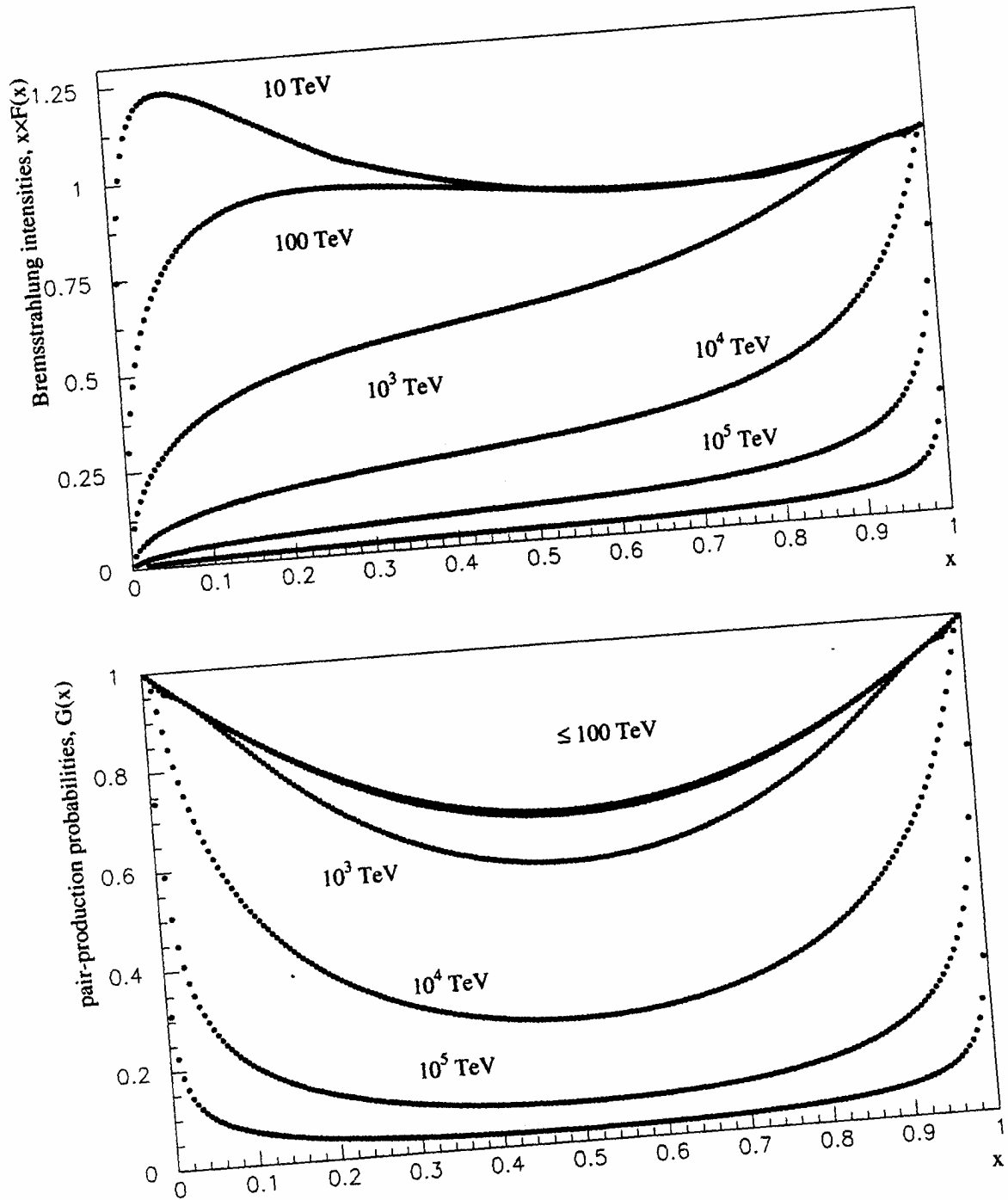


Figure 5.5. Differential bremsstrahlung intensities and differential pair-production probabilities per radiation length

energy the curve is very close to the limiting curve for Bethe-Heitler cross sections. For interactions in the atmosphere, L_{cm} near the ground is 3.053×10^4 cm ($\rho = 1.225 \times 10^{-3}$ g/cm³). On the other hand, L_{cm} about 20 km above sea level is 3.269×10^5 cm ($\rho = 1.144 \times 10^{-4}$ g/cm³).⁸ Hence, LPM threshold energies (E_{lpm}) near the ground and 20 km above sea level are 1.85×10^{18} eV and 2.0×10^{19} eV, respectively. Figure 5.4 shows the earth's mass density versus the distance from the center of earth[51]; up to 1 km below the earth surface the density, $\rho \sim 1.02$ g/cm³, and thus, $E_{lpm} \sim 1.6 \times 10^3$ TeV. The LPM effect inside the earth becomes significant from $\sim 1.0 \times 10^{+16}$ eV, and the LPM profile becomes saturated with increasing energy. In Figure 5.6, the small solid squares represent the GH profile (Approximation A) for a $1.0 \times 10^{+15}$ eV photon and the solid circles show the LPM effect for the photon-initiated cascades. The solid triangles and the empty squares represent the LPM effect for a $1.0 \times 10^{+16}$ eV and $1.0 \times 10^{+17}$ eV photon, respectively. Figure 5.7 shows the LPM effect on a shower inside the earth initiated by a single electron of energy 1.0×10^7 TeV; Figure 5.8 shows the LPM effects on upward shower development in the atmosphere, which are initiated by preshowers inside earth; and Figure 5.9 shows the LPM effects of 1.0×10^9 TeV electron in the atmosphere. In Figure 5.7 a 1.0×10^{19} eV electron initiates the shower, and the shower survives to a depth of ~ 420 meters inside earth ($\rho = 1.02$ g/cm³, $X_o = 26.8$ g/cm², $L_{cm} = 26.2$ cm). At each 200 radiation length (~ 52.4 m), an equivalent air GH electromagnetic longitudinal shower profile is shown. For example, if a νN interaction (CC) occurs at about 52.4 m below the earth's surface and the secondary lepton has an energy of 1.0×10^{19} eV, the resultant shower passes through 52.4 meters of earth ($\rho = 1.02$ g/cm³) and then comes out to the atmosphere to shower normally. The second peak in Figure 5.7 corresponds to this case. However, the LPM effect in the atmosphere should be taken into account instead of the GH profile, because 1.0×10^{19} eV is close to E_{lpm} in the air (2.0×10^{19} eV). The LPM effect is shown by profile 201 (the second highest peak) in Figure 5.8. In Figure 5.9, the showers initiated by 10^{21} eV electron in the atmosphere can survive up to ~ 190 km at sea level and ~ 1064 km at an altitude ~ 25 km above sea level.

⁸Radiation length is 37.4 g/cm².

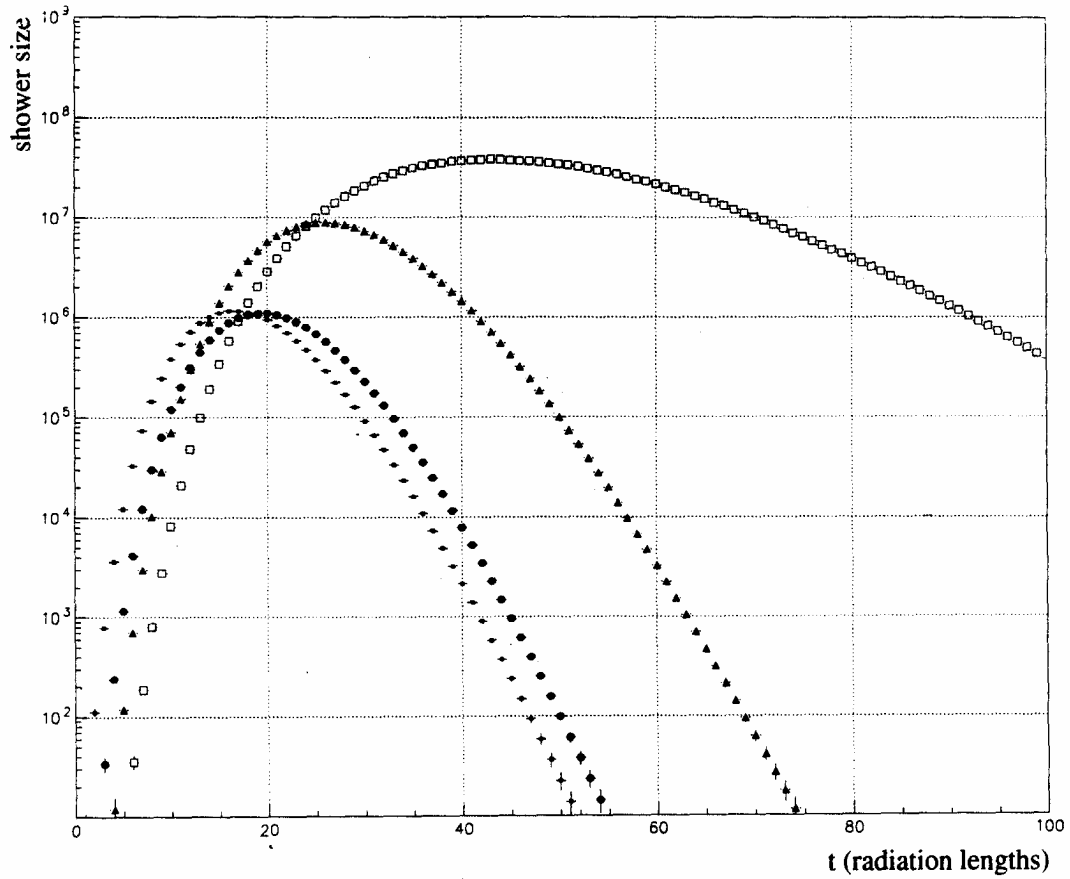


Figure 5.6. LPM effect on 10^{+15} , 10^{+16} , and 10^{+17} eV photon initiated cascades in the earth : small solid squares represent the GH profile initiated by a 10^3 TeV photon; solid circles, LPM effect for 10^3 TeV photon; solid triangles, LPM effect for 10^4 TeV photon; empty squares, LPM effect for 10^5 TeV photon.

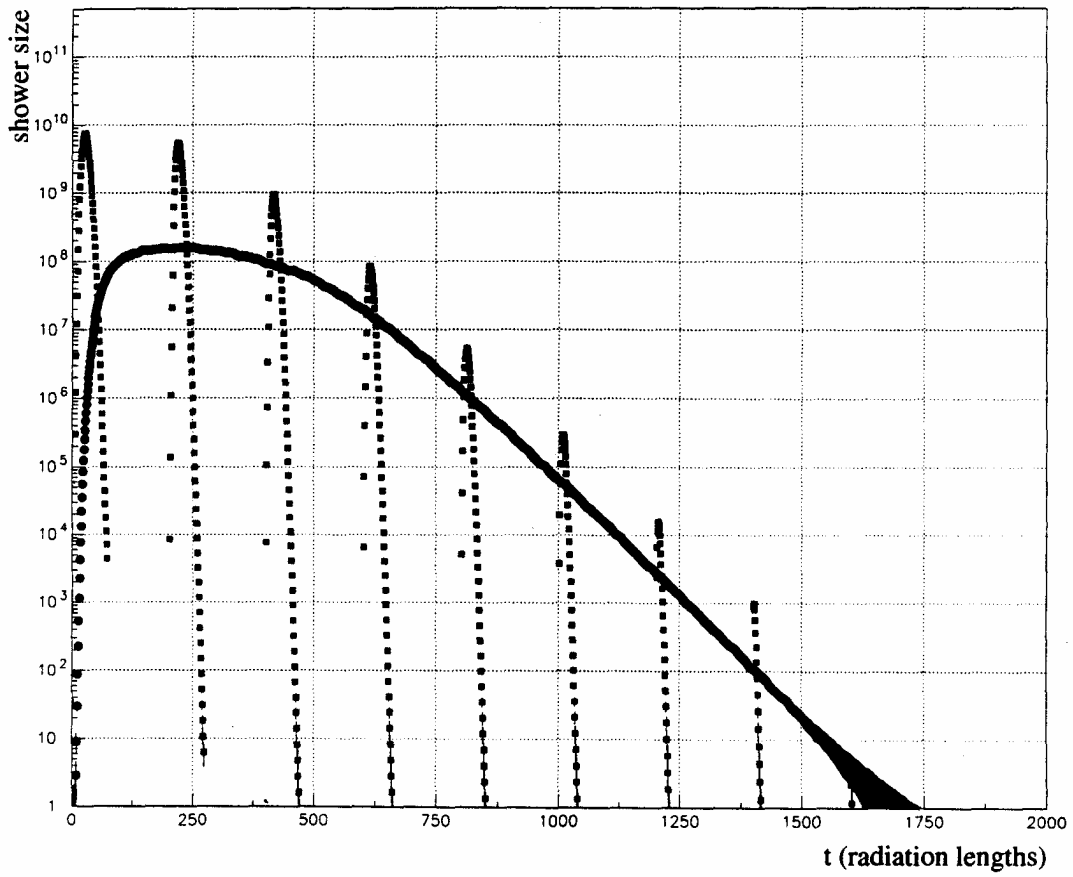


Figure 5.7. 1.0E+7 TeV electron initiated cascades in the earth, and the equivalent GH profile in the air for every 200 radiation length(X_0)

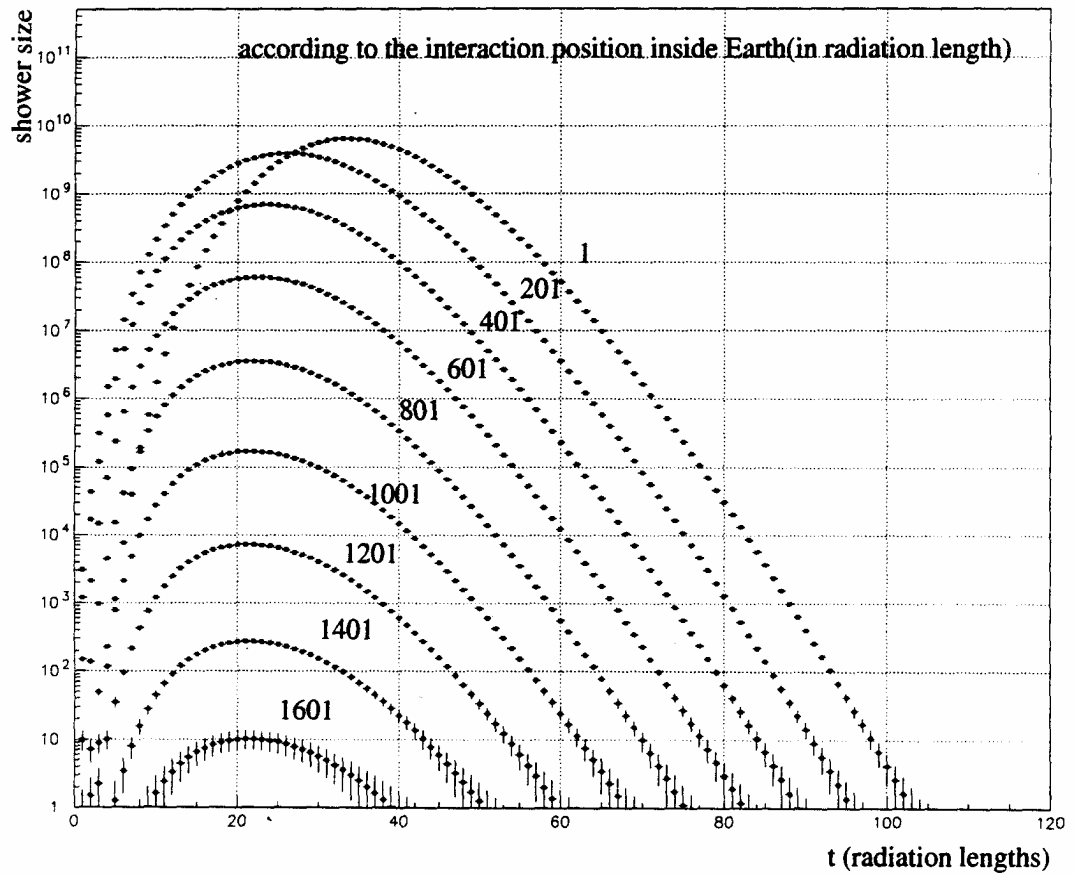


Figure 5.8. Shower profiles in the air initiated by preshowers by a $1.0E+7$ TeV electron inside the earth ; for instance, the 201 profile represents a $1.0E+7$ TeV electron initiating an EM showers at 201 X_0 below the earth surface, and finally emerging to the air

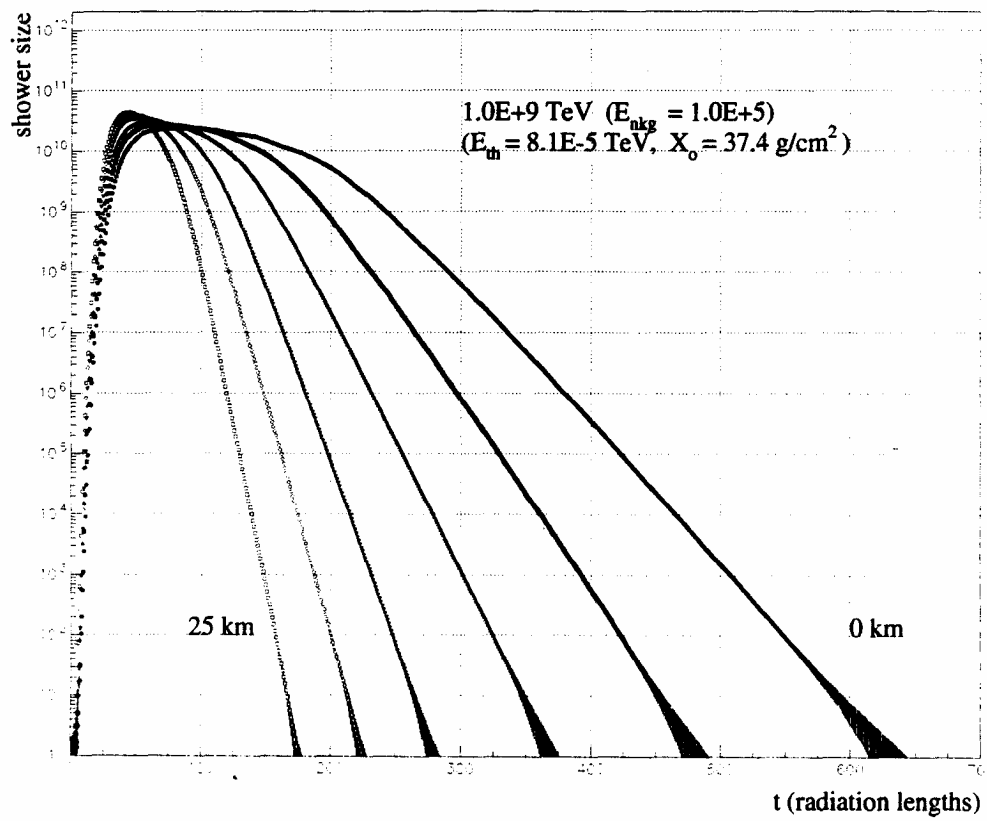


Figure 5.9. EM showers with LPM effect initiated by $1.0E+9$ TeV electron at altitudes, 25, 20, 15, 10, 5, 0 km (from left)

CHAPTER 6

DETECTOR MONTE CARLO

There are many physical processes to be considered which cannot be controlled by the experimental setup on the ground: from the first interaction of a cosmic-ray particle with atmospheric nuclei till the HiRes I detector detects the fluorescence light signal. As is the case for other cosmic-ray experiments, we use a detector Monte Carlo (MC) simulation as a way of modeling cosmic ray events, so that these events may be compared with experimental data. The detector MC simulation for the Fly's Eye/HiRes I detector has been well developed for events initiated by protons, iron, γ -rays, etc.[37] However, this MC is not appropriate for the simulation of cosmic neutrino events, especially the direction-generating-algorithm for incident cosmic rays; hence, it was modified and reinforced for cosmic neutrino events. Only the distinctive features of the MC pertaining to neutrino events are discussed here.

In the MC simulation for cosmic neutrino events, the neutrino threshold energy for the HiRes I detector and the first interaction depth (X_o) cannot be defined clearly because the EAS initiated from the interaction of (ν, N) or (ν, e^-) can be **anywhere** in the atmosphere or inside the earth. On the other hand, an EAS initiated by a proton or γ -ray with an energy less than the threshold energy ($E_{th} \sim 10^{+17}$ eV for the HiRes I detector) is much attenuated before the shower front reaches the detector, or the shower size is not big enough for the fluorescence light generated from the shower to trigger the detector. Hence, the first interaction depth (X_o) is not meaningful for neutrinos. That means, even PeV energy¹ order neutrino events can trigger the HiRes I detector.

In the MC simulation, the incident neutrinos should first be specified by their geometrical directions, identities and energies. To include all possible geometrical directions, an imaginary spherical shell (centered at the HiRes I detector) was used instead of a flat surface on the ground. Of course, the curvature of the earth is taken into account, since neutrino events (or deeply penetrating events in general) can be distinguished

¹For cosmic neutrinos.

from other cosmic ray events by horizontal geometry. Figure 6.1 shows the projection of the cosmic-ray impact points on the earth's surface. The upper right figure shows the projection if the earth is flat. The upper left figure and the lower figure show the projection if the curvature of the earth is taken into account.

6.1 Event Geometry

Figure 6.2 shows the spherical shell with radius R_p and four different geometrical cases: case 0 is for downward or upward neutrinos with no contact to the earth's surface in both directions from the impact point on the spherical shell; case 10, for downward neutrinos with a forward contact to the earth's surface and no backward contact from

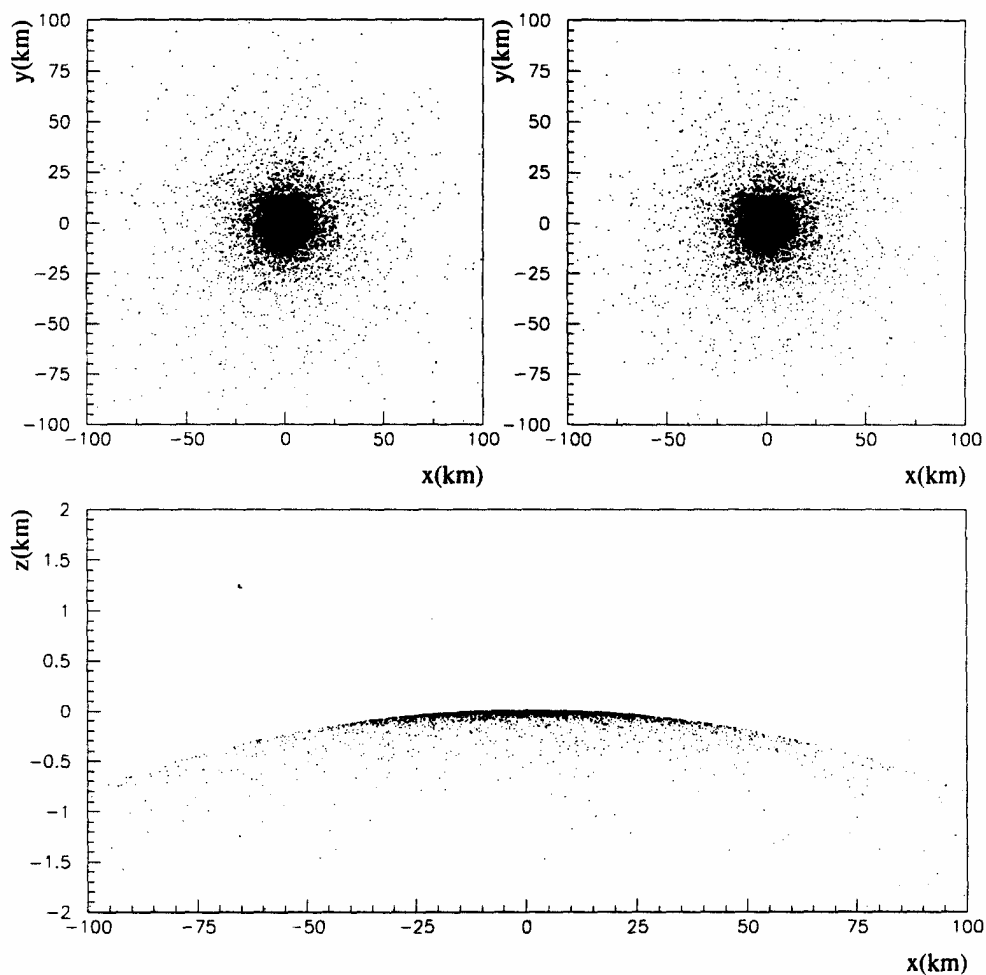


Figure 6.1. Cosmic-ray impact points projection on the earth's surface

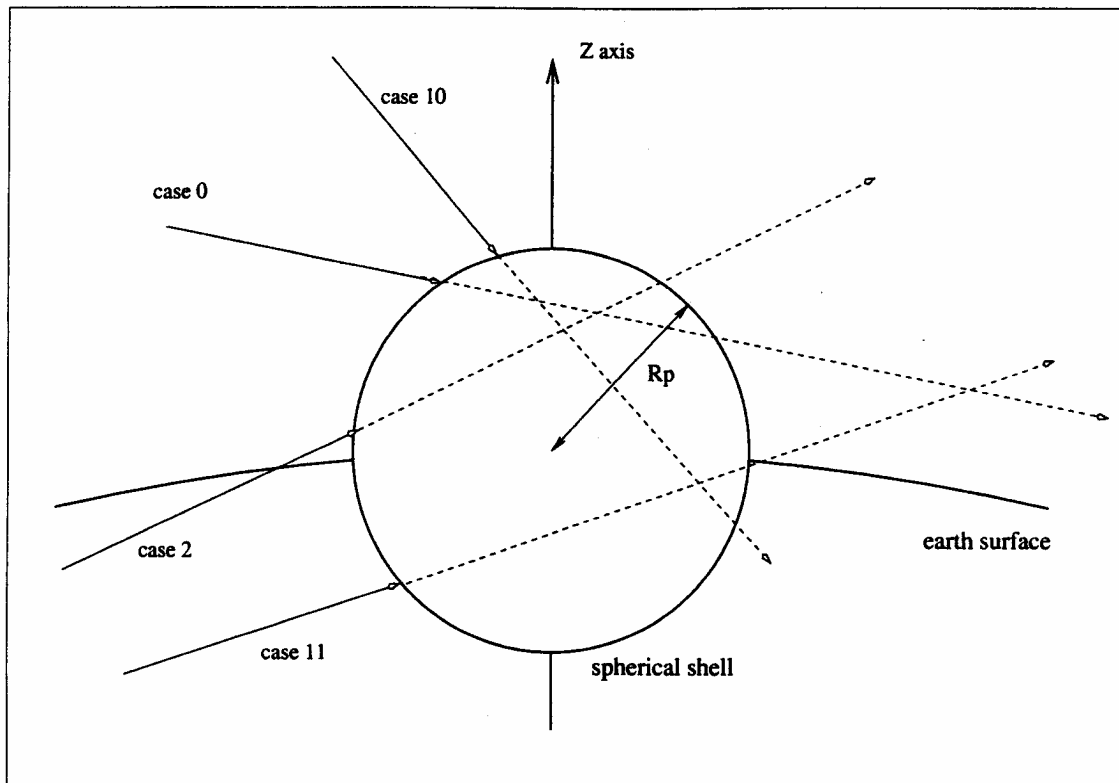


Figure 6.2. Neutrino event geometries and the cases

the impact point on the spherical shell; case 2, for upward neutrinos with two contacts to the earth's surface in the backward direction; case 11, for upward neutrinos with one forward contact and one backward contact with the earth's surface. For case 0 and case 10, all possible neutrino interactions to be considered for the HiRes I detector are in the atmosphere. However, for case 2 and case 11, neutrinos come through the earth from the other side; and if some of them survive till they reach just below the earth's surface (at maximum, ~ 980 m for 1.0×10^{21} eV), and if a shower is then initiated through the interaction, (ν, N) or (ν, e) , electromagnetic showers can go through the remaining part of the earth with the aid of the LPM effect and come out to the atmosphere. The radius of the spherical shell, R_p , has a similar meaning to the maximum R_p in the traditional HiRes MC, but it should be large enough to include all possible event geometries. Figure 6.3 shows the $1/R_p^2$ dependency of trigger rates versus R_p . This means that the R_p in the MC simulation for 1.0×10^{16} eV neutrinos should be larger than 5 km. Similarly, R_p for 1.0×10^{18} eV neutrinos should be larger than 14 km.

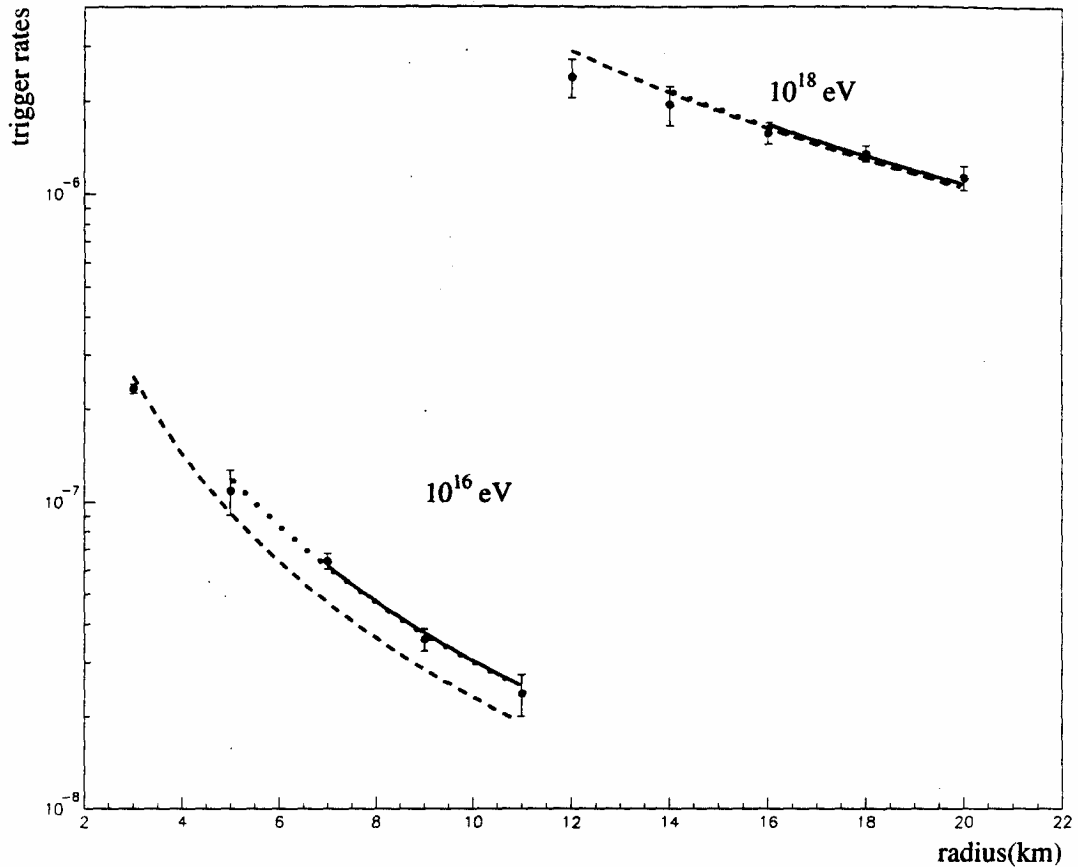


Figure 6.3. Detector trigger rates versus R_p in MC for neutrino events: The dashed lines indicate that the $1/R_p^2$ functional fit is not successful using all data points for neutrino energy between 10^{16} eV and 10^{18} eV. The solid lines indicates that the fitting is successful if some small R_p data points are removed.

6.2 Neutrino Events

Once the geometry of the incident neutrino is fixed in the MC simulation, a possible neutrino event is generated and allowed to interact and develop depending on the event geometry.

For cases 0 and 10, any possible neutrino interaction along the incident neutrino trajectory is in the atmosphere. Hence, the total probability of interaction with an atmospheric nucleon along the neutrino trajectory is calculated using the (νN) cross sections or the $(\nu_e e)$ cross section. The curved earth effect is taken into account in the atmospheric depth calculation along the neutrino trajectory. In the calculation, an isothermal atmosphere is assumed $\rho(h) = \rho_0 e^{-gMh/RT}$, where $\rho(h)$ is density of the

air as a function of the vertical altitude, $\rho_o = 1.225 \text{ kg/m}^3$ (air density at sea level), $M = 28.966$ (mean molecular weight), R is the gas constant, and $T = 288K$.

An interaction point in the atmosphere is chosen using the random number generator in the MC. The calculation of the total probability of interaction depends on the neutrino identity (electron neutrino $[\nu_e]$ or muon neutrino $[\nu_\mu]$)² and the type of interaction, such as CC or NC interaction.

For the cases 2 and 11, the survival probability of the incident neutrino is calculated from the top of the atmosphere, through the earth, and until the last $\sim 1 \text{ km}^3$ before the neutrino reaches the other side of the earth's surface. The survival probability and the interaction probability within the last $\sim 1 \text{ km}$ ($\rho_o \sim 1.0 \text{ g/cm}^3$) are combined to find the total probability, which is then the probability profile in the MC. Here, the possibility that neutrinos interact in the atmosphere after passing through the earth is ignored because it is so small. Figure 6.4 shows the total probability versus zenith angles, the probability is the average value for (νN) and $(\bar{\nu} N)$ interactions inside the earth, and the zenith angle indicates the angle from the vertical upward direction (Z-axis) on the earth surface along the neutrino trajectory. Since the 6.3 PeV $\bar{\nu}_e$ resonance affects the flux (of anti-electron neutrinos ($\bar{\nu}_e$) passing through the earth) at PeV energies ($\sim 5.7 \text{ PeV} < E_\nu < \sim 7.0 \text{ PeV}$), the interaction probability within the last $\sim 1 \text{ km}$ is abruptly reduced. To include this effect, an additional profile is made for $\bar{\nu}_e$ at around the resonance energy, $\sim 5.7 \text{ PeV} < E_\nu < \sim 7.0 \text{ PeV}$.

6.3 Extensive Air Shower (EAS)

The EAS initiated by a neutrino interaction in the atmosphere or inside the earth consists of a hadronic part and/or an electromagnetic part. The hadronic part is initiated by the secondary hadron(or hadrons) in (νN) interaction, and the electromagnetic part comes mainly from the secondary electron in $(\nu_e N)$ interaction or $(\nu_e e^-)$ interaction. To determine the ratio of the hadronic energy to the electromagnetic energy, the inelastic factor was calculated from Equation (5.5) and Equation (5.6). If the interaction occurs in the atmosphere for case 0 or case 10 in Figure 6.2, both parts contribute to the EAS; however, if the interaction occurs below the surface of the earth as for case 2 or case 11

² ν_e : 33.3% and ν_μ : 66.6%.

³An electromagnetic shower($E < 10^{20} \text{ eV}$) cannot survive after passing more than $\sim 1 \text{ km}$ inside the earth.

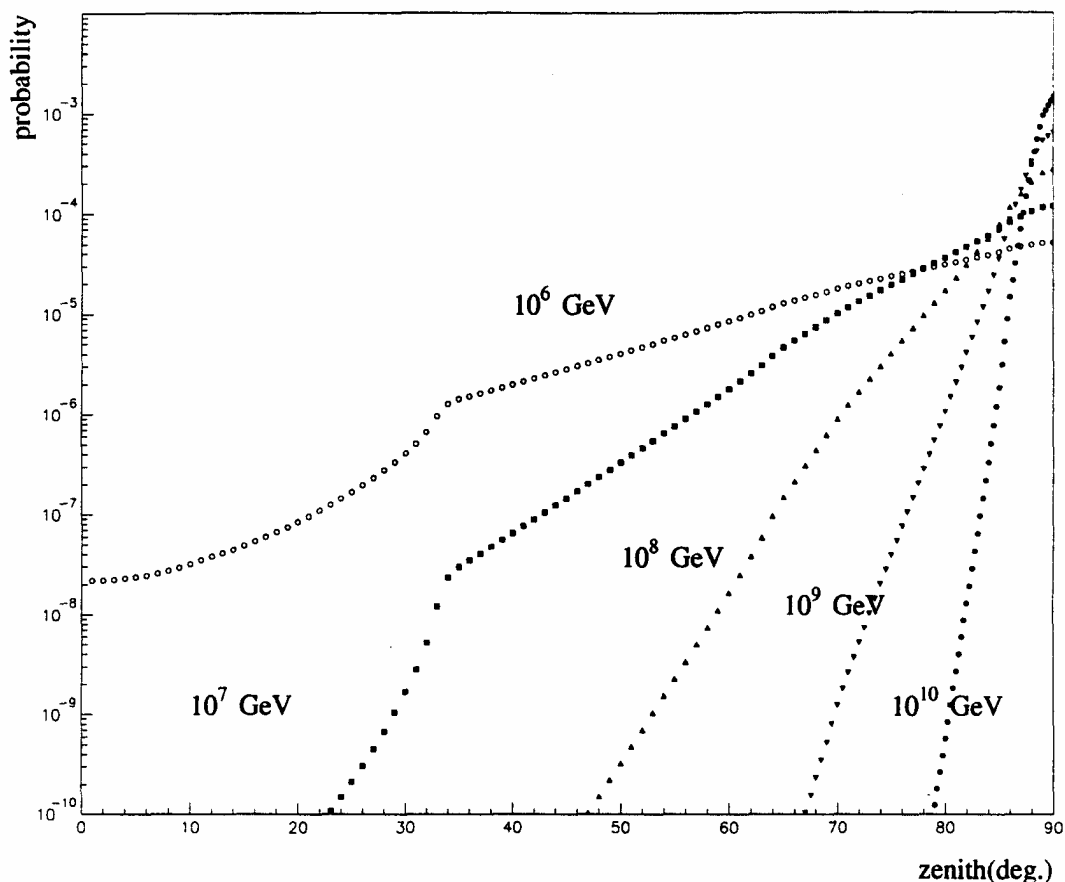


Figure 6.4. Neutrino interaction probability versus zenith angle within the depth of $1.0 \times 10^{+5}$ g/cm² (980 m) from the impact point on the earth surface in the neutrino trajectory. Empty circles are for an incident neutrino energy of $1.0 \times 10^{+15}$ eV; solid squares, $1.0 \times 10^{+16}$ eV; upward-going triangles, $1.0 \times 10^{+17}$ eV; downward-going triangles, $1.0 \times 10^{+18}$ eV; solid circles, $1.0 \times 10^{+19}$ eV.

in Figure 6.2, only the electromagnetic part can survive up to the earth's surface with the help of the LPM effect.

To estimate the shower size for the electromagnetic part, LPM profiles (for instance, Figures 5.8 and 5.9) are created for a pure electromagnetic shower in the air and inside the earth. There are two steps to get the shower size for events originating inside the earth. First, a preshower size on the earth's surface is evaluated using the LPM effect, in which the preshower is the residue surviving from the interaction point below the surface of the earth to the surface, and then the preshower is used to estimate the shower size in the air.

For the hadronic part, the longitudinal shower profile for an electromagnetic shower without the LPM effect [Eq. (2.5)] is used because we cannot be sure that the hadronic shower profile [Eq. (2.7)], which is parameterized for the hadronic interactions, is appropriate for the hadronic part initiated from a cosmic neutrino interaction and because we know that the electromagnetic shower without the LPM effect is very similar to the hadronic shower profile.

6.4 Detector Acceptance

One of the interesting things to do with the detector MC simulation is to estimate how many neutrino events (deeply penetrating events in general) the HiRes I detector can detect. First, the detector acceptance is calculated without any neutrino spectrum – this is the detector aperture. Then the expected number of events can be calculated from the aperture and any possible neutrino spectrum.

6.4.1 Detector Aperture(\mathcal{A})

Conventionally, the definition of the detector aperture (\mathcal{A}) is

$$\mathcal{A}(E) = S \times \Omega \times \mathcal{T}(E).$$

Here, the S is the imaginary spherical surface area on which neutrino flux impacts, and Ω is the solid angle covered by the flux on each surface segment, and $\mathcal{T}(E)$ is the detector triggering efficiency which can be obtained from MC simulation. Using the spherical shell criterion, $S = 4\pi R^2$ (R : radius of the spherical shell) and $\Omega = 2\pi$. Figure 6.5 shows the detector acceptance of the HiRes I detector with a 6-degree track length cut.⁴ Neutrino energies in each energy bin (MC simulation) were chosen without any weight (equally possible), and errors of the aperture (Y-axis) come from the statistical fluctuation in the MC simulation. The solid circles indicate all possible events; the empty squares, downward-going events; the empty circles, upward-going events. Taking account of the low energy region in Figure 6.6 the detector acceptance in Figure 6.5 for the upward-going events in $E < 10^{17}$ eV comes from the atmospheric pseudo-horizontally upward-going events, which is a unique signature for the deeply penetrating events. A sudden increase in the second energy bin can be explained by the 6.3 PeV ($\nu_e e$) resonance effect.

⁴The track length should be at least 6 degrees for the fitting processes in the data analysis to be successful.

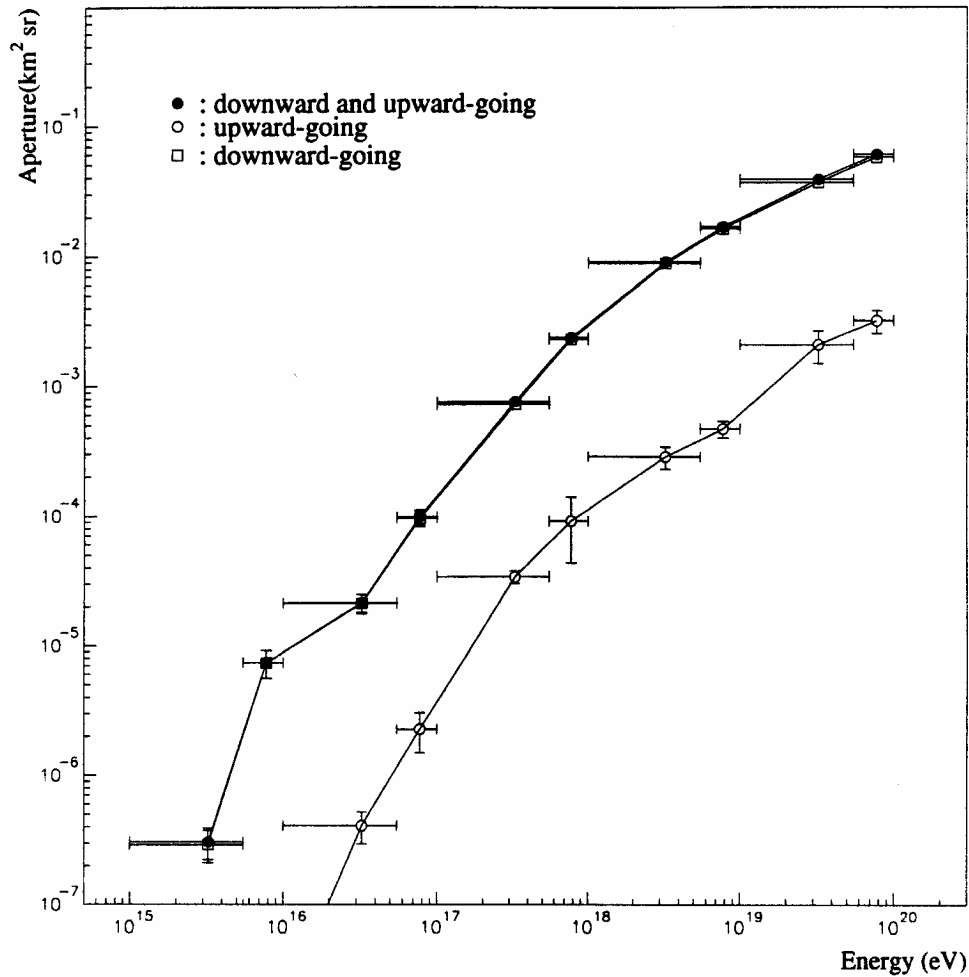


Figure 6.5. HiRes I detector acceptance for upward-going and downward-going neutrino events

In Figure 6.6, the detector acceptance from earth originated events (upward-going) is very small for the low-energy region, but it starts increasing when the neutrino energy is close to $E \sim 10^{+17}$ eV due to the LPM effect. After $E \sim 3.0 \times 10^{+17}$ eV, the increment of the acceptance slows down because of the saturation in the LPM effect as shown in Figure 5.6. For high energies, $E > 3.0 \times 10^{+19}$ eV, the increment slows down again. The reasons for this are that the high-energy neutrinos cannot survive inside the earth because of increased opacity of the earth for the high-energy neutrinos unless the geometries of the incident neutrinos are close to the horizon ($\theta \sim 90^\circ$) in the HiRes I detector coordinates. The probabilities for such specific geometries are small.

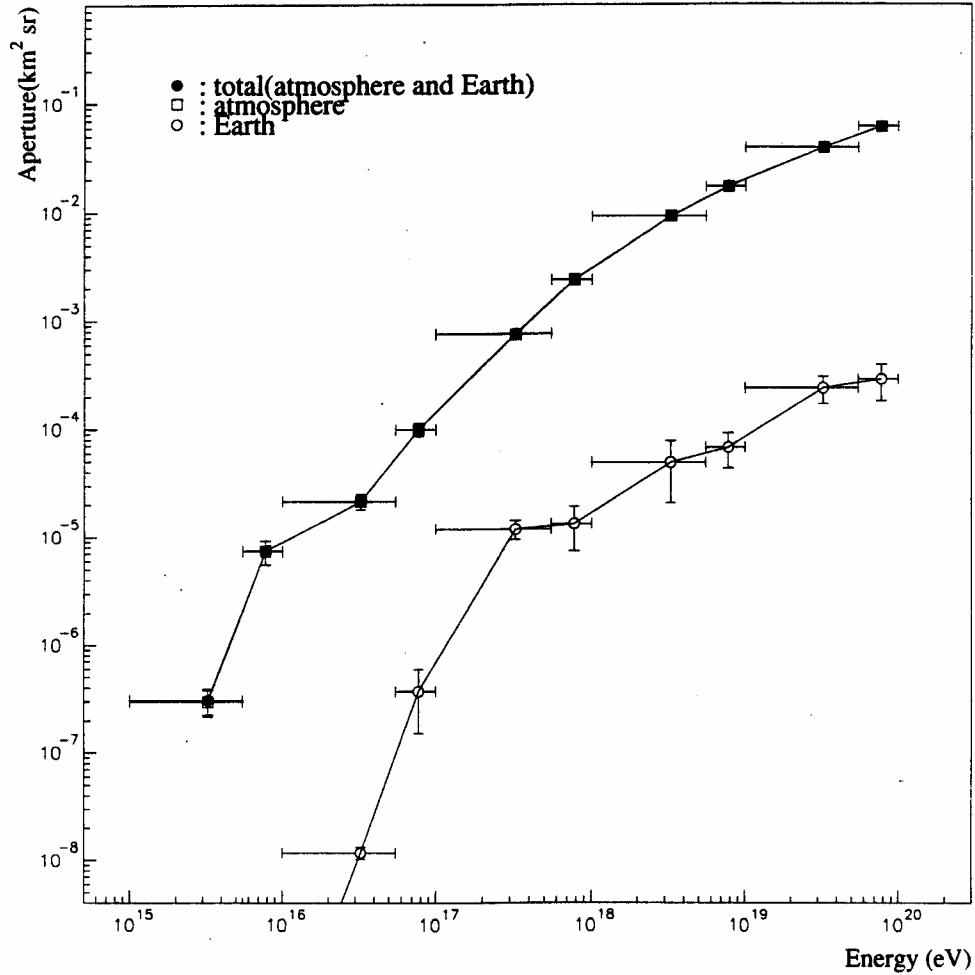


Figure 6.6. HiRes I detector acceptance for the atmospheric neutrino events and for the earth originated neutrino events.

Unfortunately, we cannot actually distinguish neutrino events from the other hadronic cosmic ray events as long as the event geometries are not oriented pseudo-horizontal or upward. To get the criterion for defining the pseudo-horizontal (or deeply penetrating) events required for neutrino identification, the dependence of atmospheric depth on zenith angle for hadronic cosmic ray showers must be investigated. More directly, the zenith angle distribution or the plane normal vector distribution (shower-detector plane vector) can be used from MC simulation or from the real data analysis for hadronic cosmic ray events. In 1992, a *deeply penetrating event search* was done with Fly's Eye data, and the plane normal vector was used to define the relevant criterion.[9] The criterion was found

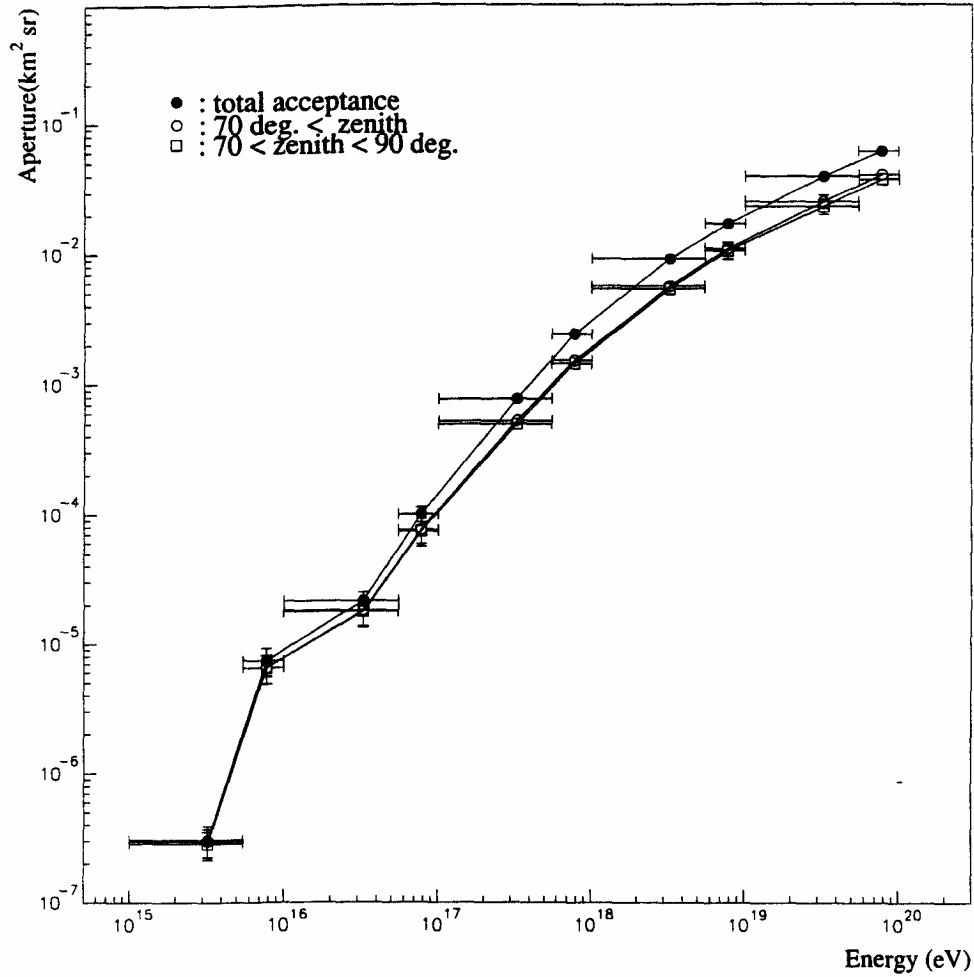


Figure 6.7. Aperture for pseudo-horizontal($\theta > 70^\circ$.) and upward-going events.

to be $\theta_n < \sim 20^\circ$; here the θ_n is the angle between Z-axis (vertically upward) and the plane normal vector. Here we define pseudo-horizontal events as having a zenith angle $\theta > 70^\circ$. More discussion of this criterion will be found in next chapter. For the pseudo-horizontal events, the detector acceptances for downward-going events and upward-going events are compared with the total detector acceptance in Figure 6.7. The acceptance for pseudo-horizontal events is more than $\sim 50\%$ of the total acceptance, and for all energy regions the downward-going events dominate over upward-going events. Figure 6.8 show the apertures for neutrino energies, $10^{15} - 10^{16}$ (eV), $10^{17} - 10^{18}$ (eV), and $10^{19} - 10^{20}$ (eV), depending on the zenith angle of the event geometry. For downward-going events ($\theta < 90^\circ$), the event probability in the HiRes I detector increases with the zenith angle,

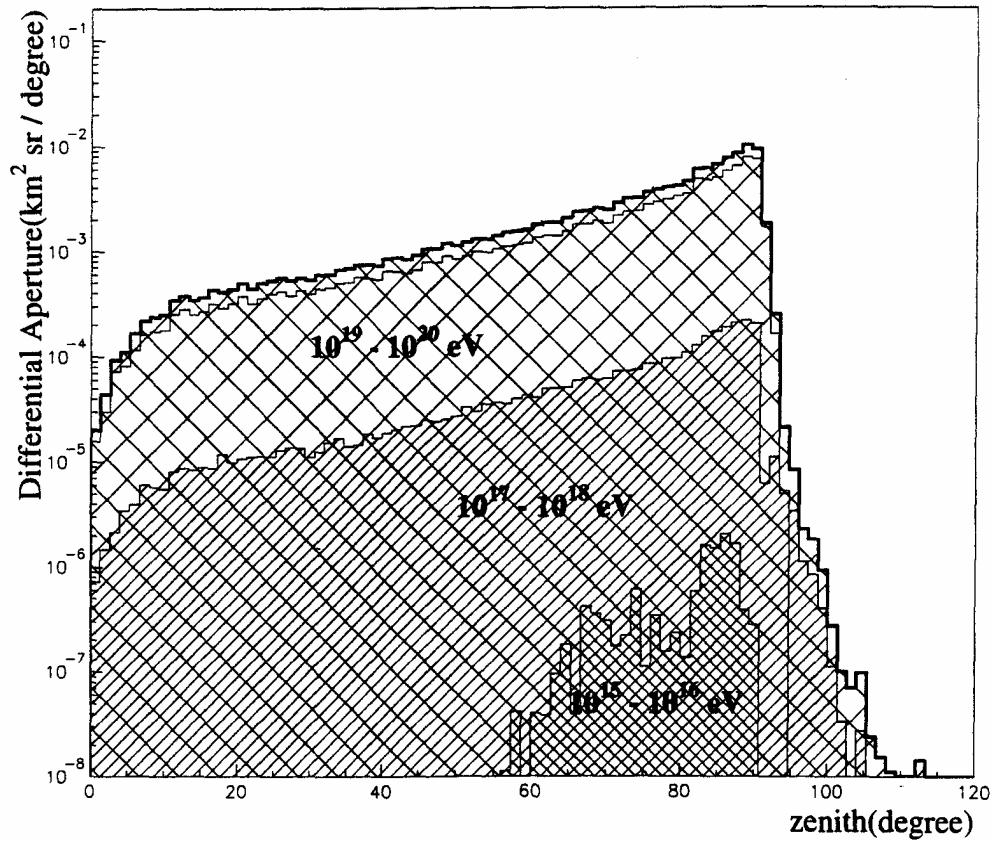


Figure 6.8. Aperture dependence on zenith angle for E_ν : $10^{15} - 10^{16}$ (eV), $10^{17} - 10^{18}$ (eV), and $10^{19} - 10^{20}$ (eV) ; the outermost thick boundary indicates the total sum for E_ν of $10^{15} - 10^{20}$ (eV).

since the atmospheric depth along the incident neutrino trajectory also increases; but for upward-going events ($\theta > 90^\circ$), the event probability decreases with the zenith angle, which reaches up to $\theta \sim 115^\circ$.

6.4.2 Neutrino Event Rate

With spectrum models such as AGN-M95, AGN-P96, AGN-SS91, and GRB-WB, the number of neutrino events in HiRes I detector can be estimated as

$$N(E_1, E_2) = \tau \int_{E_1}^{E_2} \mathcal{A}(E) \frac{d\mathcal{F}(E)}{dE} dE,$$

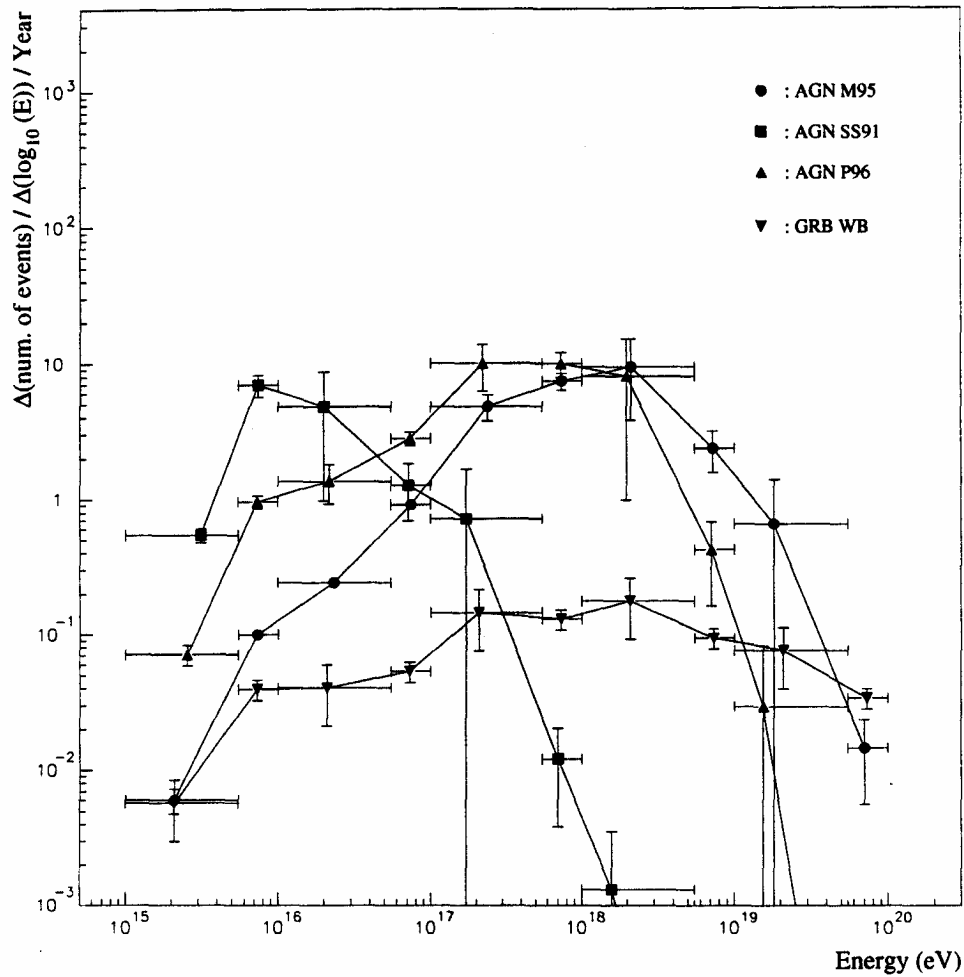


Figure 6.9. Neutrino events expectation in HiRes I detector for 1 year(detector on time)

where $N(E_1, E_2)$ is the expected number of events between energy E_1 to E_2 , τ is the detector on time, $\mathcal{A}(E)$ is the detector aperture, and $d\mathcal{F}(E)/dE$ comes from the cosmic neutrino spectrum. Figure 6.9 shows the neutrino events expectation in the HiRes I detector for 1 year of detector operation.

The various spectrum models are indicated by solid circles, AGN-M95; solid squares, AGN-SS91; upward triangles, AGN-P96; downward triangles, GRB-WB. The errors were evaluated with the uncertainties in the detector aperture [Fig. (6.5)] and the flux uncertainties in each energy bin in the neutrino spectrum models. Table 6.1 shows

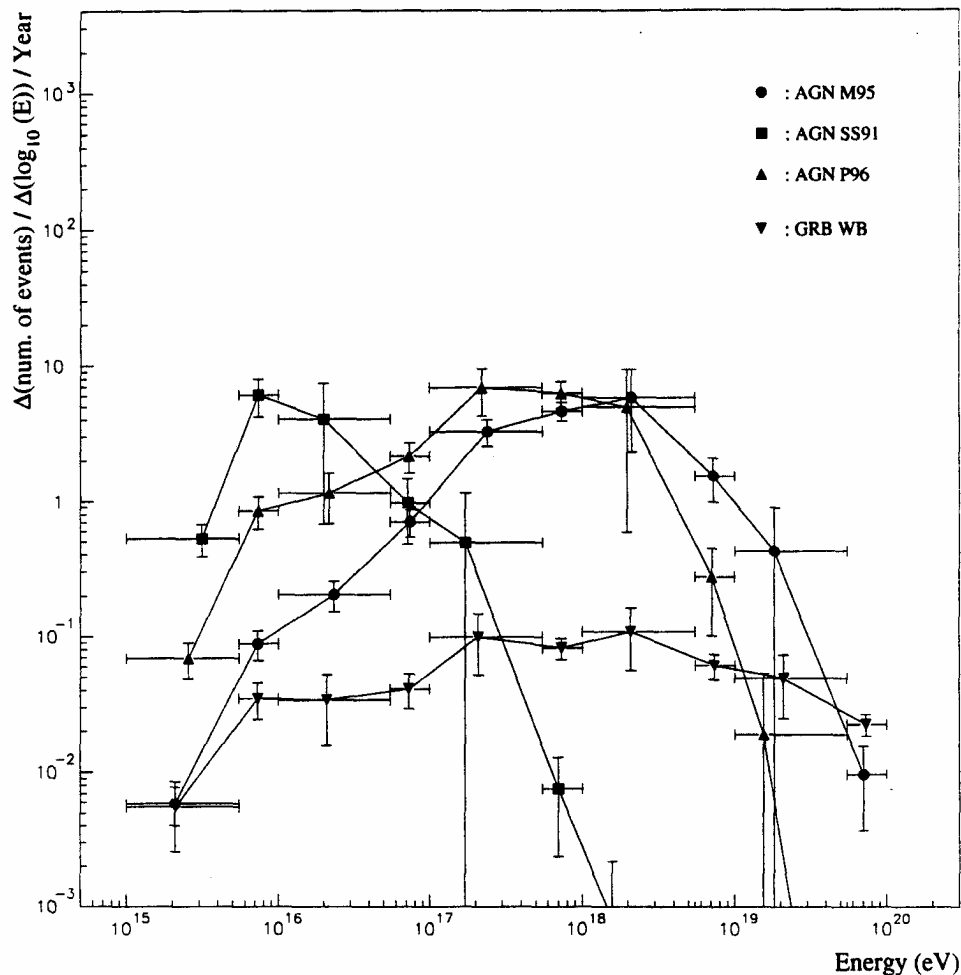


Figure 6.10. Pseudo-horizontal or upward-going events expectation ($\theta > 70^\circ$)

the number of events expected for 1 year of detector operation.⁵ Similarly, Figure 6.10 represent upward-going and pseudo-horizontal events expectation in HiRes I detector for 1 year of detector operation. Accumulated events numbers are summarized in Table 6.2. The total event number for each model correspond to ~ 1.4 events (AGN-M95), ~ 0.7 events (AGN-SS91), and ~ 1.8 events (AGN-P96) for every calendar year, respectively. Similarly, if the HiRes I detector is running with a $\sim 10\%$ duty cycle without any interruption, we should expect ~ 0.9 pseudo-horizontal or upward-going events from model AGN-M95; ~ 0.6 , from AGN-SS91; ~ 1.2 , from AGN-P96. The flux in spectrum

⁵This corresponds to 10 calendar years due to the $\sim 10\%$ duty cycle of the detector.

from GRB-WB is so small that the model spectrum cannot be tested practically with the HiRes I detector in a finite time period.

For atmospheric originating events, the number of neutrino events expected varies from model to model in Table 6.1; but for earth originated events, we cannot expect any events in a finite time period. In other words, the model spectrums, AGN-M95 and AGN-P96, lead to ~ 1 event for every 10 calendar years of detector time for earth-originated events.

Table 6.1. Number of events expected per year (detector on time).

model/energy(eV)	$> 10^{15}$	$> 10^{16}$	$> 10^{17}$	$> 10^{18}$	$> 10^{19}$
AGN-M95	14	14	14	8	-
AGN-SS91	7	4	1	-	-
AGN-P96	18	18	16	6	-
GRB-WB	-	-	-	-	-

Table 6.2. Number of events expected per year ($\theta > 70^\circ$).

model/energy(eV)	$> 10^{15}$	$> 10^{16}$	$> 10^{17}$	$> 10^{18}$	$> 10^{19}$
AGN-M95	9	9	9	5	-
AGN-SS91	6	4	-	-	-
AGN-P96	12	12	10	4	-
GRB-WB	-	-	-	-	-

CHAPTER 7

NEUTRINO EVENT SEARCH

A characteristic difference between neutrino events and hadronic cosmic ray events comes from the event geometry. Only neutrino events (or deeply penetrating events in general) can be detected in the Hires I detector in a horizontal or pseudo-horizontal geometry. In 1992, such a search for deeply penetrating events (including neutrino events) was done for the Fly's Eye Detector data[9], but no events were found.

7.1 Search Mechanism

The possibility of upward-going events from the earth and horizontal events¹ in the atmosphere is one of significant characteristics that can be used to distinguish cosmic neutrino events from hadronic cosmic ray events.

In general, the upward-going events originating below the surface of the earth can be ignored for energies less than $E \sim 10^{+17}$ eV; however, even for high energies, $E > 10^{+17}$ eV, the detector acceptance for the upward-going events is ~ 2 orders smaller than for the atmospheric events (see Figs. 6.5 - 6.8). Figure 7.1 shows the detector acceptances for horizontal events, atmospheric events, and the earth-originated events. The horizontal acceptance is not small but is $\sim 10\%$ out of the total detector acceptance. A unique and simple way to distinguish deeply penetrating events from hadronic events is to search for horizontal events and/or pseudo-horizontal² upward-going or downward-going events. In the pseudo-horizontal geometry, however, many artificial events – Xenon flasher and YAG laser events – are mixed with cosmic ray events in the HiRes I data, and they must be selected out.

¹Slightly upward-going or downward-going from the horizon – case 0 in Figure 6.2.

²Conventionally defined as those events for which the zenith angles in the event geometries are $70^\circ < \Theta < 110^\circ$.

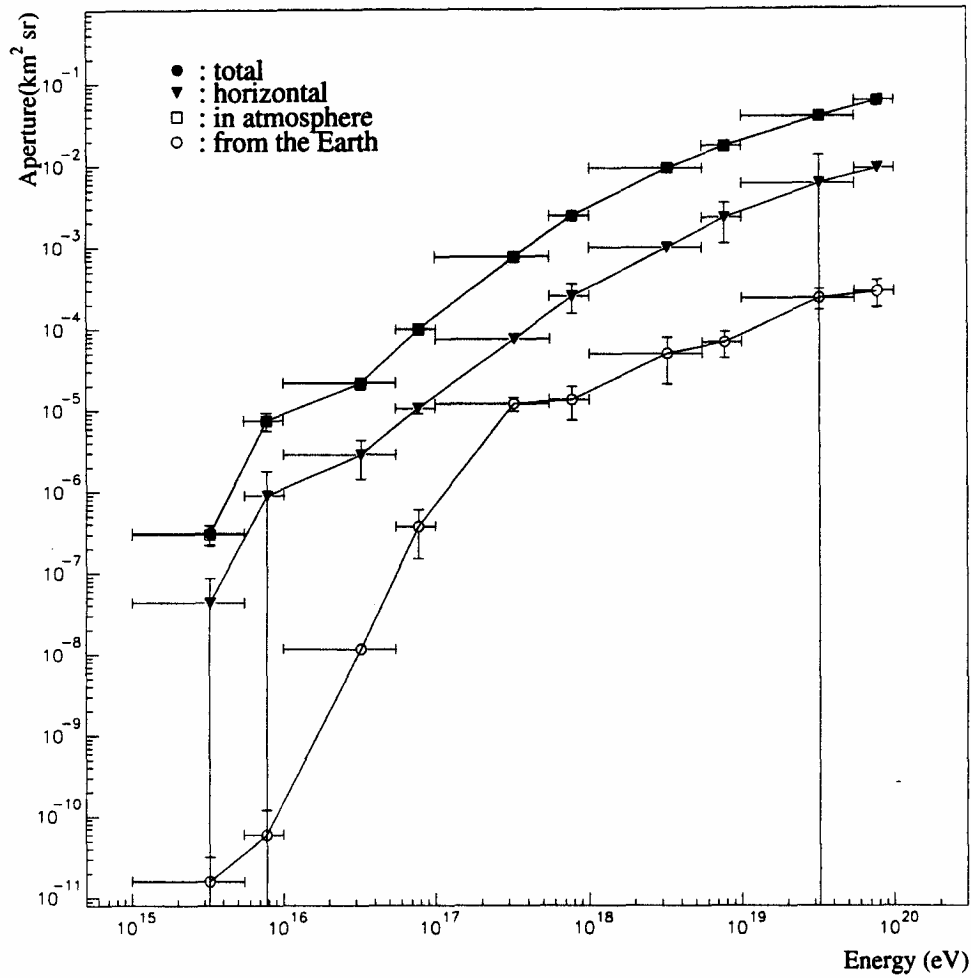


Figure 7.1. HiRes I detector acceptance : solid circles indicate total detector acceptance; downward-going triangles, for horizontal events; empty squares, for atmospheric events; empty circles, for earth-originated events.

7.1.1 Criterion for Neutrino Events

The criterion for selecting neutrino events is related to the event geometry itself, because the HiRes I detector measures the shower size and X_{max} of EAS generated by cosmic rays. Since the first interaction of hadronic events occurs near the top of the troposphere, the EAS from hadronic events with a horizontal geometry cannot penetrate deep into the atmosphere. The scintillation light from distant high events is attenuated and disappears before it reaches the detector. The selection criterion should thus be related to the zenith angle, Θ_c , in the event geometry. Using the MC[37] simulation

for hadronic events initiated by *proton* primaries the HiRes I detector apertures with several zenith angle (θ) cuts were estimated. Figure 7.2 shows the detector aperture with a 6-degree track length cut and partial apertures with 70, 80, 82, and 84 degree zenith angle cuts. In the data analysis, the zenith angle of the shower track can be found via the geometrical reconstruction – a plane fit to find the SD (shower detector) plane normal vector and a timing fit to find the geometry of the shower track – with an uncertainty from both fitting processes; however, the SD plane normal vector can be found with a relatively better resolution using the plane fit only. The plane normal vector

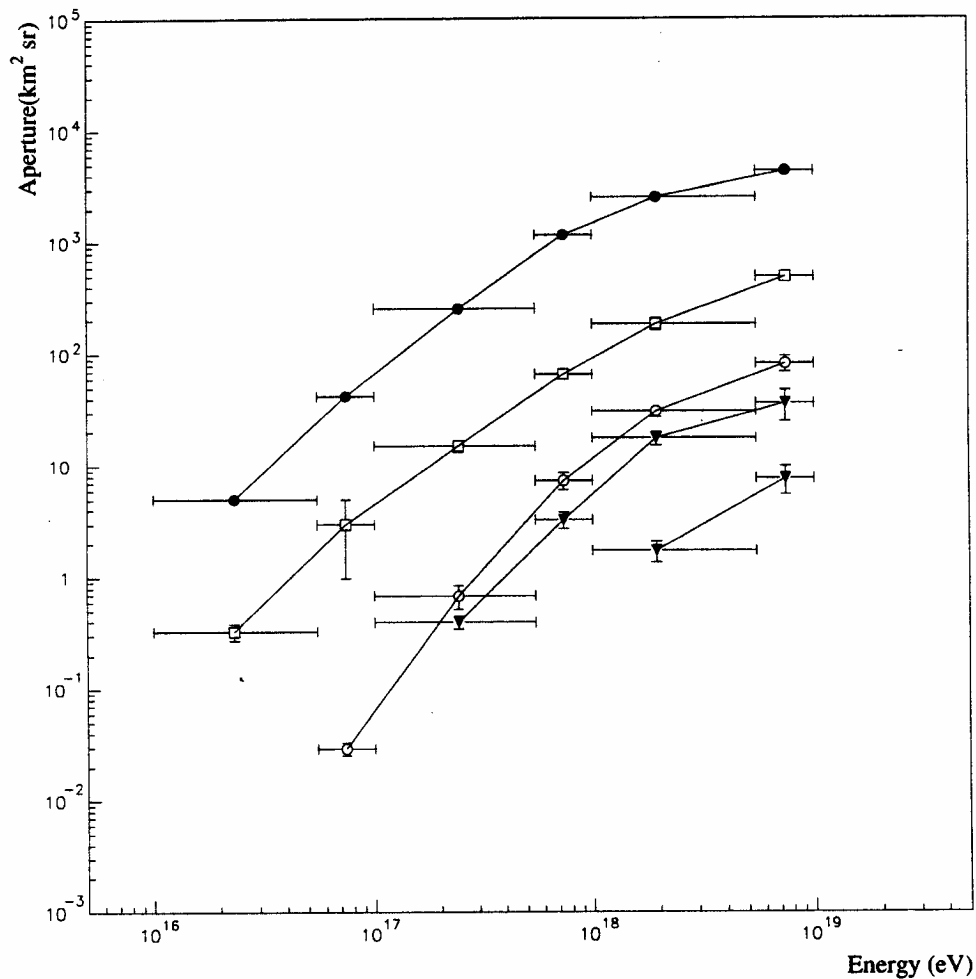


Figure 7.2. HiRes I detector Aperture for Hadronic events with a 6-degree track cut : Solid circles represent the aperture for all zenith angles; empty boxes, for zenith angles, $\theta > 70^\circ$; empty circles, for zenith angles, $\theta > 80^\circ$; downward triangles, for zenith angles, $\theta > 82^\circ$; upward triangles, for zenith angles, $\theta > 84^\circ$.

zenith angle is a more robust variable than the zenith angle, especially in searching for pseudo-horizontal events. Figure 7.3 shows the plane normal angle (Θ_n) distributions of the detector aperture for hadronic events and neutrino events. For the hadronic case, horizontal or pseudo-horizontal (up to ~ 10 degrees.) events are not expected. On the other hand, for neutrinos, the horizontal or the pseudo-horizontal events are more possible than other angles. With several SD plane normal angle cuts the hadronic event rates in the HiRes I detector was estimated using the differential cosmic ray spectrum shown in Figure 7.4. The event rates(R) are shown in Figure 7.5, and the accumulated events

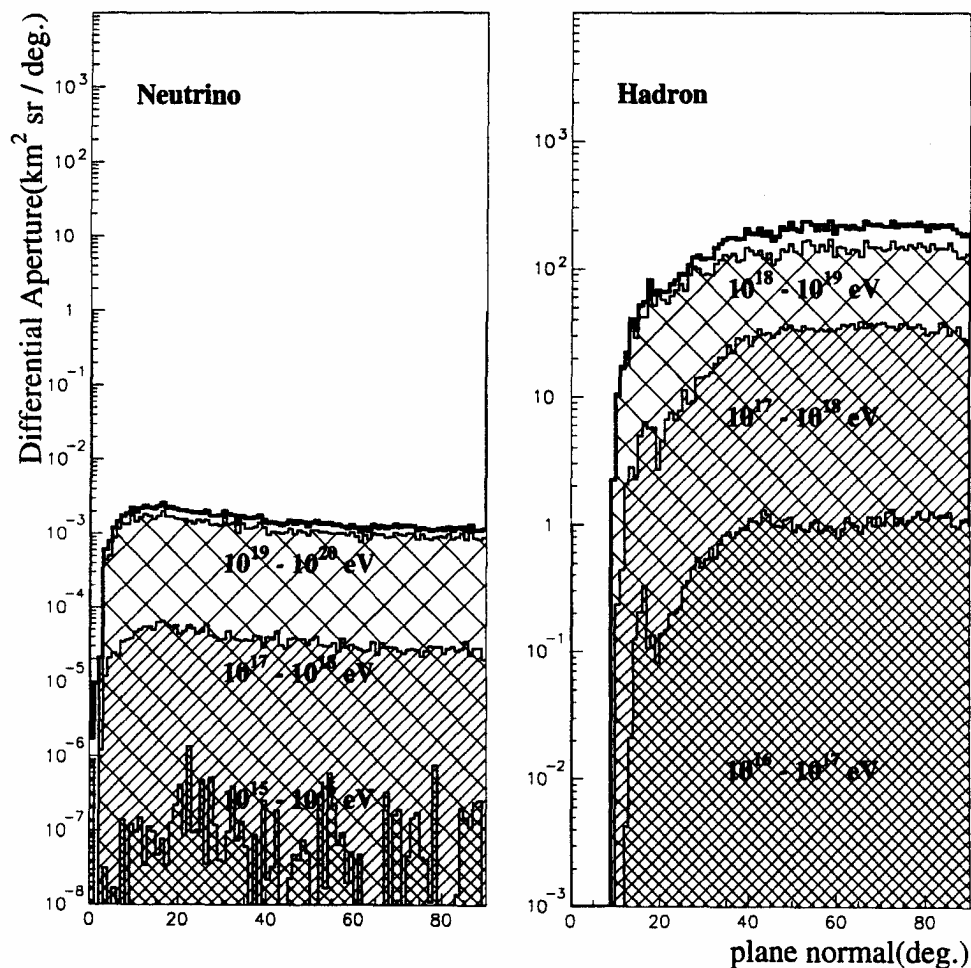


Figure 7.3. Plane normal angle distributions for the HiRes I detector aperture for the primary cosmic rays, neutrino and proton, with a 6-degree track length cut: The out most thick lines indicate total sums; $1.0 \times 10^{15} - 1.0 \times 10^{20}$ eV for Neutrino and $1.0 \times 10^{16} - 1.0 \times 10^{19}$ eV for Proton

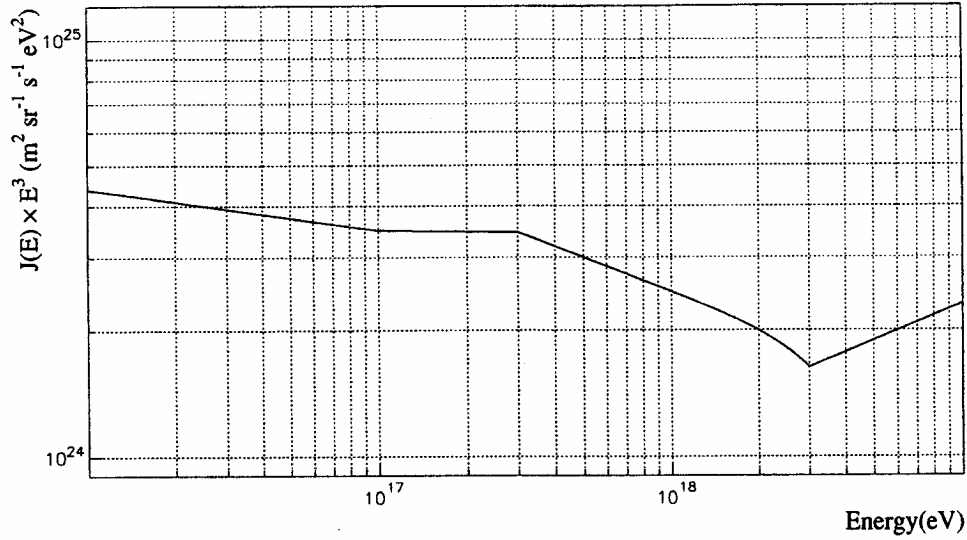


Figure 7.4. Differential cosmic ray spectrum(1.0×10^{16} eV $< E < 1.0 \times 10^{19}$ eV) : Ref. Fig. 2.1

rates for 1 year (detector on time) are summarized in Table 7.1. In the Fly's Eye detector thesis written in 1992[9], the criterion for deeply penetrating events was $\Theta_n < 18^\circ$ (plane normal angle). Since the HiRes I detector is using $1^\circ \times 1^\circ$ field of view PMTs which have much better angular resolution than in the Fly's Eye and the arrangement of mirrors in HiRes I detector is different from the Fly's Eye, the criterion for the deeply penetrating events in the HiRes I detector can be different from the one used for the Fly's Eye detector.

Table 7.1 shows that an event rate of $\sim 33 \pm 25$ for $E > 1.0 \times 10^{17}$ eV for every calendar year for hadronic events with plane normal angles, $\Theta_n < 12^\circ$ can be expected. However, the event rate for $\Theta_n < 10^\circ$ is ~ 1 event for $E > 1.0 \times 10^{18}$ eV. On the other hand, neutrino event rates from the various cosmic neutrino spectrums are summarized for 10, 12, and 15 degree angular cuts in Table 7.2, Table 7.3, and Table 7.4, respectively. Except for the model spectrum AGN-SS91 the event rates are maximized at around $\sim 10^{+17} - \sim 10^{+18}$ eV. For instance, Figure 7.6 shows the event rates versus neutrino energy with the 12-degree angular cut.

7.2 Geometrical Reconstruction

The first stage of data analysis is to reconstruct the shower geometry. Using the pointing directions of the triggered PMTs, the SD plane is determined. This is a *plane*

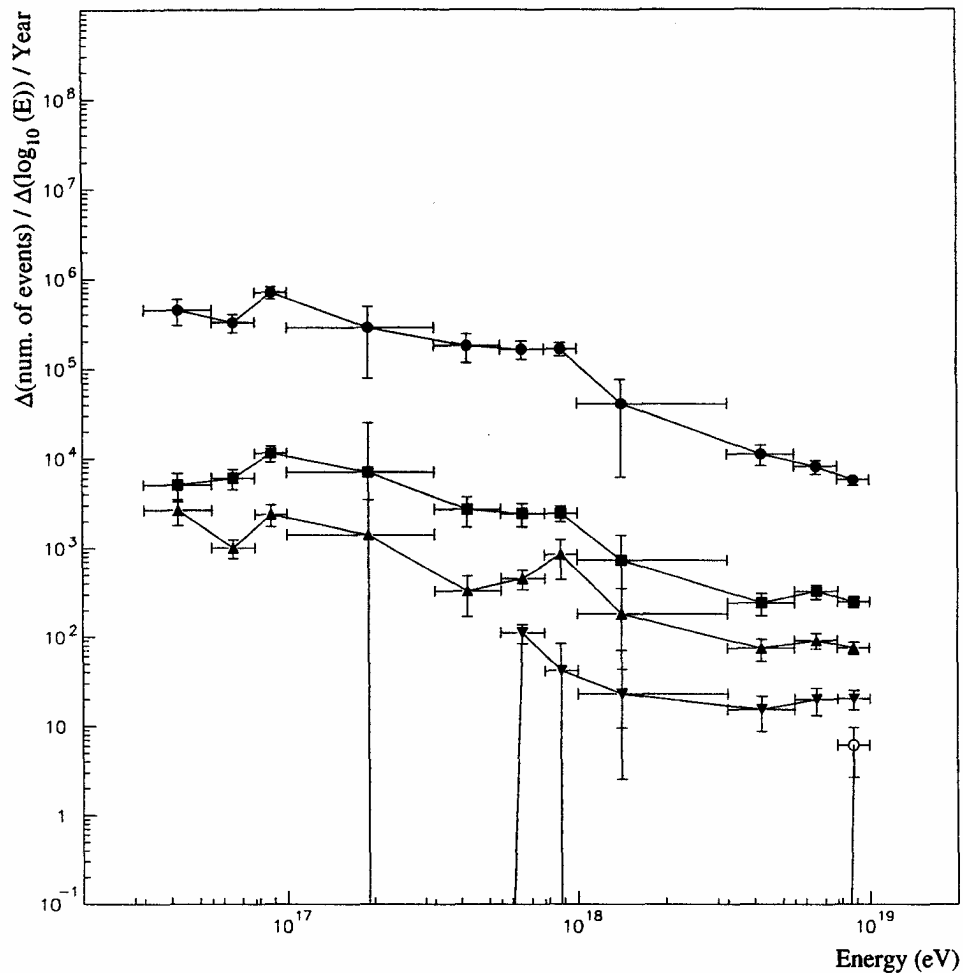


Figure 7.5. Hadronic event rates in the HiRes I detector depending on the SD plane normal angle cut: solid circles represent all angles; solid boxes, for a 20-degree cut; upward triangles, for a 15-degree cut; downward triangles, for a 12-degree cut; and empty circle, for a 10-degree cut. The uncertainties are from the statistics in the MC and the spectrum.

fit using tube pointing information. The shower geometry is reconstructed using the SD plane and the trigger time information for each PMT. This is a *timing fit* using dynamical information.

Before the fitting process starts, background noise triggered PMTs are filtered out. A PMT that does not have at least two adjacent neighbors (or else one adjacent neighbor which has another additional adjacent neighbor) is assumed to be a noise triggered PMT.

Table 7.1. Hadronic events rates for 1 year(detector on time) in HiRes I detector(6-degree track length cut)

SD (deg.)/eV	$E > 3 \times 10^{16}$	$E > 10^{17}$	$E > 10^{18}$
$\Theta_n < 90$	$3.05 \times 10^6 \pm 3.96 \times 10^5$	$7.21 \times 10^5 \pm 1.00 \times 10^5$	$8.89 \times 10^4 \pm 5.04 \times 10^4$
$\Theta_n < 20$	$5.18 \times 10^4 \pm 2.67 \times 10^4$	$1.15 \times 10^4 \pm 1.81 \times 10^3$	$2.11^3 \pm 9.78 \times 10^2$
$\Theta_n < 15$	$1.21 \times 10^4 \pm 6.78 \times 10^2$	$2.75 \times 10^3 \pm 6.78 \times 10^2$	$5.69 \times 10^2 \pm 2.52^2$
$\Theta_n < 12$	$3.28 \times 10^2 \pm 7.99 \times 10^1$	$3.28 \times 10^2 \pm 7.99 \times 10^1$	$1.05 \times 10^2 \pm 3.24 \times 10^1$
$\Theta_n < 10$	8.97 ± 5.12	8.97 ± 5.12	8.97 ± 5.12

Table 7.2. Neutrino events with the 10-degree SD plane normal angle cut for 1 year (detector on time)

model/energy(eV)	$> 10^{15}$	$> 10^{16}$	$> 10^{17}$	$> 10^{18}$	$> 10^{19}$
AGN-M95	1.3	1.3	1.2	0.7	-
AGN-SS91	0.7	0.6	-	-	-
AGN-P96	1.9	1.8	1.6	0.5	-
GRB-WB	-	-	-	-	-

Table 7.3. Neutrino events with the 12-degree SD plane normal angle cut for 1 year (detector on time)

model/energy(eV)	$> 10^{15}$	$> 10^{16}$	$> 10^{17}$	$> 10^{18}$	$> 10^{19}$
AGN-M95	1.8	1.8	1.7	1.0	-
AGN-SS91	1.0	0.9	-	-	-
AGN-P96	2.6	2.5	2.2	0.7	-
GRB-WB	-	-	-	-	-

7.2.1 Plane Fit

A χ^2 minimization method was used to get the plane normal vector of the SD plane, where the χ^2 is defined as

$$\chi^2 = \sum_{i=1}^{i=N} \left(\frac{\vec{V}_n \cdot \vec{V}_i}{\sigma_i} \right)^2,$$

N is the number of non-noise triggered PMTs; \vec{V}_n is the SD plane normal unit vector; and \vec{V}_i , the pointing unit vector for each PMT in an event. We estimate the uncertainty

Table 7.4. Neutrino events with the 15-degree SD plane normal angle cut for 1 year(detector on time)

model/energy(eV)	$> 10^{15}$	$> 10^{16}$	$> 10^{17}$	$> 10^{18}$	$> 10^{19}$
AGN-M95	2.7	2.7	2.6	1.4	–
AGN-SS91	1.5	1.3	–	–	–
AGN-P96	3.8	3.7	3.2	1.0	–
GRB-WB	–	–	–	–	–

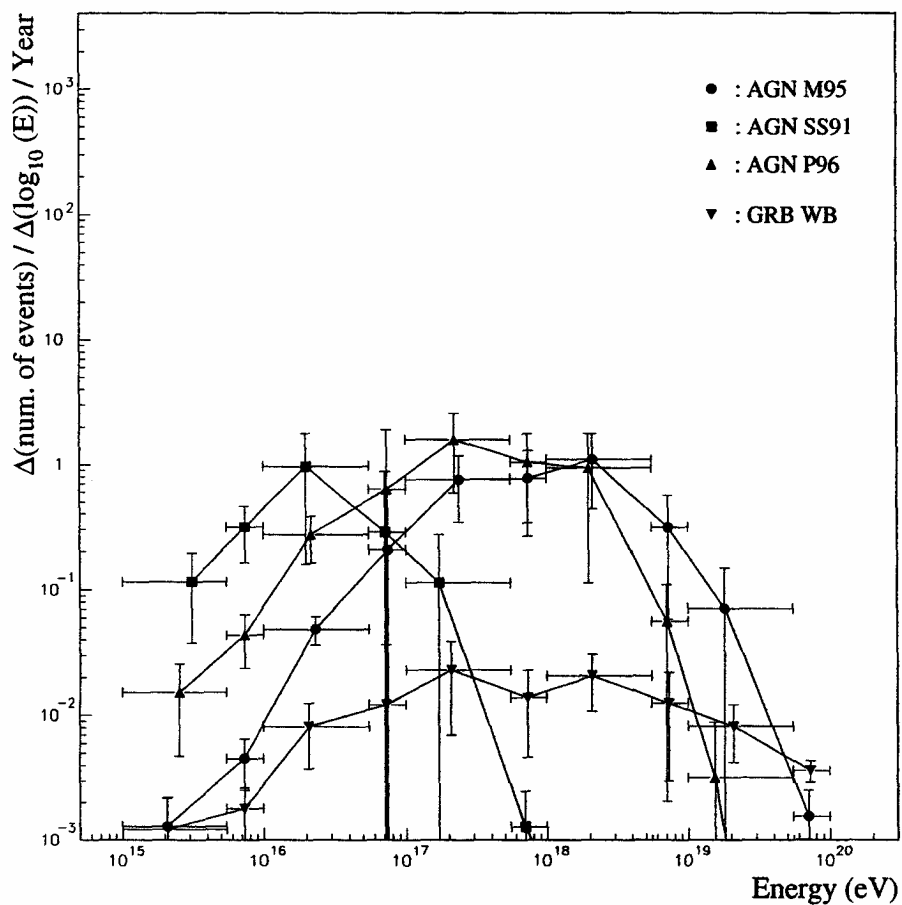


Figure 7.6. Event rates vs. neutrino energy with 12-degree plane normal angle cut: solid circles indicate AGN-M95; solid boxes, AGN-SS91; upward-going triangles, AGN-P96; downward-going triangles, GRB-WB.

of the PMT pointing vector to be $\delta_\theta = 1.745 \times 10^{-2}$ rad (1.0 degree) and $d\Omega = 2.3924 \times 10^{-4}$ st. The direction of \vec{V}_n is varied for all possible directions and the χ^2 values are compared to find the minimum value of χ^2 and the corresponding \vec{V}_n . If the minimum χ^2 value is bigger than 2.0, the event is treated as a noise event, because almost all the χ^2 values for the neutrino events in the MC simulation are smaller than 2.0. For instance, Figure 7.7 shows the resolution of the SD plane fit for pseudo-horizontal neutrino events and the correlations of χ^2 and the number of PMTs in each event. The average deviation in the Figure 7.7 is 1.4 ± 1.5 degree.

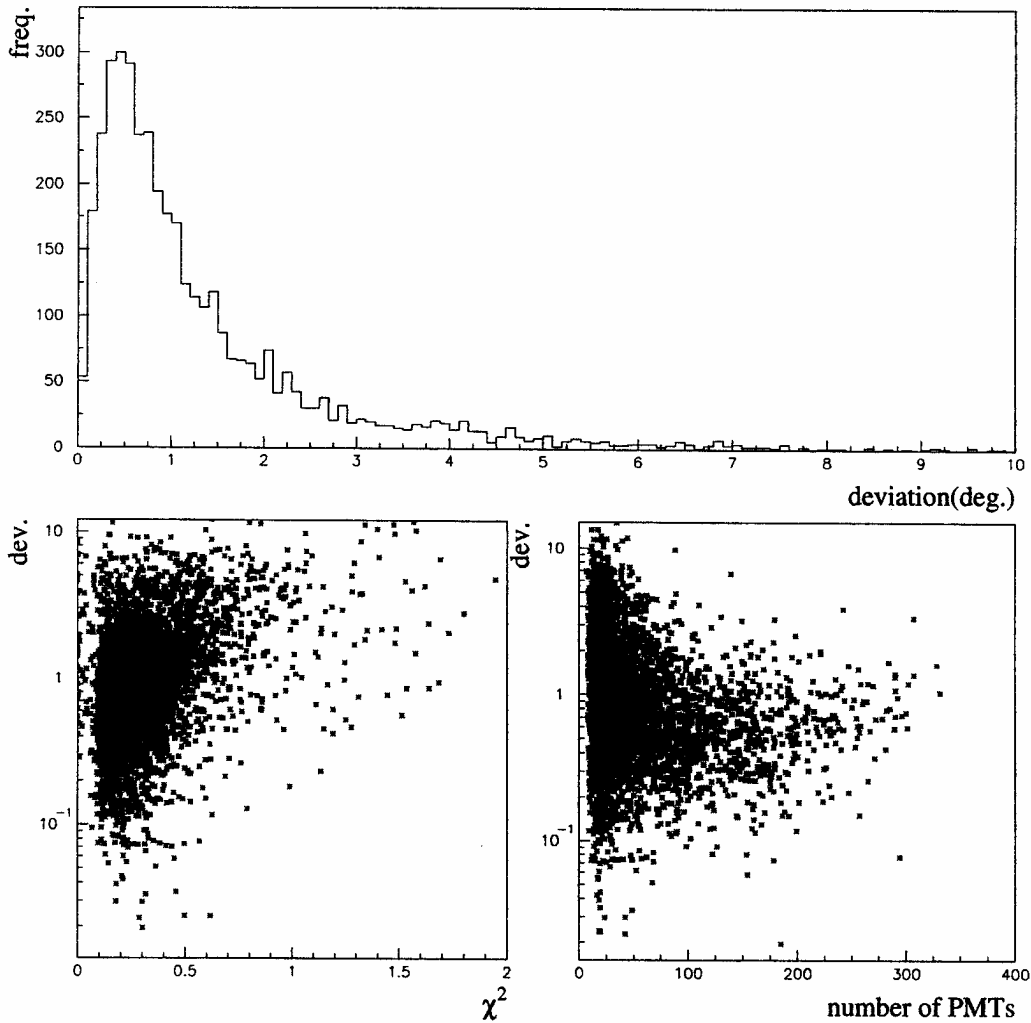


Figure 7.7. Pseudo-horizontal neutrino events for $5.5 \times 10^{17} < E < 1.0 \times 10^{18}$ eV: resolution of SD plane fit; co-relations to χ^2 and the number of PMTs

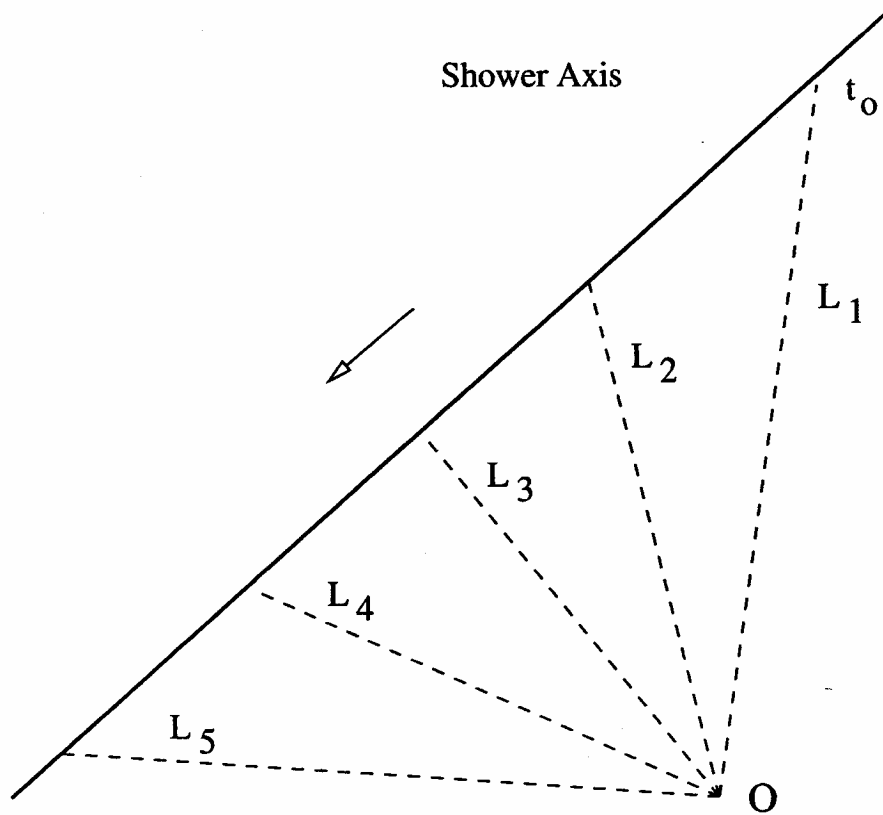


Figure 7.8. Shower axis and the direction of propagation in the SD plane; L_i ($i = 1, 2, \dots$) is the distance from the Detector to the shower axis for each bin (bin size : 1 degree)

7.2.2 Timing Fit

With the SD plane determined by the plane fit, the timing information from the triggered PMTs gives a unique way to determine the event geometry. Figure 7.8 shows the event geometry in the SD plane, in which L_i ($i = 1, 2, \dots$) is the distance from the detector to the shower axis for each bin and t_0 is the time when the shower front passes by the first bin direction. If t_0 is known, the distance L_1 from the detector to the shower axis in the first bin can be estimated by using the triggered time information assuming that the speed of shower propagation is the speed of light in free space; next, L_2 is estimated using the L_1 , bin size (1 degree), the trigger time information for the bin and the *cosine law*; and so on. Changing the value of t_0 and using a *least square* method to evaluate χ^2 for each choice of possible t_0 , the χ^2 values are compared. Once the event geometry is known from the timing fit, the shower profile of the event can be reconstructed. The X_{max} of the shower profile is a good criterion to distinguish deeply penetrating events from hadronic events. Unfortunately, the resolution of the timing fit, especially for the

pseudo-horizontal events, is not good enough for it to be used for reliable shower profile reconstruction of very rare events.

7.3 Other Possible Deeply Penetrating Events

We have focused on cosmic neutrinos as the primary source of deeply penetrating events to be observed in the HiRes I detector. However, there are other possible deeply penetrating events: Secondary hadron containing heavy quarks (for instance, charm, bottom, top) in the interaction of the EHE cosmic ray primary with atmospheric nucleus can be a source of deeply penetrating events. Under certain conditions[9], the heavy quark(for instance, the charm quark) can carry a substantial fraction of the primary cosmic ray energy to get a large Lorentz factor, and it propagates deep into the atmosphere before it decays through the weak interaction to a high-energy charged lepton, which initiates the EAS. The conditions in which such deeply penetrating events can be possible is restricted, and the heavy quark production cross section, for instance, σ_{cc}^{tot} and the Feynman X_F parameter(ratio of the energy of secondary particle to that of the primary) are not well known for EHE interactions, but an extrapolation method has been used from low energy interactions. Moreover, exotic matter[53] and other hypothetical particles can be possible sources for the deeply penetrating events.

Relatively well-known sources – neutrinos – are focused on in this thesis. However, the possibility that deeply penetrating events are from other sources is not ignored.

7.4 Neutrino Events Search

From the MC simulation ~ 9 hadronic cosmic ray events are expected with a SD plane normal angle 10-degree cut for 1 year of detector on time; ~ 328 events, with the 12-degree cut; and $\sim 1.21 \times 10^4$ events, with the 15-degree cut. The neutrino event expectation from the cosmic neutrino spectrums with the 12-degree cut and the 15-degree cut (see Tables 7.2 - 7.4, and Figure 7.3) does not change as much as the hadronic event expectation, and the number of hadronic events with the 10-degree cut is small enough so that we choose this as the criterion for the neutrino events search. The 10-degree cut and the 12-degree cut are both used to search for neutrino events in the HiRes I detector. With these plane normal angle cuts the detector acceptance is reduced to $\sim 10\%$ of the total acceptance. Figure 7.9 shows the detector acceptances with the plane normal angle cuts.

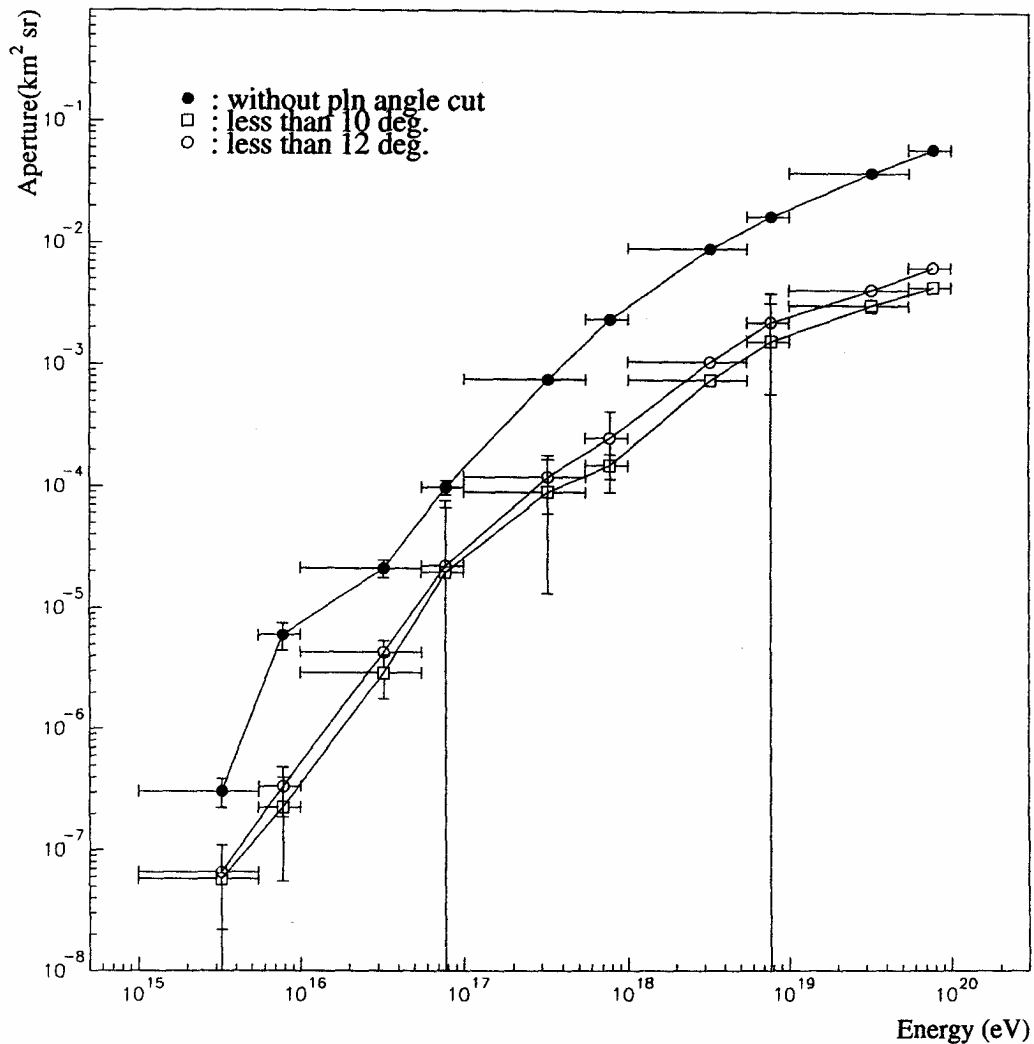


Figure 7.9. Detector acceptances with plane normal angle cuts

7.4.1 Xenon Flashers and YAG Laser Events Filtering

The data set in the HiRes I detector includes man-made events, such as Xenon flasher and YAG laser events used for detector calibration and atmospheric monitoring. The Xenon flasher events are all almost vertically upward; hence, it is easy to distinguish the flasher events from the deeply penetrating events, because the maximum elevation angle for possible upward-going deeply penetrating events should be less than ~ 25 degrees (see Figure 6.8). However, there are also inclined (~ 6 degrees in elevation) Xenon flashers, and many YAG laser events cannot be distinguished by just the elevation angle cut. Given

the known geometry for the laser events, such as the tabulated YAG laser source position at HiRes II ³ and timing information, the efficiency of finding the laser events using any algorithm can be determined.

The number of PMTs in many laser events and the inclined Xenon flasher events is more than 300; but for most of the possible neutrino events, it is less than 300 – Figure 7.7. Hence, the 300-tube number cut is applied to save processing time in the laser events selection. After this, the noise tubes in each event are filtered out, and the track length cut(6 degree) is applied again. Furthermore, if the tube number is less than the track length or the tube number is greater than four times of the track length the event is assumed to be a noise event. The plane fit is then applied. If the χ^2 of the plane fit is greater than 2.0, the event is also assumed to be a noise event.

Since laser events come from a laser source positioned at HiRes II, if the angle, Θ , (degree) between the SD plane normal vector, \vec{V}_n and the pointing vector from the HiRes I to the HiRes II is in $87.5^\circ < \Theta < 92.5^\circ$,⁴ the event is assumed to be a laser event. Then one extra bin, pointing to HiRes II, is added in the timing fit process, and χ^2 values from the timing fit are compared to each other before and after adding the bin. The efficiency of the laser event selection was tested with the known YAG laser data in HiRes I. Two Yag laser data sets were selected, one (12/01/2000) of which is for good weather condition and the other (04/15/1999) for bad weather condition. In the good weather condition case, $\sim 76\%$ out of 11632 laser events were selected to be laser events; $\sim 20\%$ were rejected with 6 degree track length cut or considered to be noise events; and 26 events ($\sim 0.2\%$) out of the 11632 laser events were filtered into the 12-degree cut. In bad weather conditions, $\sim 63\%$ out of 6152 laser events were selected to be laser events; $\sim 36\%$ were rejected; and 1 event was filtered into the 12-degree cut.

In the case of artificial events, the Yag laser events and the inclined Xenon flasher events have a unique character – they exhibit repetition with fixed geometries. However, repetition cannot be expected for neutrino events in a finite time. This unique character is useful in selecting out the artificial events.

³In the hires coordinate system, the hires2 lidar system is located at (-10518.8 -7062.8 -52.2); the old Fly's Eye lidar system is at (1667.87 2934.67 -133.67) in unit of meters.

⁴For ideal case it should be 90 degrees; the resolution of the plane fit for pseudo-horizontal events is ~ 1.5 degree.

7.4.2 Neutrino Events Search with MC Data

The neutrino events search efficiency was tested with MC data. Since the HiRes I detector cannot clearly distinguish nearby triggered events from noise events or fake events generated by μ or Cherenkov light, an R_p cut and/or angular speed cut was necessary in the data analysis. In the pseudo-horizontal neutrino event search an angular speed cut was applied, with which the noise and fake events are removed. It is equivalent to a 1.5 km R_p cut for a 6 degree track length.

With the 12-degree plane normal angle cut, the track length cut (6 degrees), the angular speed cut, and the filtering processes for noise tubes, noise events, laser events, the efficiency increases with neutrino energy from $\sim 0\%$ for the low-energy region (1.0×10^{15} eV - 1.0×10^{16} eV) to $\sim 56\%$ for the high-energy region (5.5×10^{19} eV - 1.0×10^{20} eV) – Table 7.5. For low-energies, $E < 1.0 \times 10^{16}$, we cannot expect many events to survive the angular speed cut since the low energy events will be close to the HiRes I detector. In Table 7.5, *reject* indicates the number of events rejected as noise in the filtering process or due to errors in the plane fitting. If any neutrino event in the MC data is considered to be a laser event in the filtering process, the event is also rejected as a *laser*.

In Table 7.6 the expectation of neutrino events for 1 year (detector on time) is summarized with the detector acceptance, the model spectrums for cosmic neutrinos, and the search efficiency found in the Table 7.5.

7.4.3 HiRes I Data and Data Processing

In searching for cosmic neutrino events in the HiRes I detector the data set can be categorized into two parts: the first part includes old Fly’s Eye laser data and the second part includes HiRes II laser data. To select out laser events in the first part of the HiRes

Table 7.5. Neutrino events search efficiency with the 12-degree cut.

neutrino energy(eV)	Efficiency(%)	reject(%)/laser(%)	angular speed cut(%)
$1.0 \times 10^{15} - 5.5 \times 10^{15}$	0	73 / 0	27
$5.5 \times 10^{15} - 1.0 \times 10^{16}$	0	59 / 0	41
$1.0 \times 10^{16} - 5.5 \times 10^{16}$	12	62 / 1	25
$5.5 \times 10^{16} - 1.0 \times 10^{17}$	22	62 / 2	14
$1.0 \times 10^{17} - 5.5 \times 10^{17}$	37	47 / 4	12
$5.5 \times 10^{17} - 1.0 \times 10^{18}$	43	38 / 5	14
$1.0 \times 10^{18} - 5.5 \times 10^{18}$	48	33 / 9	10
$5.5 \times 10^{18} - 1.0 \times 10^{19}$	46	26 / 15	13
$1.0 \times 10^{19} - 5.5 \times 10^{19}$	54	22 / 12	12
$5.5 \times 10^{19} - 1.0 \times 10^{20}$	56	21 / 12	11

Table 7.6. Neutrino events expectation in the HiRes I detector for 1 year(detector on time) with the 12-degree SD plane normal angle cut and the events search efficiency.

model/energy(eV)	$> 10^{15}$	$> 10^{16}$	$> 10^{17}$	$> 10^{18}$	$> 10^{19}$
AGN-M95	0.8	0.8	0.8	0.5	–
AGN-SS91	0.1	0.1	–	–	–
AGN-P96	1.0	1.0	1.0	0.3	–
GRB-WB	–	–	–	–	–

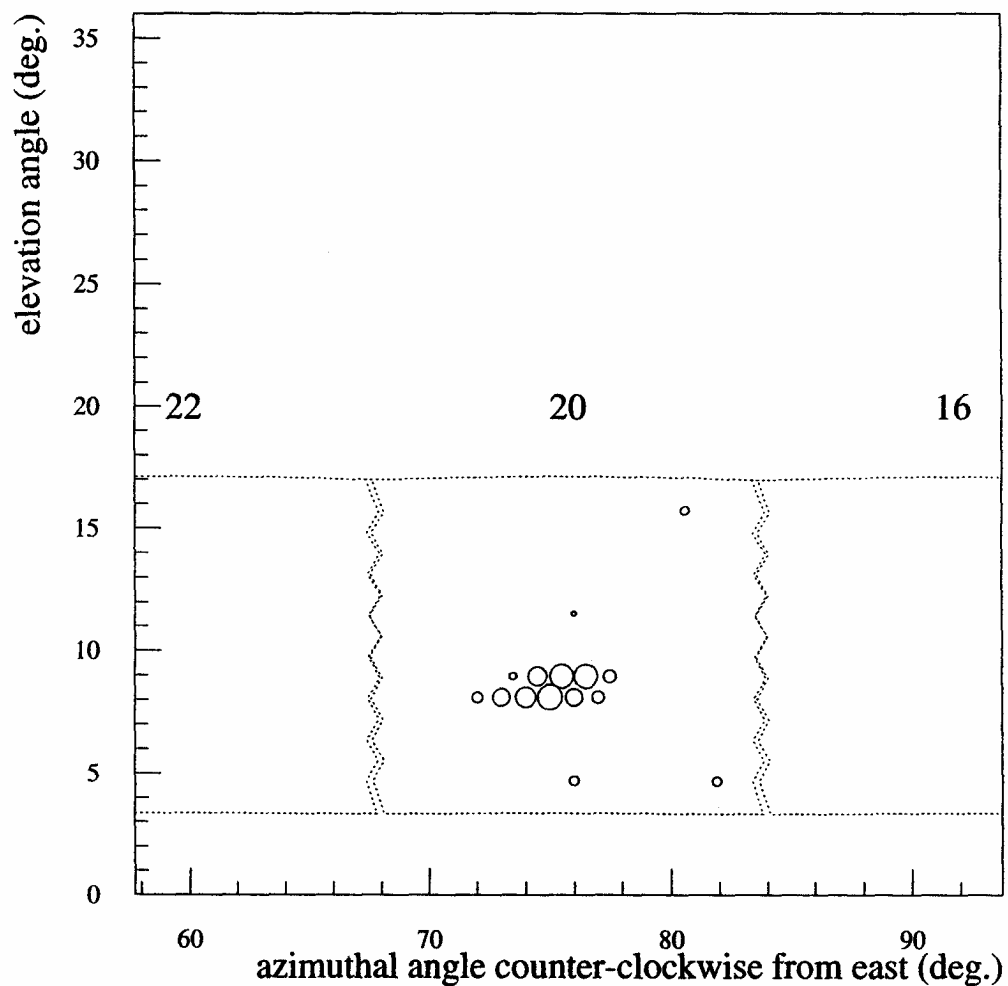
I data set is not easy; there is no exact timing and geometry information for laser events with which any suspicious event can be traced back to check out if it is a laser event or not, and there is no laser sample data set extracted from the HiRes I data set with which the laser events selection efficiency can be tested. This thesis reports on a search using the second part of the HiRes I data only.

Available HiRes I data (10/01/1999 – 07/28/2001) from the second part, which is calibrated (PASS1) and anonymously accessible, was located at *titus.physics.utah.edu*. The daily data file set was brought to *icebox.chpc.utah.edu* and taken through the PASS2 process to select out downward-going events (.ps2d.dst) with zenith angle, $\Theta < 70^\circ$. Then, two remaining file sets (.ps2u.dst and .ps2h.dst) for horizontal events ($\Theta > 70^\circ$) and upward-going events were merged to one data file. With the merged data file YAG laser events selection was done; after which the horizontal events selection was made with the 10-degree cut and the 12-degree cut in the SD plane normal angle. Here, all Xenon flasher events were also removed, since the event geometries are out of the SD plane normal angle cuts.

Finally, two data sets were created, in which neutrino candidate events could be included, but still including many noise events mixed up with remaining YAG laser events. At this stage, some noise events were selected out by hand; and some of the remaining YAG laser events were also selected out if geometrically similar events repeated in a short time period. Then, the remaining events were categorized for each mirror data set (22-mirror data set) to search for geometrical repetition. To remove remaining noise events, PMT trigger time information was used to determine if the data were event or not.

twelve events with the 10-degree SD plane normal angle cut and 10 events with 10 - 12 degree cut were left for further investigation. For those events the repetition of the event pattern was searched for again by investigating nearby events within 1 min in the

pass1 data file set. Repetitions were found for almost all events; hence, the events were considered to be Yag laser events. Some of these events were already filtered out as Yag laser events or not filtered into the 10 degree or 10 - 12 degree SD normal angle cut because of noise tubes in the filtering process. Only one event(Julian date : 11936.8587706; 01/26/2001 23:51 in Utah) out of the 22 events had no associated pattern repetition found. It is shown in Figure 7.10. With the SD plane fit and the timing fit the event geometry



BigH 00011936 2001-JAN-26 : 23:51:17.062 101 845

Figure 7.10. The event on the cluster box plane

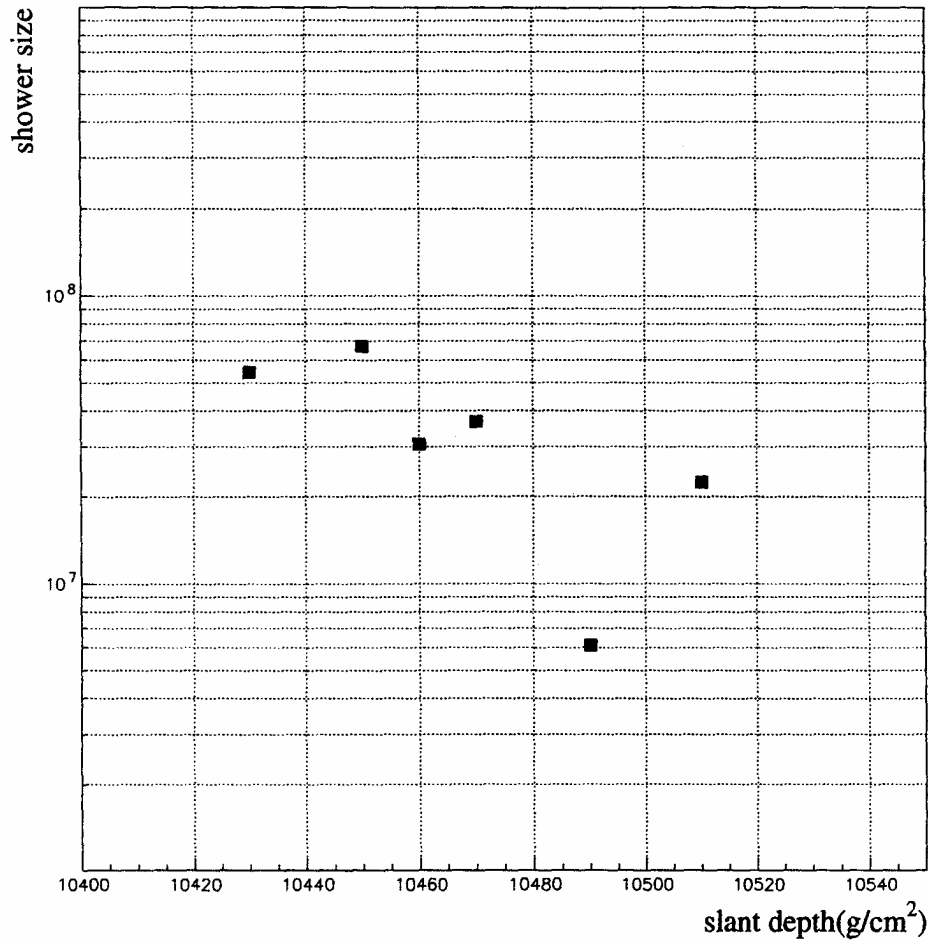


Figure 7.11. Shower size vs. slant depth

was estimated as $\theta \sim 94^\circ$ (downward-going); $\phi \sim 349^\circ$; $R_p \sim 6$ km; ground impact point, ($\sim 15.0, \sim 3.7, 0.0$) km. Shower profile reconstruction was done for the event assuming that the event was not a noise event. Figure 7.11 shows the shower profile reconstructed with the six bin data: The X_{max} depth with which we can distinguish any possible deeply penetrating event from hadronic cosmic ray events cannot be estimated from the profile. The shower profile was then compared to the EM longitudinal Gaisser-Hillas (GH) profile to determine if it was consistent with being a part of a hadronic cosmic ray event or a part of deeply penetrating event. The pattern matched a GH profile with energy $\sim 10^{+10}$ GeV. Figure 7.12 shows the GH profile, in which the slant depth of the profile was shifted to $+8530$ g/cm² for the fitting to the data points indicated with solid boxes.

If the event was a hadronic cosmic ray event, then the X_{max} , ~ 9500 g/cm² cannot be

explained. If the event was a neutrino event or deeply penetrating event, it is not clear why just a part of signal profile was detected by the HiRes I detector. Therefore, this event is probably not a cosmic ray event.

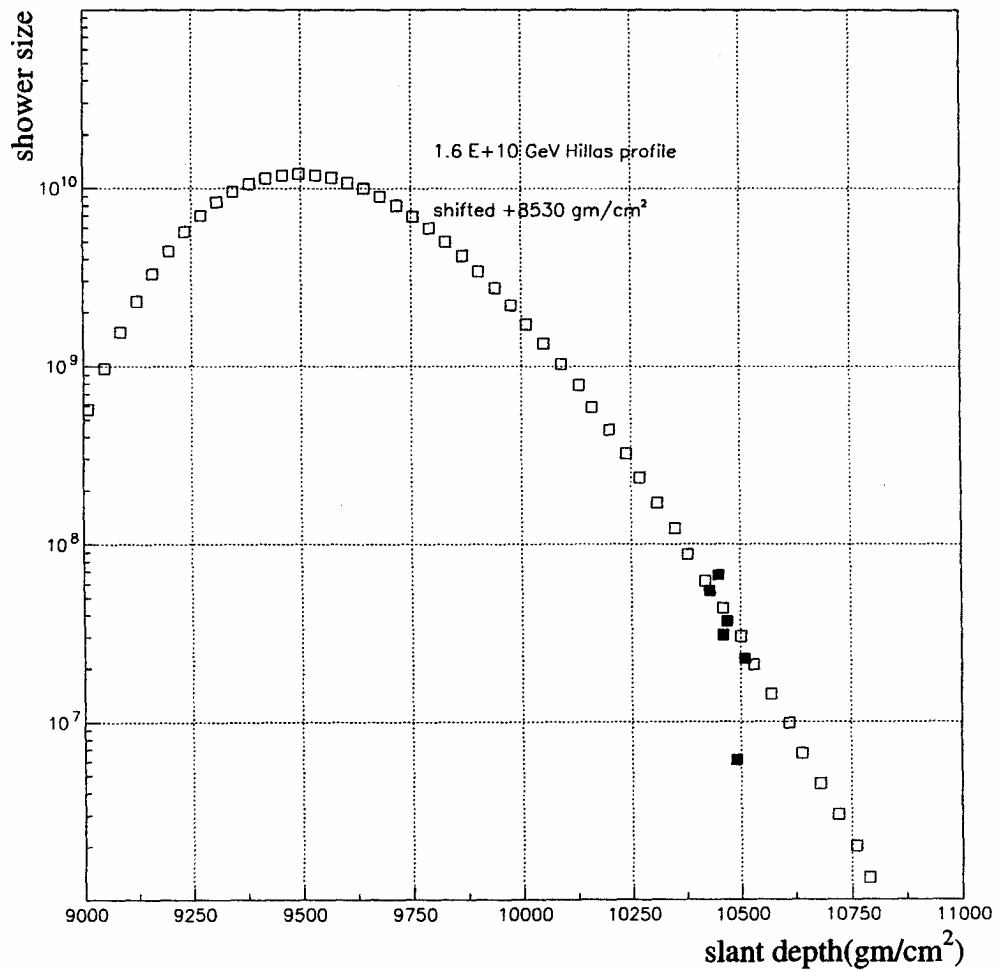


Figure 7.12. EM longitudinal Gaisser-Hillas profile with energy 1.6×10^{10} GeV; slant depth is shifted $+8530 \text{ g/cm}^2$

CHAPTER 8

CONCLUSION AND DISCUSSION

8.1 Conclusion

No cosmic neutrino event or deeply penetrating event was found in the HiRes I data from October, 1999 to July, 2001.

From the cosmic neutrino model spectrums, such as AGM-M95, AGN-SS91, AGN-P96, and GRB-WB, no reasonable number of neutrino events could be expected in the HiRes I detector for such a short time period (see Table 7.6), and indeed no events were found. For the model spectrums and the neutrino event search method described in this work, it would take more than 10 calendar years of operation to find any neutrino event in the HiRes I detector.¹ However, changing the data analysis method might make detection possible. For instance, the model spectrums such as AGN-M95 and AGN-P96 are close to the minimum cosmic neutrino flux required for the HiRes I detector to detect ~ 1 event/yr (see Table 6.2) if we use all data with zenith angles $\theta > 70^\circ$.

Assuming one neutrino event was detected with the HiRes I detector for the time period (10/01/1999 - 07/28/2001), we can estimate a flux limit of $\nu_\mu + \bar{\nu}_\mu$ using the total detector acceptance. In this time period, the HiRes I detector took data for 1618.91 hours ($\sim 18.5\%$ of 1 year), which was averaged over 21 active mirrors.[54] Figure 8.1 shows the ν flux limit (90% CL) required for observing at least one neutrino event for $E_\nu > 1.0 \times 10^{17}$ eV. Here, the differential cosmic neutrino spectrum is assumed to be a power law, $dN/dE \sim E^{-\gamma}$ with $1.0 < \gamma < 3.0$.

Considering that none of the proposed cosmic neutrino spectrum models has yet been confirmed, and that the value of the UHE neutrino cross section is not well known, this null result is just a first step in the systematic neutrino event search with the HiRes I and HiRes II detectors.

According to the MC simulation for cosmic neutrino events in the HiRes I detector, the detector acceptance of the earth originated upward-going events is ~ 1 order of magnitude

¹Considering the $\sim 10\%$ of duty cycle of the detector.

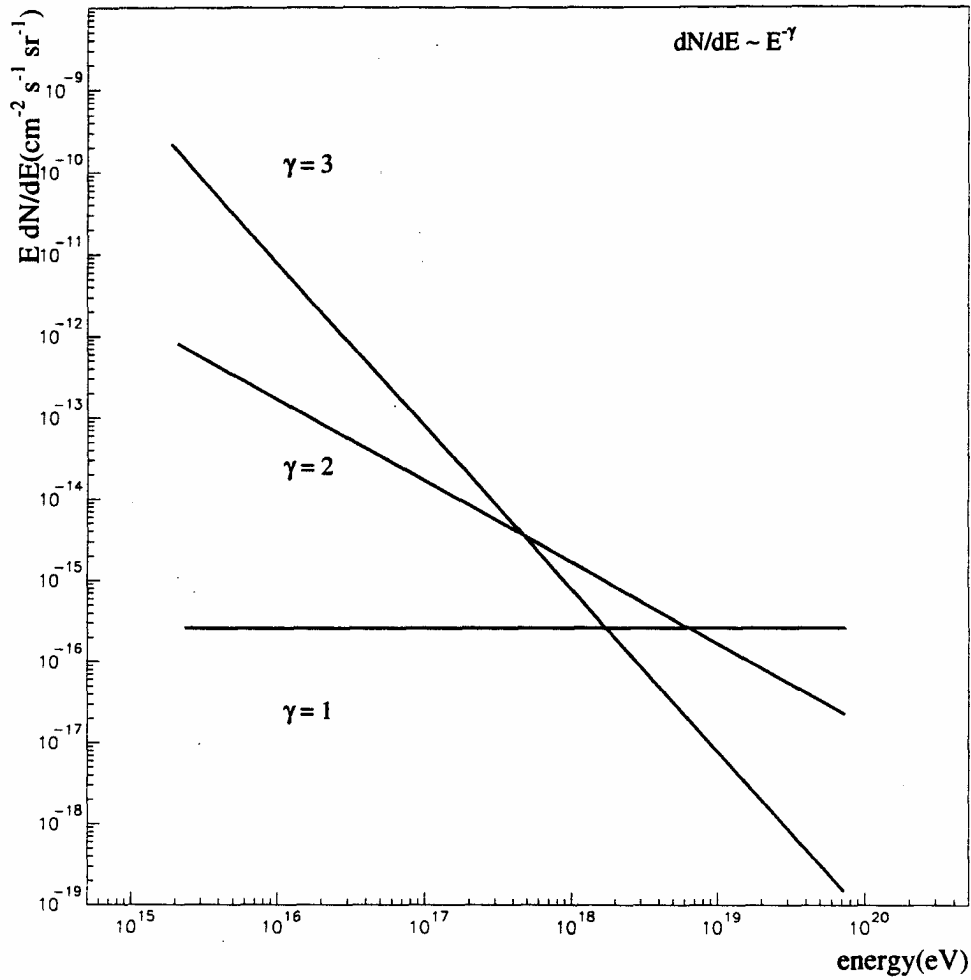


Figure 8.1. $\nu_{\mu} + \bar{\nu}_{\mu}$ neutrino flux limit for $\gamma = 1, 2, 3$

smaller than the acceptance for the horizontal events produced in the atmosphere, which is $\sim 10\%$ of the total detector acceptance. Hence, expecting earth originated events to be observed in the HiRes I detector is not realistic. Furthermore, the search for low energy neutrino events ($E < 10^{+16}$ eV) is not appropriate for the HiRes I detector, because most of the events are too close to the detector to be distinguished from background noise events.

8.2 Discussion

A clear method to distinguish neutrino events from hadronic cosmic ray events has been demonstrated for the HiRes Detector. That involves the search for pseudo-horizontal

events using the SD plane normal angle(PLN) cut, which needs to be chosen to include both horizontal events and earth-originated events. The PLN cut can be chosen so that no hadronic events pass, or it can be chosen to include some hadronic events so as to increase the detector neutrino acceptance. The former choice is a strong cut which can find any trace of deeply penetrating events quickly, but the latter choice is more sensitive and needs more time and work than the former choice. In the latter choice, an event-by-event shower profile reconstruction is necessary to distinguish the deeply penetrating events from the hadronic events, most of which should not show the X_{max} in the shower profile but just a part of a tail in their profiles.

In this thesis, the strong cut (the former choice) was chosen. In the MC simulation, the horizontal events occurred with zenith angles from $\theta \sim 83^\circ$ to $\theta \sim 92^\circ$; and the earth originated events, from $\theta \sim 90.6^\circ$ to $\theta \sim 113^\circ$. To find a proper zenith angle limit to avoid hadronic events the detector acceptance for the hadronic events was calculated with several zenith angle cuts in the event geometries (see Figures 7.2 - 7.3). In the hadronic event generating process in the MC the same algorithm (spherical shell criterion) was used as in the MC for the neutrino events. The event rates of the hadronic cosmic rays were then estimated with the cosmic ray spectrum in Figures 7.4 - 7.5 and Table 7.1. The 10-degree PLN angle cut would clearly avoid hadronic events, but the 12-degree PLN angle cut was also chosen because the uncertainty of plane fit was $\pm 1.5^\circ$.

In the HiRes I data there were not only cosmic ray events but also many artificial events such as Yag laser events and Xenon flasher events which had to be removed from the data. A filtering process including a noise tube cut, a noise event cut, a 6-degree track length cut, and an angular speed cut was necessary to remove these artificial events. Even after the filtering process some laser events and noise events remained. To remove these laser events and noise events the topological repetition of patterns on the cluster box plane correlated with the event time information in PMTs was investigated. Any event having a repetition within $\pm 30 \sim \pm 40$ events before and after the event in the daily data file set was considered to be a laser event and was removed. One suspicious event remained, but it was ruled to be a noise event. The shower profile of the event did not show a whole shower profile (as shown in Figure 7.11). If the event was a cosmic ray event, why the detector received just a part of the signal from the shower cannot be explained.

8.3 Summary of MC

The MC for cosmic ν_μ and ν_e neutrino events for energy $E \geq 1.0 \times 10^{15}$ eV was modified from the conventional MC for hadronic cosmic ray events as follows: first, the

event generation algorithm was modified since the neutrino has an extremely small cross section and the interaction of (νN) is almost equally probable anywhere in the earth atmosphere, though the probability is extremely small. Instead of a square surface on the ground used for hadronic interactions, a spherical surface was used for the impact points of incident neutrino trajectories, where the HiRes I detector is at the center of the spherical surface. With this algorithm all possible event geometries were considered in the MC even for the neutrino events originating from below the surface of the earth. For the (νN) and (νe) neutrino cross section in the atmosphere and inside the earth, the parton model (CTEQ4-DIS) was used, and the shadow effect of the earth on the neutrino flux was estimated for all incident directions and energies of neutrinos.

In the MC simulation the neutrino flux ratio of ν_μ to ν_e was 2 : 1 with the assumption that the cosmic neutrinos are created mainly from the pion photo-production as in the cosmic neutrino model spectrums, AGN-M95, AGN-P96, AGN-SS91, and GRB-WB.

REFERENCES

- [1] T. C. Weekes. Phys. Rep. 160 (1988) 1 ; P. Sokolsky, P. Sommers, and B. R. Dawson, Phys. Rep. 217, No. 5 (1992) 225-277.
- [2] Linsley, J., Phys. Rev. Lett., **10** 146; G. Brooke *et al.*, (Haverah Park Collab.), *Proc. 19th Intl. Cosmic Ray Conf.* (La Jolla) **2**, 150 (1985); M.A. Lawrence, R.J.O. Reid, A.A. Watson, J. Phys. G **17** 733 (1991); N. N. Efimov *et al.*, (Yakutsk Collab.) *ICRR Symposium on Astrophysical Aspects of the Most Energetic Cosmic Rays*, ed. N. Nagano and F. Takahara, World Scientific pub. (1991); *Proc. 22nd ICRC*, Dublin (1991); N. Hayasihida *et al.*, Phys. Rev. Lett. **73**, 3491 (1994); S. Yoshida, *et al.*, (AGASA Collab.) *Astropart. Phys.* **3**, 105 (1995); D.J. Bird *et al.*, (Fly's Eye Collab.) Phys. Rev. Lett. **71**, 3401 (1993); *The Astrophysical Journal*, **424**, 491 (1994); *ibid.* **441**, 144 (1995).
- [3] K. Greisen, Phys. Rev. Lett., Vol. **16**, 17, (1966) p. 748
- [4] D. J. Bird, *et al.* *Astrophysical Journal*, 441 (1995) p. 144; M. A. Lawrence, R.J.O. Reid, A.A. Watson, J. Phys. G **17**(1991), 733; J. W. Elbert and P. Sommers, *Astrophysical Journal*, 441 (1995) p. 151; F. Halzen, *et al.* *Astroparticle Physics*, 3 (1995) p. 151; R. J. Protheroe and P. A. Johnson, [lanl.arXive.org, astro-ph/9605006](http://lanl.arXive.org/astro-ph/9605006).
- [5] T. J. Weiler, Phys. Rev. Lett. **49** 234 (1982); S. Yoshida, *Workshop on Observing Giant Cosmic Ray Air Showers from $> 10^{20}$ eV Particles from Space* 246 (1997).
- [6] T. K. Gaisser, A. K. Harding, and T. Stanev, *Astrophysical Journal*, **345** (1989) p. 423; K. Mannheim and P. L. Biermann, *Astronomy and Astrophysics*, **253**, L21-L24 (1992).
- [7] Sudbury Neutrino Observatory, <http://www.sno.phy.queensu.ca/>; AMANDA, <http://amanda.berkeley.edu/>; Baikal, <http://www-zeuthen.desy.de/baikal/>; Super Kamiokande, <http://www-sk.icrr.u-tokyo.ac.jp/>.
- [8] R. Baltrusaitis *et al.* *The Astrophysical Journal*, **281** (1984) p. L9-L12; *The American Physical Society* **31** 2192 (1985).
- [9] B. L. Emerson, Ph.D. thesis, University of Utah, 1992.
- [10] F. W. Stecker *et al.* Phys. Rev. Lett., Vol. **66**, 21, (1991) p. 2697
- [11] T. K. Gaisser and Todor Stanev, Phys. Rev. D, Vol. **57**, 3, (1998) p. 1977; C. T. Hill and David N. Schramm, Phys. Rev. D, Vol. **31**, 3, (1985) p. 564; F. W. Stecker, *et al.* Phys. Rev. Lett., Vol. **66**, 21, (1991) p. 2697; K. Mannheim, *Astron. Astrophysics*, 269, 67(1993) p. 67; A. P. Szabo and R. J. Protheroe, *Astroparticle Physics* 2 (1994) p. 375; T. K. Gaisser, *et al.* Phys. Rev. D, Vol. **54**, 9, (1996) p. 5578; R. J. Protheroe, [lanl.arXive.org, astro-ph/9607165](http://lanl.arXive.org/astro-ph/9607165); R. Gandhi, *et al.*

- Astroparticle Physics 5 (1996) p. 81; K. Mannheim, R. J. Protheroe, and J. P. Rachen, [lanl.arXive.org, astro-ph/9812398](https://arxiv.org/abs/astro-ph/9812398).
- [12] L. V. Volkova, *Yad. Fiz.* **31**, 1510(1980); V. Agrawal, T. K. Gaisser, P. Liparri, T. Stanev, *Phys. Rev. D* **53**, 1314, (1996).
- [13] J. D. Bjorken and E.A. Paschos, *Phy. Rev.*, Vol. **185**, 5, (1969) p. 1975; C. Quigg, M. H. Reno, and T. P. Walker, *Phys. Rev. Lett.*, Vol. **57**, 6, 774 (1986); H. L. Lai, *et al.*, *Phys. Rev. D*, Vol. **51**, 9, (1995) p. 4763; R. Gandhi *et al.* *Astroparticle Physics*, vol. **5** (1996) 81-110; R. Gandhi *et al.*, [lanl.arXive.org, hep-ph/9807264](https://arxiv.org/abs/hep-ph/9807264).
- [14] P. Sokolsky, *Introduction to Ultrahigh Energy Cosmic Ray Physics* (Addison-Wesley Publishing Company, Inc., 1989) p. 8; M. A. Huang, Ph.D. thesis, University of Utah, 1996, p. 4.
- [15] P. Sokolsky, *Introduction to Ultrahigh Energy Cosmic Ray Physics* (Addison-Wesley Publishing Company, Inc., 1989) p. 84 - 102.
- [16] P. Sokolsky, *Introduction to Ultrahigh Energy Cosmic Ray Physics* (Addison-Wesley Publishing Company, Inc., 1989) p. 6-7.
- [17] J. Ranft, *Phys. Rev. D*, Vol. **51** 64 (1995); R.S. Fletcher, T.K. Gaisser, P. Lipari, and T. Stanev, *Phys. Rev. D*, Vol. **50**, 5710 (1994); N. Kalmykov *et al.*, *Physics of Atomic Nuclei*, **58**, 1728 (1995).
- [18] T. K. Gaisser, *Cosmic Rays and Particle Physics*, (Cambridge University Press, 1990) p. 245
- [19] C. Caso *et al.*, *Particle Physics Booklet* (Extracted from the Review of Particle Physics), *The European Physical Journal C* **3** (1998), p. 26-45
- [20] C. Caso *et al.*, *Particle Physics Booklet* (Extracted from the Review of Particle Physics), *The European Physical Journal C* **3** (1998), p. 186
- [21] W. Heitler *Quantum Theory of Radiation* (Oxford University Press, 1944) 2nd edition; M. S. Longair, *High Energy Astrophysics*, Cambridge, Cambridge University Press, 1991, p. 120; Pierre Sokolsky, *Introduction to Ultrahigh Energy Cosmic Ray Physics* (Addison-Wesley Publishing Company, Inc., 1989) p. 20.
- [22] A. M. Hillas, *J. Phys. G: Nucl. Phys.*, **8**, 1982, p. 1461-1473
- [23] J. Linsley, in *Proc. 18th ICRC, Bangalore, India*, vol. **12**, p. 135; A. M. Hillas, in *Proceedings of the Cosmic Ray Workshop, University of Utah 1983*, p. 21
- [24] T. K. Gaisser and A. M. Hillas, *Proc. 15 th ICRC, Plovdiv, Bulgaria, 1977*, vol. **8**, p. 353
- [25] D. J. Bird *et al.*, *Proc. 23rd ICRC (Calgary)*, **2**:34, (1993); D. J. Bird *et al.*, *Phys. Rev. Lett.*, **71**:3401, (1993).
- [26] J. Velasco, *et al.*, [lanl.arXive.org, hep-ph/9910484](https://arxiv.org/abs/hep-ph/9910484).
- [27] R. M. Baltrusaitis, *et al.*, *Nucl. Instr. Meth.*, A240, 1985, p. 414; P. Sokolsky, *Introduction to Ultrahigh Energy Cosmic Ray Physics* (Addison-Wesley Publishing

- Company, Inc., 1989) p 50.
- [28] A. N. Bunner, Ph.D. thesis, Cornell University, 1967.
- [29] K. D. Green, Ph.D. thesis, University of Utah, 1992, p. 44-55.
- [30] D. R. Longtin, E. P. Shettle, J. R. Hummel, and J. D. Pryce, *A Wind Dependent Desert Aerosol Model : Radiative Properties* (Scientific Report No. 6, AFGL-TR-88-0112, 1988); P. Sokolsky, *Introduction to Ultrahigh Energy Cosmic Ray Physics* (Addison-Wesley Publishing Company, Inc., 1989) p. 198
- [31] <http://hires.physics.utah.edu/internal/atmos-ana/index.html>
- [32] T. AbuZayyad, Ph.D. thesis, University of Utah, 2000, p. 21
- [33] G. F. Knoll, *Radiation Detection and Measurement*, (John Willy & Sons, Inc., 1989) p. 251-285
- [34] M.J. Kidd, Ph.D. thesis, University of Illinois, 1997.
- [35] K. Belov, The mirror threshold data in HiRes I detector, University of Utah, 2000.
- [36] T. AbuZayyad, Ph.D. thesis, University of Utah, 2000.
- [37] Monte Carlo program set for cosmic neutrino events was modified partially from the one started by J. Elbert and M. Salamon in the early 1980's; and it has been improved by B. Dawson (University of Adelaide) (1985 -), H. Dai (1990 -1997), and by Fly's Eye and HiRes collaborators.
- [38] C. T. Hill and D. N. Schramm, *Phys. Rev. D*, Vol. **31**, 3, (1985) p. 564; F. W. Stecker, *et al. Phys. Rev. Lett.*, Vol. **66**, 21, (1991) p. 2697; A.P. Szabo and R. J. Protheroe, *Astroparticle Physics*, 2, (1994) p. 375; K. Mannheim, *Astron. Astrophysics*, 269, 67(1993) p. 67; T. K. Gaisser, *et al. Phys. Rev. D*, Vol. **54**, 9, (1996) p. 5578; R. Gandhi, *et al. Astroparticle Physics*, 5, (1996) p. 81; R. J. Protheroe, lanl.arXive.org, astro-ph/9607165; T. K. Gaisser and Todor Stanev, *Phys. Rev. D*, Vol. **57**, 3, (1998) p. 1977; K. Mannheim, R. J. Protheroe, and J. P. Rachen, lanl.arXive.org, astro-ph/9812398.
- [39] R. Gandhi *et al.*, lanl.arXive.org, hep-ph/9807264.
- [40] E. Waxman and J. Bahcall, *Phys. Rev. D*, Vol. **59**, 023002, (1998) p. 59; E. Waxman and John Bahcall, lanl.arXive.org, hep-ph/9902383.
- [41] K. Mannheim, *Astroparticle Physics* **3**, 295 (1995)
- [42] E. Waxman and J. Bahcall, *Phys. Rev. Lett.*, **78**, 2292 (1997).
- [43] J. D. Bjorken and E.A. Paschos, *Phys. Rev.*, Vol. **185**, 5, (1969) p. 1975.
- [44] C. Quigg, M. H. Reno, and T. P. Walker, *Phys. Rev. Lett.*, Vol. **57**, 6, 774 (1986).
- [45] R. Gandhi *et al.* *Astroparticle Physics*, vol. **5** (1996) p. 81-110.
- [46] H. L. Lai, *et al.*, *Phys. Rev. D*, Vol. **51**, 9, (1995) p. 4763

- [47] C. Caso *et al.*, *Particle Physics Booklet* (Extracted from the Review of Particle Physics), The European Physical Journal **C3**, (2000) p. 16
- [48] T. K. Gaisser, *Cosmic Rays and Particle Physics*, (Cambridge University Press, 1990) p. 76.
- [49] A. B. Migdal, *Phys. Rev.*, Vol. **103**, 6, (1956) p. 1815.
- [50] T. Stanev and C. Vankov *et al.*, *Phys. Rev. D*, Vol. **25**, 5, (1982) p. 1291.
- [51] A. M. Dziewonski and D. L. Anderson, *Physics of the Earth and Planetary Interior*, **25** (1981) 297.
- [52] C. Caso *et al.*, *Rev. of Particle Physics* (The European Physical Journal) **C**, Vol. 15, (1999) p. 173.
- [53] Brasil-Japan Group, *Proc. 15th ICRC(Ploudiv)*, **7**, 208, (1977).
- [54] B. T. Stokes, The HiRes I detector run time calculation, University of Utah, 2002.